UNIVERSITY OF TRENTO - Italy

International PhD Program in Biomolecular Sciences
Centre for Integrative Biology

30th Cycle

"Inhibition of mitochondrial translation as a novel strategy to eradicate glioblastoma stem cells"

Tutor

Prof. INES MANCINI

Department of Physics, University of Trento

Advisor

Dr. ANGELIKA MODELSKA

CIBIO, University of Trento

Ph.D. Thesis of

DENISE SIGHEL

CIBIO, University of Trento

Academic Year 2016-2017

Original authorship

Declaration:

I, Denise Sighel, confirm that this is my own work and the use of all material from other sources has been properly and fully acknowledged.

TABLE OF CONTENTS

ABSTRACT

Glioblastoma multiforme (GBM) is the most common and aggressive primary brain tumor in adults. The search for new effective chemotherapeutic agents to treat GBM has proven challenging throughout the last few decades. As a result, very limited pharmacological treatment is currently available.

GBM aggressiveness is associated with its glioblastoma stem cells (GSCs) component, which is responsible for resistance to therapy. Therefore, new specific pharmacological approaches directed to eradicate GSCs are endowed with a great therapeutic potential.

GSCs have been shown to rely on mitochondrial respiration for their high energy demand. In order to have a functional mitochondrial respiration process, the five complexes forming the oxidative phosphorylation (OXPHOS) chain have to be built by the coordinate assembly of proteins translated by either the cytosolic or the mitochondrial ribosomes.

Given their endosymbiotic origin and despite the evolutionary changes occurred the mitochondrial ribosomes (mitoribosomes) still share structural and functional similarities with the bacterial ones, particularly considering the functional ribosomal core. In the light of these similarities, we hypothesized that antibiotics targeting bacterial ribosomes could be exploited to inhibit mitoribosomes, affecting mitochondrial translation and OXPHOS assembly, and hence leading to detrimental effect on GSCs viability.

We performed a high-content imaging driven screening of several bacterial ribosome targeting antibiotics and identified quinupristin/dalfopristin (Q/D) as the most promising compound due to its cytotoxic and mitotoxic effects on GSCs.

We demonstrated that Q/D effectively prevents GSCs expansion, resulting to be over an order of magnitude more effective in GSCs growth inhibition than temozolomide, the only drug used in first line GBM therapy. We then investigated the mechanism of action of Q/D, proving that it inhibits mitochondrial translation and, as a consequence, it decreases the functionality of the OXPHOS complexes reducing mitochondrial respiration capacity. Moreover, we obtained the structure of this compound bound to the human mitoribosome using cryo-electron microscopy, which provides the basis for further development of more potent analogs.

Finally we proved the efficacy of Q/D *in vivo* using a xenograft mouse model of GBM.

Our results suggest that mitochondrial translation represents a therapeutic target for GBM and show that Q/D, acting *via* inhibition of mitochondrial translation, is extremely effective against GSCs. Interestingly, Q/D has been approved by the Food and Drug Administration

(FDA) in 1999 and, therefore, its toxicological and pharmacokinetic properties are known, making this antibacterial antibiotic a candidate drug for repurposing for GBM treatment. Given the urgent medical need for novel therapeutic approaches in GBM treatment, Q/D represents a promising therapeutic solution that is worth further preclinical and clinical investigations.

ABBREVIATIONS

ATP	Adenosine triphosphate
Baf	Bafilomycin
BBB	Blood-brain barrier
BN-PAGE	Blue native polyacrylamide gel electrophoresis
CNS	Central Nervous System
COX1	Cytochrome *c* oxidase subunit 1
COX4	Cytochrome *c* oxidase subunit 4
CQ	Chloroquine
CSCs	Cancer stem cells
D	Dalfopristin
DMSO	Dimethyl sulfoxide
EGF	Epidermal growth factor
ESI-MS	Electrospray mass spectrometry
ETC	Electron transport chain
$FADH_2$	Reduced flavin adenine dinucleotide
FCCP	Carbonyl cyanide-4-(trifluoromethoxy)phenylhydrazone
FDA	Food and Drug Administration
FGF2	Fibroblast growth factor
GBM	Glioblastoma Multiforme
GSCs	Glioblastoma stem cells
Gy	Grays
IMP2	Oncofetal insulin-like growth factor 2 mRNA-binding protein 2
MGMT	O^6-methylguanine DNA-methyltransferase
mtDNA	Mitochondrial DNA
mt-LSU	Mitochondrial ribosomal large subunit
MTO	MitoTracker Orange
mt-SSU	Mitochondrial ribosomal small subunit
NADH	Reduce nicotinamide adenine dinucleotide
NMR	Nuclear magnetic resonance spectroscopy
NSCs	Neural stem cells
OXPHOS	Oxidative phosphorylation
PI	Propidium iodide
PTC	Peptidyl transferase centre
Q	Quinupristin
Q/D	Quinupristin/Dalfopristin
TMZ	Temozolomide
WHO	World Health Organization

THESIS ORGANIZATION

The thesis is organized in eight main chapters: Introduction, Hypothesis and Aims, Results, Discussion, Conclusions, Ongoing work, Future Perspectives and Experimental Procedures.

The introduction chapter describes the background at the base of this project, focusing on evidence published before and during the period in which this work has been carried out. The introduction starts describing glioblastoma multiforme (GBM) as a disease, reviews the standard of care used in GBM treatment and continues focusing on the glioblastoma cancer stem cell (GSC) component, with particular attention on GSCs metabolism. It moves on with some hints on mitochondrial respiration metabolism, on oxidative phosphorylation (OXPHOS) chain and on mitochondrial translation. It concludes with reviewing the current evidence on targeting mitochondrial metabolism in cancer therapy.

The second chapter outlines the hypothesis and the scope of the current work, which ultimately aims at the identification and characterization of a novel molecule able to affect selectively the GSC component. Given the importance of functional mitochondrial translation for GSCs survival and based on the similarities existing between bacterial and mitochondrial ribosomes, the hypothesis underlying the whole project is the potential exploitation of bacterial ribosome targeting antibiotics as a tool to target mitochondrial translation and eradicate GSCs.

The results chapter describes how quinupristin/dalfopristin (Q/D) was selected among the different bacterial ribosome targeting antibiotics tested, how its effect on different GSCs, grown both in adherence and as neurospheres, was characterized, how its mechanism of action was studied and, lastly, how its efficacy *in vivo* was evaluated using a patient-derived GSCs xenograft mouse model.

The fourth chapter provides a discussion of the obtained results, with a special focus on the possible use of a combination of drugs acting on different levels of cellular metabolism or of drugs acting on GSCs and on the cells comprising the tumor bulk. Moreover, a discussion on blood-brain barrier (BBB) penetration and alternative routes of administration is provided.

The fifth chapter contains the main conclusions of the work.

The sixth chapter presents an overview of the ongoing work, which sets the basis for the future perspectives outlined in chapter seven.

The experimental procedures and methodologies used in this work are presented in chapter eight.

1. INTRODUCTION

1. 1 GLIOBLASTOMA MULTIFORME

Glioblastoma multiforme (GBM) is the most common and aggressive malignant primary brain tumor in adults, accounting for 47.1% of all malignant central nervous system (CNS) tumors and for the majority (56.1%) of all gliomas. It has an incidence rate of 3.2 per 100,000 people and a median age at diagnosis of 64 years (Brodbelt et al., 2015; Ostrom et al., 2017). Although the therapy involves radical treatments, such as surgical resection of the tumor followed by radiotherapy and chemotherapy, patients survive, on average, 12 to 15 months post-diagnosis, with a 5-year survival rate of 5.5% (Ostrom et al., 2017). GBM aggressively infiltrates normal surrounding brain parenchyma, rendering complete surgical resection very difficult. Temozolomide (TMZ) is currently the only chemotherapeutic drug used in the clinic in combination with radiotherapy to treat newly diagnosed GBM. TMZ increases the median survival of radiation treated patients from 12.1 months to 14.6 months (Stupp et al., 2005). Unfortunately, the tumor recurs, underlying the importance of developing new and more effective therapies. Strenuous efforts have been made in the past years to develop novel strategies to cure GBM, with unsuccessful outcomes (reviewed in Khosla, 2016).

1.1.1 The disease

GBM is a diffuse infiltrating form of glioma with predominantly astrocytic differentiation. It is classified as grade IV, the highest and most severe form accordingly to the World Health Organization (WHO) Classification of CNS Tumors (Louis et al., 2016). GBM is predominantly located in the supratentorial region, with the highest occurrence in the frontal lobe, followed by the temporal and parietal lobes (Larjavaara et al., 2007).

As the name implies, glioblastomas are a genetically and morphologically heterogeneous group of tumors, characterized by anaplasia, with nuclear and cellular pleomorphism, significant anisokaryosis and increased nuclear-cytoplasmic ratio. In addition, GBM tumors present pseudopalisading necrosis regions, as well as microvascular endothelial proliferation and atypical mitotic figures (reviewed in Urbanska et al., 2014). These tumors are extensively vascularized as a result of an overactivated angiogenesis, even though this process is often inefficient, leading to areas of hypoxia, necrosis, and edema (Ricci-Vitiani et al., 2010). **Figure 1.1** shows two magnetic resonance imaging (MRI) images of a 60-year-old male glioblastoma patient.

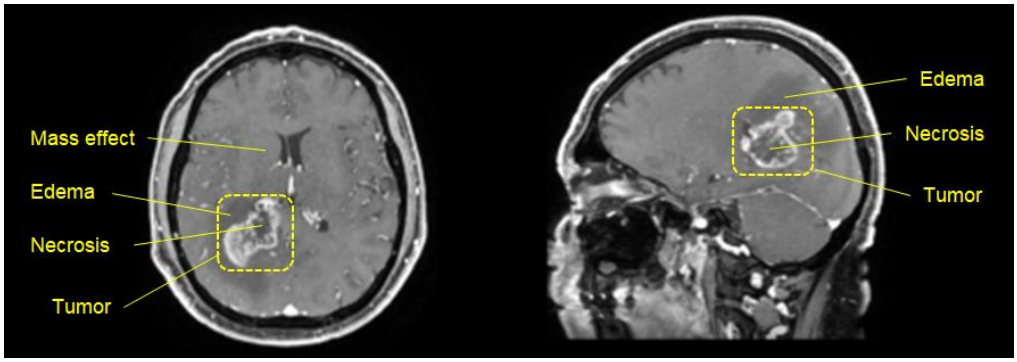

Figure 1.1 Primary glioblastoma multiforme. Axial T1 C+ fat saturated MRI (*left*) and Sagittal T1 C+ fat saturated (*right*) MRI images showing a mass abutting the right ventricular trigone and presenting peripheral enhancement and central necrosis. Case courtesy of A.Prof Frank Gaillard, Radiopaedia.org, rID: 37092.

From a genetic perspective, GBM are highly diverse, being characterized by an intra and inter-tumor heterogeneity. Typical molecular changes include various deletions, amplifications, and point mutations, which activate signal transduction in the receptor tyrosine kinase (RTK)/ RAS/ phosphoinositide 3-kinase (PI3K) signaling pathway, or disrupt the retinoblastoma (Rb) or the p53 signaling pathways, leading to uncontrolled proliferation, enhanced survival, angiogenesis and infiltration and decreased apoptosis induction (Brennan et al., 2013; McLendon et al., 2008). Based on characteristic gene expression signatures, GBM can be stratified into four distinct molecular subclasses: proneural, neural, classical and mesenchymal, each presenting different clinical behavior, prognosis and sensitivity to therapy. The proneural subtype correlates with a more favorable survival compared to the others, whereas tumors with a classical signature have been shown to respond better to concurrent radio and chemotherapy. Interestingly, GBM recurrence is often accompanied by a phenotypic shift toward the mesenchymal subtype, which represents the most aggressive one (Phillips et al., 2006; Verhaak et al., 2010).

According to another study based on global DNA methylation patterns GBM can be further stratified into six epigenetic subgroups: IDH, K27, G34, RTK I (PDGFRA), RTK II (Classic), and mesenchymal. Each group presents characteristic global DNA methylation patterns, specific hotspot mutations, DNA-copy-number alterations and transcriptomic patterns (Sturm et al., 2012). The six epigenetic groups identified correlate well with the previous described GBM classification. In detail, the IDH cluster displays proneural expression patterns, the K27 cluster also shows a clear enrichment of the proneural signature, the RTK II (Classic) cluster is enriched for “classical” expression profiles, the RTK I (PDGFRA) cluster is highly enriched for proneural expression, the mesenchymal cluster correlates with the mesenchymal gene expression cluster, and the G34 cluster presents a mixed gene

expression pattern (Sturm et al., 2012). According to these findings, this classification refines the previously reported one (Verhaak et al., 2010), further dividing the proneural subtype into subgroups with distinct genomic aberrations and adding new information for the other groups.

GBM stratification and a deep knowledge on the mutations characterizing the different tumor subgroups are fundamental and are at the basis for a “precision medicine” approach in the treatment of GBM. By knowing the molecular pathways altered in a specific subgroup, it is possible to rationally select the best therapeutic regimen for a given patient or to select the patients who could benefit the most from a given therapy (Prados et al., 2015). For example, it has been reported that EGFR-amplified/overexpressing glioblastoma patients strongly benefit from a metronomic administration of temozolomide (longer treatment compared to the standard schedule), with a strong increase in the patient overall survival (34 months for patients with high expression of EGFR *versus* 14 months for patients with low expression of EGFR) (Cominelli et al., 2015). Most probably, a combination of drugs targeting the multiple alterations present in a specific subgroup would represent the best therapeutic option (Prados et al., 2015).

According to the increasing importance of molecular-based stratification systems, the 2016 WHO Classification of CNS Tumors used for the first time molecular parameters in addition to histological features to classify brain tumors. In the case of GBM the parameter used to stratify patients by WHO is the presence or the absence of point mutations in the genes encoding for isocitrate dehydrogenase (IDH) (Louis et al., 2016). Therefore, the new classification recognizes two major entities for GBM: IDH-wt and IDH-mutant GBM (Louis et al., 2016). GBM IDH-wild type accounts for 90% of the cases and corresponds to the so-called "primary GBM". This GBM type occurs *de novo*, without evidence of a less malignant precursor. It is characterized by EGFR amplification or overexpression, with EGFRvIII being the most common mutation, PTEN mutation or deletion, and loss of chromosome 10. Giant cell glioblastoma, gliosarcoma and the epithelioid glioblastoma are included in this group (Louis et al., 2016; reviewed in Ohgaki and Kleihues, 2013). GBM IDH-mutant type accounts instead for the remaining 10% of the cases and corresponds to the so-called "secondary GBM". IDH1 mutation is associated with a better outcome and an increased overall survival. This GBM type develops from less malignant (low-grade) precursors, such as diffuse astrocytoma (WHO grade II) or anaplastic astrocytoma (WHO grade III). In addition to IDH mutations, TP53 mutations, and 19q loss have been observed (Louis et al., 2016; reviewed in Ohgaki and Kleihues, 2013).

1.1.2 The standard of care: radiotherapy plus temozolomide

The standard treatment for GBM patients involves neurosurgery followed by radiotherapy and temozolomide (TMZ) based-chemotherapy.

Surgical removal of the tumor represents the first line of treatment and has an immediate effect on patients' lives, including alleviation of tumor mass effects (i.e. reduction of the increased intracranial pressure and relief from symptoms, such as headache, nausea, vomiting), and reversal of neurological deficits, leading to an improvement in the quality of life. Whenever possible, a total removal of the tumor mass is recommended. In fact, although even a complete mass removal is not curative, it has been associated with a better outcome and quality of life, and a prolonged progression-free survival (Stummer et al., 2008). Given the highly infiltrative nature of GBM, total mass removal is not often feasible. Moreover, it is important to take into account the fine balance between the maximal removal of the tumor and the preservation of the neurological functions. To help neurosurgeons to maximize the extent of surgical resection, multiple tools have been developed in the last years, including intraoperative use of sophisticated imaging techniques, such as intraoperative magnetic resonance imaging (IoMRI) (Senft et al., 2011) and high field IoMRI (Mohammadi et al., 2014), as well as the development of novel tumor specific fluorescent agents, such as 5-aminolevulinic acid (5-ALA) (Hadjipanayis et al., 2015). 5-ALA is a newly FDA approved compound that, after oral administration, is able to cross the blood-brain barrier (BBB) and is metabolized by glioma cells to a fluorescent metabolite (protoporphyrin IX). The metabolite fluorescence allows tumor tissue visualization and localization in a real-time manner, so that the fluorescence-guided surgery permits a greater extent of resection (Hadjipanayis et al., 2015).

The second line of treatment for GBM patients is represented by radio and chemotherapy. In 2000-2002, Roger Stupp, in cooperation with the European Organization for Research and Treatment of Cancer (EORTC) Brain Tumor and Radiotherapy Groups and the National Cancer Institute of Canada (NCIC) Clinical Trials Group, performed a randomized phase III study for newly diagnosed GBM patients, comparing radiotherapy and concomitant temozolomide followed by 6 cycles of standard dose temozolomide versus radiotherapy alone (Stupp et al., 2005). This study showed that both the median survival and the overall survival were improved in patients treated with concomitant temozolomide (TMZ) compared to those of patients treated with radiotherapy alone (Stupp et al., 2005, 2009), as shown in **Table 1.1**.

Table 1.1 Median and overall survival for radiotherapy alone- or concomitant TMZ-treated patients

TREATMENT	MEDIAN SURVIVAL	OVERALL SURVIVAL			
		2 years	3 years	4 years	5 years
Radiotherapy	12.1	10.9%	4.4%	3.0%	1.9%
Radiotherapy + TMZ	14.6	27.2%	16.0%	12.1%	9.8%

Showing the clinically meaningful and statistically significant survival benefit given by TMZ, this research has become a landmark for the treatment of GBM. Nowadays, the "Stupp regimen" is the "standard of care" for newly diagnosed GBM patients. After neurosurgery, patients receive radiotherapy, consisting of fractionated focal irradiation at a dose of 2 Gy per fraction given once daily/five days per week over a period of six weeks, for a total dose of 60 Gy, with concomitant TMZ at a dose of 75 mg/m^2/day, given 7 days per week from the first day until the last day of radiotherapy. After a 4-week break, patients then receive up to six cycles of adjuvant TMZ for 5 days every 28 days. The dose of adjuvant TMZ is of 150 mg/m^2/day for the first cycle and then it is increased to 200 mg/m^2/day beginning with the second cycle (Strik et al., 2012; Stupp et al., 2005). Since TMZ is stable at acid pH, has a bioavailability approximately of 100% and, due to its lipophilic nature, is capable of crossing the blood-brain barrier (BBB), it is administered orally, in capsules. TMZ, whose structure is represented in **Figure 1.2**, is a pro-drug, which is spontaneously hydrolyzed to 5-(3-methyltriazen-1-yl)imidazole-4-carboxamide (MTIC) at physiological pH. MTIC is an alkylating agent, which is able to add a methyl group to purine bases of DNA, to form O^6-methylguanine, N^7-methylguanine and N^3-methyladenine, causing cell cycle arrest at G2/M and leading to apoptosis (Lee, 2016; Newton and Otero, 2015).

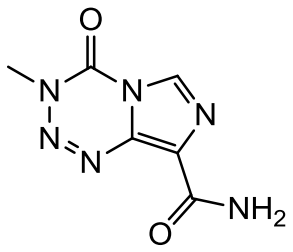

Figure 1.2 Temozolomide structure

The most widely studied mechanism of resistance to TMZ in GBM is the expression of the O^6-methylguanine DNA-methyltransferase (MGMT), a DNA repair protein able to remove methyl adducts from O^6-methylguanine and repair DNA damage, preventing the apoptotic effect of TMZ. The MGMT gene is epigenetically silenced in about 50% of GBMs by promoter methylation, resulting in increased sensitivity to TMZ. Although not sufficient, MGMT

promoter methylation is a relevant prognostic marker in predicting therapeutic response to TMZ (Crinière et al., 2007; Hegi et al., 2005). Nevertheless, given the lack of other therapeutic options for patients with unmethylated MGMT promoter, the clinical utility of MGMT remains poor. Recently, the addition of alternating electrical fields to maintenance TMZ chemotherapy has demonstrated a statistically significant improvement in progression-free and overall survival in newly diagnosed GBM patients (from 16 months to 20.9 months), according to a randomized prospective phase III trial (Stupp et al., 2015, *ibid.* 2017).

TMZ, concomitant and adjuvant to radiotherapy, is so far the only drug proved to prolong survival in newly diagnosed GBM, particularly with a methylated MGMT gene promoter. Yet, prognosis remains dismal, glioblastoma almost invariably recurs, and the patient survival remains very poor. When GBM recurs, there is not an established standard therapeutic regimen. Treatments differ between patients and include repeated surgery or radiotherapy and second-line therapies, such as nitrosoureas, antiangiogenic drugs, EGFR-targeted therapies or experimental protocols (Paolillo et al., 2018). Nevertheless, numerous experimental trials have failed to prolong survival and, despite all the new therapeutic attempts, only 5.5% of patients survive 5 years after diagnosis (Ostrom et al., 2017). Therefore, the development of new and more effective therapies is urgently needed.

1.2 GLIOBLASTOMA STEM CELLS (GSCs)

A major problem when treating GBM is that the tumor population is highly heterogeneous. Within the different cell types composing the tumor mass, the subgroup of glioblastoma stem cells (GSCs) is considered responsible for tumor initiation, progression, invasion, drug resistance and therefore disease recurrence (Bao et al., 2006; Chen et al., 2012; Galli et al., 2004; Singh et al., 2004). Hence, new therapies selectively targeting GSCs could lead to their eradication, preventing recurrence.

GSCs have been shown to depend on mitochondrial metabolism for their energy production. Inhibition of oxidative phosphorylation (OXPHOS), but not glycolysis, abolishes GBM cell clonogenicity (Janiszewska et al., 2012). Importantly, a high OXPHOS activity in GBM tumors, detected by measuring complex IV functionality, is a strong and independent negative prognostic factor for the overall survival of GBM patients (Griguer et al., 2013). The dependence of GSCs on mitochondrial activity suggests that inhibition of mitochondrial metabolism could become a new therapeutic approach in tumors (Marchetti et al., 2015). Therefore, OXPHOS undoubtedly represents an attractive target for the treatment of GBM, allowing to affect selectively the cancer stem cells compartment.

1.2.1 Stochastic *vs* Cancer Stem Cells (CSCs) model

GBM is characterized by a complex inter-patient as well as intra-tumor heterogeneity (Reardon and Wen, 2015). Intra-tumor heterogeneity refers to the presence of multiple and molecularly different cell subpopulations within the tumor. This has been demonstrated by Aubry and colleagues who showed that GBM biopsies taken from different zones of the same tumor present a molecularly heterogeneous signature (Aubry et al., 2015). This phenomenon contributes to tumor aggressiveness, chemotherapy resistance and disease relapse (Stieber et al., 2014; Yap et al., 2012).

As depicted in **Figure 1.3**, two models have been proposed to explain intra-tumor heterogeneity: a stochastic or clonal evolution model and a cancer stem cells (CSCs) hierarchy model.

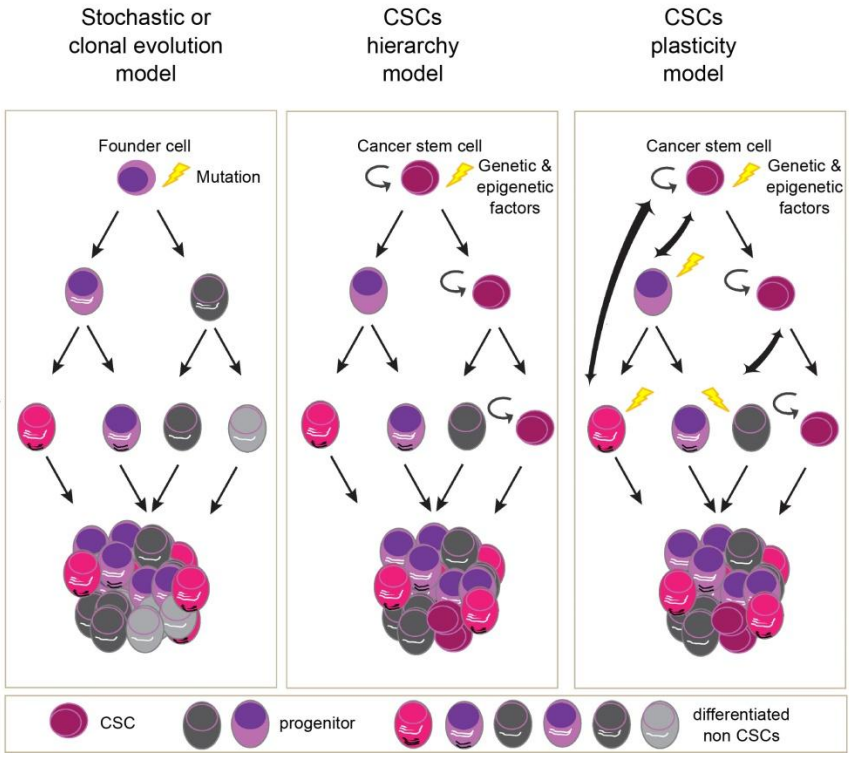

Figure 1.3 Representation of the different models of tumorigenesis. In the stochastic or clonal evolution model (*left*), all tumor cells are considered to arise from a single cancer cell and to possess equal tumorigenic potential, whereas according to the CSCs hierarchy model (*middle*) the tumor presents a hierarchical architecture, with a small population of highly tumorigenic CSCs, which are able to self-renew and to differentiate into all the phenotypically different cell types forming the tumor. The clonal evolution and the CSCs based models are not mutually exclusive. The CSC plasticity model (*right*) combines the previous two models, introducing the concept of dynamic stemness: under specific tumor micro-environmental stimuli, a non CSC can undergo a plasticity transition and reacquire CSC features and tumorigenic potential (adapted from Hamaï et al., 2014)**.**

In the clonal evolution model, first proposed by Prof. Nowell in 1976, a tumor arises from a single cell of origin endowed with growth advantages conferred by an oncogenic mutation. Genetically unstable daughter cells can acquire other genetic and epigenetic alterations, allowing subsequent selection of more aggressive subclones. Importantly, clonal selection can differ in time and space due to diverse stimuli and demands deriving from the different tumor areas. According to this theory, different subclones possess the same tumorigenic potential (Cabrera et al., 2015; Nowell, 1976; Rich, 2016). In the CSCs hierarchy model, instead, only a small subpopulation of stem cells is endowed with self-renewal properties and tumorigenic potential. CSCs proliferate consistently and are able to differentiate into all the phenotypically different cell types forming the tumor. As a result, tumors present a hierarchical architecture, comprising highly tumorigenic CSCs that proliferate and differentiate into intermediate progenitors and terminally differentiated non tumorigenic progeny. CSCs are, therefore, considered responsible for tumor initiation, progression, and heterogeneity (Cabrera et al., 2015; Lan et al., 2017; Rich, 2016).

The clonal evolution and the CSCs based models are not mutually exclusive. The progression of tumor heterogeneity is a complex process that could be explained by an alternative model, the so-called cancer stem cells plasticity model, able to combine the previously two theories. According to this model, several genetically distinct cancer stem clones deriving from a common ancestor may exist within a single tumor. Each cancer stem cell accumulates epigenetic and genetic alterations over time and, upon proliferation and differentiation, forms intermediate progenitors and terminally differentiated non tumorigenic progeny. The progenitors and the progeny can, under specific tumor micro-environmental stimuli, such as chemotherapeutic agents, undergo a plasticity transition and reacquire CSC features and tumorigenic potential (Auffinger et al., 2014; Cabrera et al., 2015; Rich, 2016).

1.2.2 GSCs identification and features

Glioblastoma stem cells (GSCs) were first identified in parallel by several groups at the beginning of 2000s (Galli et al., 2004; Ignatova et al., 2002; Singh et al., 2004; Yuan et al., 2004). GSCs are a minor fraction of cancer cells characterized by long-term proliferation and self-renewal capabilities, established through proliferation, subspheres formation and limiting dilution assays. Moreover, they are multipotent, being able to differentiate into the three major neural cell types, i.e. mature neurons, astrocytes and oligodendrocytes. Lastly, GSCs are able to establish tumors with all the GBM typical features upon xenograft transplantation into recipient mice. Singh *et al*. demonstrated that as few as 100 GSCs were enough for the establishment of a GBM tumor in immunocompromised mouse, whereas 100,000 non-GSCs

were not able to initiate tumor formation (Singh et al., 2004). GSCs features are summarized and represented in **Figure 1.4.**

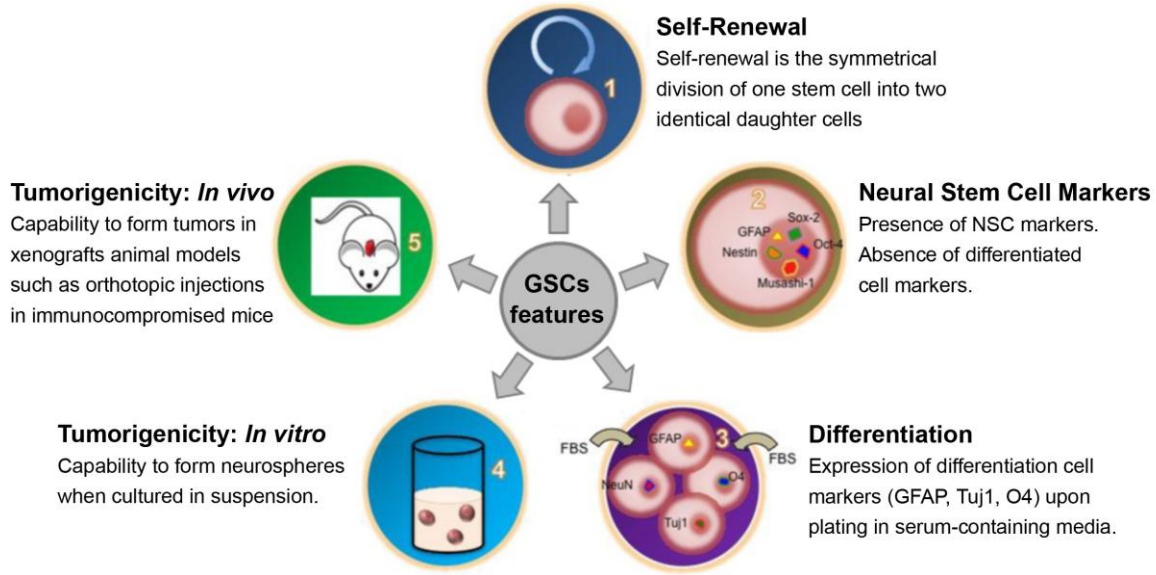

Figure 1.4 Glioblastoma stem cells' features. 1. Self-renewal. 2. Expression of neural stem cell markers. 3. Differentiation capability. 4. Long-term tumorigenic ability *in vitro*. 5. Capability to establish GBM tumors upon xenograft transplantation into recipient mice (adapted from Gürsel et al., 2011).

Culture conditions for GSCs isolation and expansion have been adapted from those originally used for neural stem cells (NSCs). Accordingly, GSCs are grown in suspension as neurospheres in serum-free medium, enriched with growth factors, such as epidermal growth factor (EGF) and fibroblast growth factor (FGF2) (Kim et al., 2015; Ledur et al., 2017). Alternatively, GSCs can be grown in adherence on laminin-coated flasks, allowing for uniform access to growth factors, suppression of differentiation and expansion of pure stem cell populations (Pollard et al., 2009). Despite the lack of a strict consensus due to significant inconsistency of marker expression among GBM tumors, GSCs can be identified and enriched using different cellular markers. Several surface markers have been proposed, such as CD133, CD44, SSEA-1, L1CAM, A2B5 and INTEGRIN α6 (reviewed in Brescia et al., 2012; Lathia et al., 2015), as well as typical NSCs markers that have been found widely expressed also in GSCs, i.e. SOX2, NESTIN, NANOG, OLIG2, MYC, BMI1, and MUSASHI1 (reviewed in Brescia et al., 2012; Lathia et al., 2015). Most probably, given the complex GBM heterogeneity, a single marker is not sufficient to identify GSCs in every tumor, but a combination of markers will possibly best define GSCs (reviewed in Brescia et al., 2012).

GSCs, as NSCs, reside in the so-called niches, which correspond to anatomical regions characterized by a unique microenvironment comprising tumor, glial and endothelial cells, blood vessels, infiltrating and resident immune cells (reviewed in Hambardzumyan and Bergers, 2015). GSCs interact dynamically with the niche, secreting factors that influence the microenvironment and being, in turn, influenced and maintained in a stem cell-like state by the niche signaling. Calabrese and colleagues showed for the first time that disruption of the niche microenvironment depletes GSCs and arrests tumor growth (Calabrese et al., 2007). Within a single tumor, morphologically and functionally distinct tumor niches exist. GBM displays three specialized tumor niches: the perivascular tumor niche, the hypoxic tumor niche, and the vascular invasive-tumor niche. In the perivascular tumor niche GSCs are located close to the endothelial cells that line capillaries and cause vascular basement membrane degradation by secreting vascular endothelial growth factor (VEGF), therefore resulting in abnormal, greatly enlarged vessels that are susceptible to leakiness and microhemorrhages. The hypoxic tumor niche presents a regressed or non-functional vasculature, leading to necrotic zones surrounded by hypoxic palisading tumor cells. GSCs are enriched in this sort of niches, because hypoxia promotes stemness and self-renewal and protects tumor cells from radio and chemotherapy. Finally, the vascular invasive-tumor niche is present at the outer edge of the tumor, where GSCs use the normal blood vessels to migrate and invade the surrounding normal parenchyma (reviewed in Hambardzumyan and Bergers, 2015; Sundar et al., 2014).

The poor prognosis associated to GBM is linked to therapeutic resistance and tumor recurrence. GSCs have been attributed a crucial role in resistance to radiotherapy and chemotherapy for several reasons. Firstly, O^6-methylguanine-DNA-methyltransferase (MGMT), the key repair enzyme for temozolomide induced DNA adducts, has been reported to be expressed at higher levels in GSCs as compared to non-stem cells (Liu et al., 2006). Bao *et al.* demonstrated that GSCs are capable of activating the DNA damage checkpoint response and to increase the DNA repair capacity following radiotherapy. Moreover, the CD133 marker positive cell fraction was shown to survive ionizing radiation and consequently, was enriched after radiotherapy both *in vitro* and *in vivo* (Bao et al., 2006). Chen and colleagues clarified that the subgroup of endogenous mouse tumor cells responsible for the regeneration of the tumor after TMZ treatment presents very similar properties to those proposed for GSCs (Chen et al., 2012). Finally, GSC population was shown to be increased after TMZ treatment, both *in vitro* and *in vivo* (Auffinger et al., 2014). This phenomenon was due to a phenotypic shift in the non-GSCs toward a stem cell state, supporting the GSCs plasticity model. The newly converted GSCs expressed stemness and

pluripotency markers and were able to generate tumors upon intracranial transplantation in recipient mice (Auffinger et al., 2014).

Based on the described evidence, GSCs are considered responsible for tumor initiation, progression, invasion, drug resistance and, thus, disease recurrence. Therefore, therapies targeting GSCs are very attractive for GBM treatment.

1.2.3 CSC and GSC metabolism

Altered metabolism is recognized as a developing hallmark of cancer (Hanahan and Weinberg, 2011). For many decades, tumor metabolism has been thought to heavily rely on aerobic glycolysis, a phenomenon known as the "Warburg effect" (Warburg, 1956). In the past years, some studies have supported the "Warburg effect", showing an increased glycolysis and a reduced mitochondrial oxidative phosphorylation (OXPHOS) capacity but other studies have demonstrated that mitochondria and OXPHOS play an essential role in tumorigenesis and tumor progression (reviewed in Jose et al., 2011; Moreno-Sánchez et al., 2014). Early evidence on the importance of mitochondria in tumorigenesis came from experiments performed on rho^0 cells which, devoid of any mitochondrial DNA and consequently having a reduced OXPHOS activity, demonstrated a dramatic reduction in tumorigenic potential and increased vulnerability to cytotoxic drugs (Cavalli et al., 1997; Hayashi et al., 1992). These results have been recently supported by a study based on melanoma and breast cancer rho^0 cells (Tan et al., 2015).

It has become clear that the bioenergetic profile of tumors is variable, with inter- and intra-tumor differences in glycolytic and mitochondrial metabolism. Cancer cells continuously reprogram their metabolism to adapt to environmental pressures and metabolic flexibility is an established cancer feature (reviewed in Berridge et al., 2010; DeBerardinis and Chandel, 2016; Pavlova and Thompson, 2016). Despite Warburg's first statement about the mitochondrial respiration impairment in cancer cells ("...the respiration of all cancer cells is damaged...(which) must be irreversible since...never returns to normal", Warburg, 1956), it has been demonstrated that mitochondria and OXPHOS play an essential role in cancer, with OXPHOS being the major source of ATP in many cancer types, even in the presence of enhanced rate of glycolysis (reviewed in Moreno-Sánchez et al., 2014; Zu and Guppy, 2004).

Accumulating evidence suggests that the cancer stem cell (CSC) subpopulations rely on mitochondrial respiration for their energy demand (reviewed in Sancho et al., 2016; Viale et al., 2015). The OXPHOS dependence has been proven for CSCs of various tumor types, including leukemia, breast, pancreatic and ovarian cancer (Pastò et al., 2014; Sancho et al.,

2015; Škrtić et al., 2011; Viale et al., 2014; Vlashi et al., 2014). GSCs have also been demonstrated to rely on OXPHOS. Vlashi and colleagues showed that the metabolic state of GSCs differs from that of the tumor bulk, with GSCs being less glycolytic and having higher mitochondrial OXPHOS capacity compared to differentiated counterpart (Vlashi et al., 2011). Janiszewska *et al.* demonstrated that GSCs depend on OXPHOS for their energy demand and survival and that inhibition of OXPHOS suppresses cell clonogenic potential. They associated the oncofetal insulin-like growth factor 2 mRNA-binding protein 2 (IMP2) to OXPHOS regulation and maintenance, proving that IMP2 delivers complex IV chain subunit-encoding mRNA to mitochondria and, at the same time, binds and interacts with two nuclearly-encoded subunits of complex I, NDUFS3 and NDUFS7, which are part of the subcomplex form of complex I in early assembly. They hypothesized that IMP2 could function as a complex I chaperone, facilitating the assembly and/or the translocation of the subcomplex form of complex I into mitochondria while at the same time delivering complex IV chain subunit-encoding mRNA. Depletion of IMP2 in GSCs resulted in a decrease oxygen consumption rate and in a subsequent diminished tumorigenesis *in vitro* and *in vivo* (Janiszewska et al., 2012). Increased complex IV activity in tumors has been associated with tumor progression after chemotherapy failure. Pharmacological or genetic inhibition of complex IV, which is overexpressed in TMZ resistant cells, reverts TMZ chemoresistance (Oliva et al., 2010, 2011). Importantly, a high OXPHOS activity in GBM tumors, detected by measuring complex IV functionality, is a strong and independent negative prognostic factor for the overall survival of GBM patients. Patients with low complex IV activity survived, on average, for 14.3 months, whereas the median survival time for patients with high complex IV activity was 6.3 months (Griguer et al., 2013). Recently, the FGFR3-TACC3 (F3-T3) gene fusion, described in a small subset of human GBM cases (3%) (Singh et al., 2012), have been shown to induce mitochondrial biogenesis and to activate OXPHOS (Frattini et al., 2018).

1.3 OXPHOS AND MITOCHONDRIAL TRANSLATION

Mitochondria are cytoplasmic organelles involved in a variety of cellular metabolic functions, essential for cellular homeostasis maintenance (McBride et al., 2006). Due to the fundamental role played in energy production, mitochondria are often referred as the “powerhouse” of the cell. In fact, among many other cellular functions, mitochondria are responsible for ATP synthesis, which takes place through the oxidative phosphorylation (OXPHOS) process.

The essential protein core of OXPHOS consists of five multi-subunit complexes, namely I, II, III, IV and V, located within the inner mitochondrial membrane. In order to assemble each complex (with the exception of complex II), genes from the mitochondrial and nuclear genomes have to be coordinately expressed. The mitochondrial genome encodes only 13 out of all the proteins forming these complexes (Anderson et al., 1981). The 13 mtDNA-encoded proteins are translated by the mitochondrial translation system on the mitochondrial ribosomes, also called mitoribosomes (O'Brien, 1971). Therefore, inhibition of mitochondrial translation would hamper OXPHOS complexes formation, leading to impairment of complexes functionality and ATP production and finally resulting in cellular detrimental effects.

1.3.1 The oxidative phosphorylation process

The oxidative phosphorylation (OXPHOS) represents the last step of the cellular respiration process and it is endowed with a high capacity of ATP production, quantified in almost 30 ATP molecules per one molecule of glucose (Rich, 2003). The concept of oxidative phosphorylation was first proposed by Prof. David Keilin (Keilin, 1925; Keilin 1966) and its mechanism was elucidated by Prof. Peter Mitchell (Mitchell, 1961), who in 1978 won the Nobel Prize in Chemistry for his contribution to the understanding of biological energy transfer through the formulation of the chemiosmotic theory.

OXPHOS is the metabolic pathway that couples the sequential transport of high-energy electrons through the electron transport chain (ETC) to the synthesis of ATP driven by the so-called chemiosmosis process. During OXPHOS, electrons derived from NADH and $FADH_2$, produced in the previous steps of cellular respiration, are gradually transferred to molecular O_2 *via* a series of transmembrane protein complexes comprising the ETC. In detail, in the ETC electrons are transferred sequentially from an electron donor molecule to a more electronegative electron acceptor molecule, which then acts as electron donor towards a more electronegative electron acceptor molecule till the electrons are transferred to O_2, the ultimate electron acceptor. The energy released in the electron transfer promotes the transport of H^+ through the mitochondrial inner membrane toward the intermembrane space, with the generation of an electrochemical gradient, which, in turn, drives the synthesis of ATP from ADP through a process called chemiosmosis (Mitchell, 1961).

The electron transport chain (ETC) is composed of four transmembrane multi-subunit complexes, namely I, II, III, and IV, located within the inner mitochondrial membrane. At the end of the ETC, ATP synthase or complex V is responsible for ATP synthesis (**Figure 1.5**).

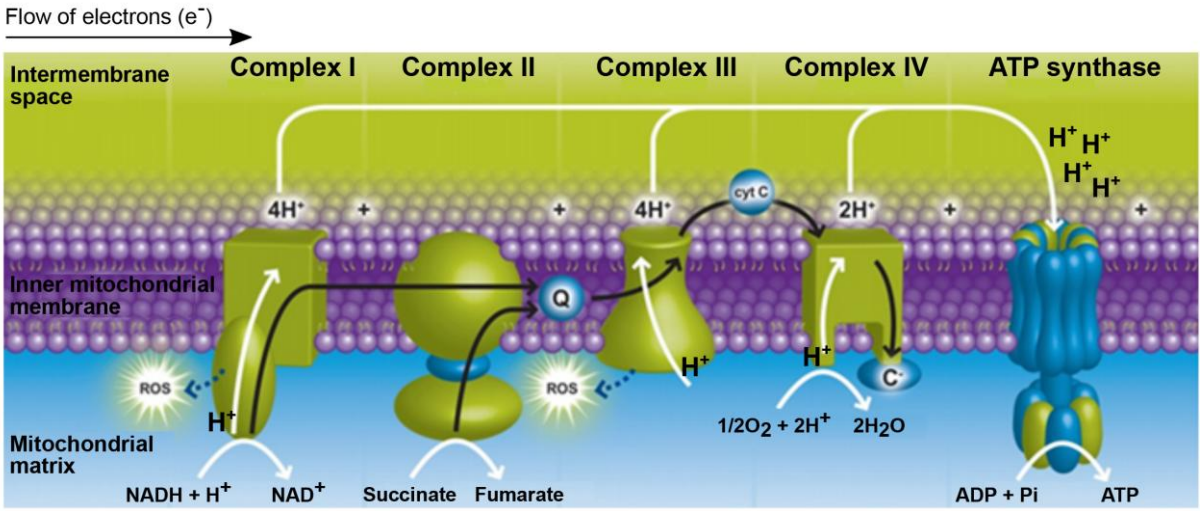

Figure 1.5 Oxidative phosphorylation chain. The oxidative phosphorylation (OXPHOS) chain consists of five multi-subunit complexes, located in the mitochondrial inner membrane. Complex I, II, III and IV are responsible for the sequential transport of high-energy electrons deriving from NADH, $FADH_2$ to molecular O_2 and for the generation of an electrochemical gradient, which, in turn, drives the synthesis of ATP by ATP synthase (or complex V) through a process called chemiosmosis (Adapted from Abcam oxidative phosphorylation).

Complex I, also known as NADH dehydrogenase or NADH-ubiquinone oxidoreductase, is the first enzyme of the respiratory chain. It is composed of 45 protein subunits and catalyzes the transfer of two electrons from NADH to ubiquinone (also called coenzyme Q). These electrons are initially transferred from NADH to flavin mononucleotide (FMN) and then, through an iron-sulfur carrier, to ubiquinone that is reduced to ubiquinol. The redox energy released during this process is used by complex I to translocate protons from the mitochondrial matrix toward the intermembrane space. Therefore, complex I acts as a proton pump, translocating 4 H^+ for each electron pair transferred from NADH to ubiquinone, and contributing to the generation of the electrochemical gradient (reviewed in Hirst, 2013).

Complex II, also called succinate dehydrogenase or succinate-CoQ reductase, is the only complex of the ETC to be entirely nuclearly encoded. It consists of 4 polypeptides and catalyzes the transfer of two electrons from $FADH_2$, produced in the Krebs cycle from the oxidation of succinate, to ubiquinone. Complex II permits the transfer of electrons to ubiquinone in parallel to complex I. However, this mechanism is not associated with a significant decrease in free energy and H^+ are not pumped across the membrane at this level (reviewed in Cecchini, 2003).

Ubiquinone, which receives electrons from complexes I and II, is a lipid-soluble molecule that is able to freely diffuse within the membrane transferring electrons to complex III. Complex III, also known as ubiquinone-cytochrome *c* oxidoreductase, is composed of 11 protein subunits and catalyzes the reoxidation of ubiquinol with the sequential transfer of electrons to the cytochrome *c*, a water-soluble electron carrier bound to the outer face of the mitochondrial inner membrane. Complex III acts also as a proton pump, translocating 4 H^+ to the intermembrane space and contributing to the generation of the electrochemical gradient (Berry et al., 2000; Lange and Hunte, 2002).

Complex IV, also called cytochrome *c* oxidase, is the last electron carrier of the ETC. It consists of 13 protein subunits and catalyzes the transfer of electrons from cytochrome *c* to molecular oxygen O_2, with the formation of water. Four electrons are required to reduce each molecule of O_2, and two water molecules are formed in the process. At the same time, complex IV acts as proton pump, pumping 2 H^+ into the intermembrane space for each electron pair transferred and contributing to the generation of the electrochemical gradient (reviewed in Richter and Ludwig, 2003). The electrochemical gradient generated by proton translocation across the inner membrane establishes a proton-motive force, which is characterized by two components: a difference in electric potential (ΔΨ) and a difference in proton concentration (Δ pH). Given the highly hydrophobic core of the inner membrane phospholipid bilayer, protons cannot diffuse down-gradient back into the matrix, but they need a channel protein forming a hydrophilic tunnel across the membrane. ATP synthase, or complex V, is composed of 17 polypeptides, which constitute two functional domains: the F_1 domain, which is a water-soluble portion located in the mitochondrial matrix, and the F_0 domain, which, instead is located in the inner mitochondrial membrane. The F_0 domain allows protons to flow down the electrochemical gradient, and the energy released in this process causes rotation of two rotary motors: the ring of c subunits in F_0 (relative to subunit a), along with subunits γ, δ and ε in F_1, to which it is attached. The rotation is coupled to the synthesis of ATP from ADP and inorganic phosphate (P_i) in the F_1 sector. ATP is then released into the mitochondrial matrix (reviewed in Walker, 2013).

This entire process constitutes OXPHOS. Overall, OXPHOS produces 5 molecules of ATP per every two molecules of NADH (4 electrons) oxidized by one molecule of O_2. This balance represents the maximal efficiency achievable by OXPHOS. Under certain physiological conditions the efficiency of OXPHOS can decrease, due to the leaking of the ETC chain (reviewed in Papa et al., 2012).

As said, each OXPHOS complex comprises different protein subunits. In order to form each complex, with the exception of complex II, genes from the mitochondrial and nuclear

genomes have to be coordinately expressed and assembled. **Table 1.2** summarizes the nuclear and mitochondrial protein contribution to each OXPHOS complex.

Table 1.2 Nuclear and mitochondrial protein contribution to each OXPHOS complex

	Subunits	Polypeptides encoded by mtDNA	Polypeptides encoded by nuclear DNA
Complex I NADH dehydrogenase	45	7	38
Complex II Succinate ubiquinone oxidoreductase	4	0	4
Complex III Ubiquinol Cytochrome *c* oxidoreductase	11	1	10
Complex IV Cytochrome *c* oxidoreductase	13	3	10
Complex V ATP synthase	17	2	15

1.3.2 Mitoribosomes and mitochondrial translation

According to the endosymbiotic theory, mitochondria arose from an α-proteobacterial ancestor, which was engulfed by an eukaryotic cell 1.45 billion years ago (Gray, 2012; Gray et al., 1999; Sagan, 1967). Although the majority of the mitochondrial proteins are encoded by nuclear genes, mitochondria have conserved their own DNA (mtDNA), and their own transcriptional and translational apparatus systems. The human mitochondrial DNA (mtDNA) is a double-stranded, circular molecule of 16.5 kb containing 37 genes, which code for 13 polypeptides translated from 11 mt-mRNA species (9 monocistronic and 2 bicistronic), two mt-rRNAs and 22 mt-tRNAs (Anderson et al., 1981, **Figure 1.6**). All the 13 mtDNA-encoded polypeptides are highly hydrophobic protein subunits of the OXPHOS complexes and are synthesized by the mitochondrial translation system on the mitoribosomes.

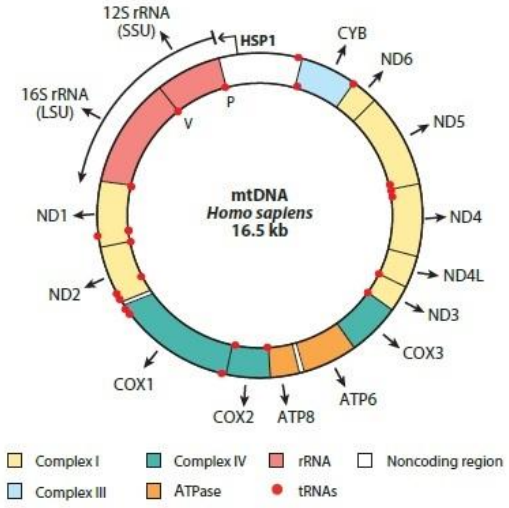

Figure 1.6 Mitochondrial genome. MtDNA codes for 13 polypeptides, two mt-rRNAs and 22 mt-tRNAs (adapted from Ott et al., 2016).

The human mitoribosome is a large ribonucleoprotein complex composed of 82 proteins and three ribosomal RNA species (Amunts et al., 2015). Each mitoribosome comprises a small ribosomal subunit (28S, mt-SSU) and a large ribosomal subunit (39S, mt-LSU) (O'Brien, 1971). The small ribosomal subunit is believed to be involved in messenger RNAs (mRNAs) binding and deciphering through selection of the cognate aminoacyl–transfer RNA (aa-tRNA) molecules. On the other hand, the large subunit is involved in peptide bond formation, which is catalyzed by the peptidyl transferase center (PTC) (Ban et al., 2000; Nissen et al., 2000).

Models of the mammalian 55S mitoribosome and its subunits approaching full atomic resolution were published in 2014 and 2015 (Amunts et al., 2015; Brown et al., 2014; Greber et al., 2014b, 2014a, 2015), allowing for the building of near-complete models of the 16S and 12S mitoribosomal RNAs and the assignment of all mammalian mitoribosomal proteins.

Compared to the ancestral bacterial ribosome, the mitoribosome presents a different overall appearance that reflects structural changes occurred through evolution, including ribosomal RNA reduction and gain of mitochondrial-specific ribosomal proteins. 36 out of the 82 mitoribosomal proteins are mitochondrial-specific, 22 located in the 39S subunit (Greber et al., 2014a) and 14 in the 28S subunit (Amunts et al., 2015). The mitoribosomal-specific proteins have been suggested to structurally compensate for the interactions mediated by missing rRNA segments, as observed in the region around uL24m (Greber et al., 2014b), and to provide additional functions, such as membrane association (Greber et al., 2014b) and mRNA recruitment (Amunts et al., 2015; Greber et al., 2014a). 5S rRNA, a fundamental component of bacteria ribosome, is absent from the 55S mitoribosome. Interestingly, in the cryo-EM structure of the 39S subunit, a tRNA molecule was detected in the central protuberance (CP) in a location close to the position of domain β of 5S rRNA in bacteria (Greber et al., 2014b). The tRNA molecule, which was termed CP tRNA, interacts with several ribosomal proteins at the CP, architecturally substituting for the absence of the 5S rRNA (Greber et al., 2014b) and functioning as a stable structural scaffold to organize the structure of the CP (Greber et al., 2014a).

Although mitochondrial rRNA is encoded by the mitochondrial genome, interestingly, all 82 mitoribosomal proteins are nuclear-encoded, translated in the cytosol and imported into the mitochondrial matrix (reviewed in Neupert, 2015).

Despite these evolutionary changes, the mitoribosome still shares several similarities with its bacterial ancestors. In fact, the functional mitoribosomal core comprising the codon-recognition sequences on the mt-SSU and the peptidyl transferase centre (PTC) in the mt-LSU has been conserved (Amunts et al., 2015; Brown et al., 2014; Greber et al., 2014b, 2014a, 2015). Moreover, the presence of the E-site in human mitoribosomes has been confirmed (Amunts et al., 2015). Mitoribosome have been found attached to the mitochondrial inner membrane (Englmeier et al., 2017; Liu and Spremulli, 2000), where the

hydrophobic proteins they synthesize through mitochondrial translation can be directly inserted and be assembled with the nuclear-encoded proteins to form the multi-subunit OXPHOS complexes.

Mitochondrial translation, as the bacterial and cytosolic translation, can be divided into four main steps (reviewed in Christian and Spremulli, 2012; Hällberg and Larsson, 2014; Mai et al., 2017; Ott et al., 2016). A representative description of the mitochondrial translation process is depicted in **Figure 1.7**. Each step is performed within the mitoribosome, which operates in conjunction with several translation factors.

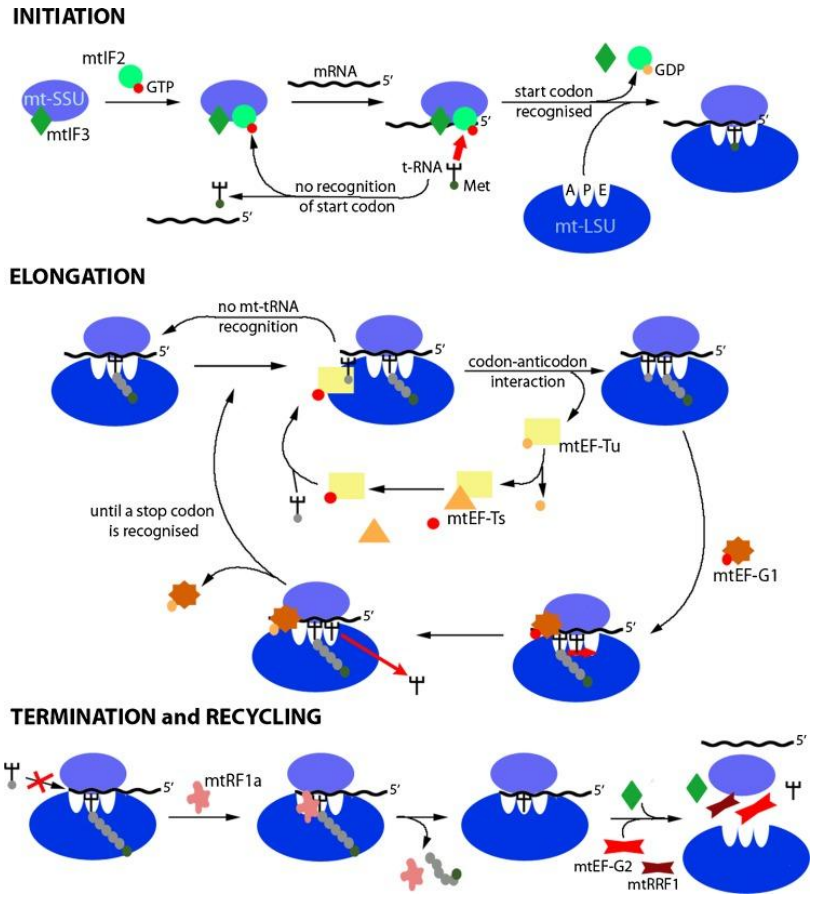

Figure 1.7 Mitochondrial translation process. Mitochondrial translation starts with the initiation step, where an mt-encoded mRNA is recruited and loaded onto the ribosomal small subunit and subsequently a start codon is selected and recognized by the initiator mt-tRNA (fMet-tRNA), which carries a formylated methionine. The second step of translation is represented by elongation. Here, the codons in the mRNA are read sequentially and the cognate amino acids are integrated into the nascent polypeptide chain. The elongation cycle is then repeated several times, until the polypeptide chain is completed and a stop codon is positioned in the A site, with translation termination. The nascent chain then leaves the ribosome through the exit tunnel and is inserted in the mitochondrial inner membrane. Finally, the recycling step restores mt-SSU and mt-LSU (Figure credit: Mai et al., 2017).

Mitochondrial translation starts with the initiation step, where a mt-encoded mRNA is recruited and loaded onto the ribosome and subsequently a start codon is selected and recognized by the initiator mt-tRNA (fMet-tRNA). Unlike bacteria, mitochondria contain only two initiation factors (IFs), namely mtIF2 and mtIF3. A homolog of the "universal" translation initiating factor IF1 has never been observed in mitochondria; however the mtIF2 possesses a region which has been shown to be functionally equivalent to IF1 (Gaur et al., 2008). Therefore, it is thought that mtIF2 plays the role of two bacterial initiating factors (IF1 and IF2). MtIF2 presents a molecule of GTP bound to its structure (mtIF2:GTP), which is important for its function (Spencer and Spremulli, 2005). Mitochondrial initiation starts when mtIF3 binds the mitochondrial small subunit (mt-SSU) preventing premature reassociation of the mt-SSU to the mt-LSU (Koc and Spremulli, 2002). The mt-SSU mtIF3 complex is then bound by a molecule of mtIF2:GTP, followed by the recruitment of a mt-mRNA to the mt-SSU and the placement of the start codon in the P site of the mt-SSU. The majority of the mitochondrial mRNAs are almost completely leaderless, therefore lacking the canonical Shine–Dalgarno sequence located in the 5' untranslated region (5'UTR) typical of bacterial transcripts (Montoya et al., 1981; reviewed in Temperley et al., 2010). For these mRNA species, the start codon is at or very near the 5' end of the mRNA, with a maximum of 3 nucleotides preceding the start codon. In the case of the ND4L/ND4 and ATP8/ATP6 bicistronic mRNAs, instead, two 5'UTRs of 296 and of 161 nucleotides are present preceding the open reading frame (ORF) encoding for ND4 and for ATP6 respectively (Montoya et al., 1981; reviewed in Temperley et al., 2010). The starting codons used in mammalian mitochondria are represented by the most common AUG, but also by AUA and AUU (Anderson et al., 1981). MtIF2:GTP favors the recognition of the start codon in the P site of the mt-SSU by the initiator mt-tRNA which carries formylated methionine (*f*Met-tRNA^{Met}) (reviewed in Christian and Spremulli, 2012). Once this step has been completed successfully, the GTP bound to mtIF2 is hydrolyzed to GDP, the IFs are released and, thus, the mitochondrial large subunit (mt-LSU) can associate to the mt-SSU, forming the mitochondrial monosome (reviewed in Christian and Spremulli, 2012).

The second step of translation is represented by elongation. Here, the codons in the mRNA are read sequentially and the cognate amino acids are integrated into the nascent polypeptide chain. In this phase, the elongation factor Tu (mtEFTu) bound to a molecule of GTP forms a ternary complex with an aminoacyl-tRNA (aa-tRNA), and this ternary complex enters the A site of the mitoribosome. If a correct codon-anticodon pair forms, GTP is hydrolyzed to GDP, with the subsequent release of mtEFTu:GDP from the mitoribosome. The elongation factor Ts (mtEFTs) mediates the exchange of GDP for GTP on mtEFTu, with mtEFTu:GTP complex restoration (Cai et al., 2000). The formation of the peptide bonds between the amino acids carried by the aa-tRNA present in the A and P sites is catalyzed by

the peptidyl transferase center (PTC) in the mt-LSU (Nissen et al., 2000). In detail, the PTC catalyzes the transfer of the peptide chain of the tRNA in the P site on the aa-tRNA newly entered in the A site, elongating the peptide chain by one amino acid. Subsequently, the mitochondrial elongating factor G1 (mtEFG1) favors the translocation of the peptidyl-tRNA from the A site to the P site, with the simultaneous movement of the deacylated tRNA from the P to the E site (Bhargava et al., 2004; reviewed in Spremulli et al., 2004). The presence of the E-site in human mitoribosomes has been recently confirmed (Amunts et al., 2015). The elongation cycle is then repeated several times, until the polypeptide chain is completed and a stop codon is positioned in the A site, with translation termination. In mammalian mitochondria the stop codons are represented by the triplets UAA and UAG. When a stop codon is located in the A site, it is recognized by the mitochondrial release factor 1a protein (mtRF1a) (Soleimanpour-Lichaei et al., 2007), which mediates the hydrolysis of the ester bond between the nascent polypeptide chain and the last mt-tRNA, resulting in the release of the nascent polypeptide. The nascent chain then leaves the ribosome through the exit tunnel and is inserted in the mitochondrial inner membrane.

Finally, the recycling step restores mt-SSU and mt-LSU. After chain release, two recycling factors, the mitochondrial ribosome recycling factors 1 and 2 (mtRRF1 and mtRRF2) favor the dissociation of the two ribosomal subunits, and the release of mt-mRNA and decylated mt-tRNA (Rorbach et al., 2008; Tsuboi et al., 2009). Re-association of the mt-SSU and mt-LSU is prevented by the formation of an mtIF3:mt-SSU complex.

1.4 TARGETING MITOCHONDRIAL METABOLISM IN CANCER THERAPY

The strong reliance of cancer stem cells on mitochondrial activity for their energy demand (reviewed in Sancho et al., 2016; Viale et al., 2015) suggests that mitochondrial metabolism could represent a new therapeutic target in tumors (reviewed in Ashton et al., 2018; Marchetti et al., 2015; Martinez-Outschoorn et al., 2017; Weinberg and Chandel, 2015). Key experiments supporting this idea have been published in the last years and some molecules able to interfere with mitochondrial metabolism are already in clinical trials as anti-cancer agents (Kuntz et al., 2017; Molina et al., 2018; Ravà et al., 2018; Reed et al., 2016).

The most studied example is represented by the anti-diabetic drug metformin, which has been shown to reversibly inhibit OXPHOS complex I (Wheaton et al., 2014), resulting in cytotoxic effects in different cancer stem cell lines, including breast (Song et al., 2012), pancreatic (Gou et al., 2013), colon (Zhang et al., 2013) and also glioblastoma (Würth et al., 2013). In addition, epidemiological studies have pointed out that diabetic patients taking

metformin are less susceptible to develop cancer (Evans et al., 2005) and that those who have already developed cancer and take metformin have an increased survival rate (Tan et al., 2011). Metformin is currently in hundreds of ongoing clinical trials to evaluate its antineoplastic therapeutic efficacy. Like metformin, the more lipophilic biguanide phenformin has also shown anti-cancer properties by inhibiting complex I (Appleyard et al., 2012; Birsoy et al., 2014). Atovaquone is a FDA approved naphtoquinone with antipneumocystic and antimalaric activity (Nixon et al., 2013). It is an ubiquinone analogue able to inhibit complex III in parasites but also in breast cancer cell lines, resulting in MCF7-derived CSCs propagation inhibition and apoptosis induction (Fiorillo et al., 2016). Inhibition of complex IV has also been demonstrated to have potential therapeutic effects in cancer treatments. Among others, Oliva and colleagues have recently shown encouraging results for two different small molecule inhibitors of complex IV in GBM (Oliva et al., 2016, *ibid*. 2017). Both molecules were able to significantly inhibit GSC proliferation and to decrease the size and volume of tumor-treated mice xenografts (Oliva et al., 2016) and to increase the median overall survival of treated mice (Oliva et al., 2017).

Beside OXPHOS complexes inhibitors, there are many other molecules able to interfere with mitochondrial metabolism at different levels (reviewed in Marchetti et al., 2015; Weinberg and Chandel, 2015). Several antibiotic classes developed to target bacterial ribosome have shown mitochondrial toxicity due to their off-target on mitochondrial ribosomes (Greber and Ban, 2016; Guan, 2011; Soriano et al., 2005; De Vriese et al., 2006; Zhang et al., 2005). The off-target effects of bacterial ribosome targeting antibiotics are easily explained on the basis of the mitochondrial evolutionary origin and on the fact that the functional mitoribosomal core has been preserved during evolution (Amunts et al., 2015; Brown et al., 2014; Greber et al., 2014b, 2014a, 2015). The similarity between the mitochondrial and the bacterial translation systems sets the basis for the potential exploitation of ribosome-targeting antibiotics as inhibitors of mitochondrial translation and, hence, as agents interfering with OXPHOS functionality in tumors. This rationale has already produced interesting results for acute myeloid leukemia (AML) (Škrtić et al., 2011), where the glycylcycline tigecycline was able to selectively kill leukemia stem cells and to decrease tumor mass in xenografts mice models. These promising results have led to a phase I clinical trial with 27 adult patients with relapsed and refractory AML (Reed et al., 2016). This study established the maximum tolerated dose (300 mg/day) but unfortunately did not show significant clinical response in patients (Reed et al., 2016), suggesting the need to find drug schedules that permit more sustained target inhibition.

Very recently, William *et al.* showed that doxycycline, another tetracycline antibiotic, prevents TMZ-induced increase of GSCs tumorigenicity (William et al., 2018), supporting the idea of mitochondrial translation inhibition as anti-cancer targeted therapy in GBM.

2. HYPOTHESIS AND AIMS

Glioblastoma multiforme (GBM) is the most common and aggressive primary brain tumor in adults, with a median survival of 15 months post-diagnosis and a 5-year survival rate of 5.5%. The sole clinically available drug, temozolomide, prolongs life of 2.5 months only. Therefore, novel therapeutic approaches are urgently needed. Given the aggressive nature of the glioblastoma stem cell (GSC) component that is responsible for tumor initiation, progression, invasion, drug resistance and consequently disease recurrence, novel therapies should aim at specifically targeting and eradicating this cell population.

Recent evidence has shown that GSCs, as well as other cancer stem cells, rely on mitochondrial oxidative phosphorylation (OXPHOS) for their high energy demand. Importantly, a high OXPHOS activity in GBM tumors is a strong and independent negative prognostic factor for GBM patients' overall survival. Therefore, OXPHOS is undoubtedly an attractive target in the treatment of GBM. The essential protein core of OXPHOS components is assembled with the contribution of proteins translated by the mitochondrial ribosomes. According to the endosymbiotic theory, mitoribosomes are known to derive from a bacterial ancestor. Despite the evolutionary changes occurred, the functional mitoribosomal core of the mitoribosome, comprising the codon-recognition sequences on the mt-SSU and the peptidyl transferase centre (PTC) in the mt-LSU has been conserved. In the light of the similarities shared by the mitoribosome and its bacterial ancestors, bacterial ribosome targeting antibiotics could be exploited to inhibit mitoribosome, affecting mitochondrial translation and OXPHOS assembly, and hence leading to detrimental effect on GSCs viability.

Based on this hypothesis, this study aimed at:

- identifying one or more molecules among the different classes of bacterial ribosome targeting antibiotics endowed with a mitotoxic and cytotoxic potential on GSCs, using both high- and low-throughput screening approaches.
- characterizing the mechanism of action of the selected molecule using different molecular assays.
- validating the potential anticancer activity of the selected molecule *in vivo* using a patient-derived GSCs xenograft mice model.

Considering the urgent medical need for novel therapeutic approaches in the context of GBM treatment, the ultimate ambitious goal of this project was to provide a new candidate molecule for further preclinical and clinical evaluation.

3. RESULTS

3.1 A HIGH-CONTENT SCREENING IDENTIFIES STREPTOGRAMINS AS THE MOST EFFECTIVE CLASS TARGETING GSCS

3.1.1 The Model

In order to identify a bacterial ribosome-targeting antibiotic class able to induce cyto- and mito-toxicity in glioblastoma stem cells (GSCs), we decided to perform a high-content imaging screening using two GSC lines, namely COMI and VIPI.

COMI and VIPI cell molecular characterization

COMI and VIPI lines, whose isolation and characterization have been previously reported (Ropolo et al., 2009; Vecchio et al., 2014, 2015), were a kind gift from Dr. Antonio Daga (Azienda Ospedaliera Universitaria San Martino di Genova, Italy). These lines derive from two male patients diagnosed with grade IV GBM and have both been classified as belonging to the RTK II (Classic) cluster according to their EGFR amplification (Vecchio et al., 2015). Biological grouping performed by Vecchio *et al.* was based on correlations with mutational status and DNA copy number variations of the main genes, TP53, IDH1, H3F3A, EGFR, PDGFRA and CDKN2A, which characterize the subgroups proposed by Sturm *et al.* (Sturm et al., 2012). **Table 3.1** reports COMI and VIPI biological group characterization performed by Vecchio and colleagues (Vecchio et al., 2015).

Table 3.1 COMI and VIPI biological group characterization [a)]

CELLS	Biological Group	TP53	IDH1	H3F3A	EGFR	PDGFRA	CDKN2A
COMI	RTK II (Classic)	wt	wt	wt	Ampl	wt	Del
VIPI	RTK II (Classic)	mut	wt	wt	Ampl	wt	Del

a) Wt: wild type; mut: mutation or copy number variations; ampl: genes locus amplification; del: gene deletions. TP53 gene is considered mutated when either copy number changes or mutations are present. Adapted from (Vecchio et al., 2015).

GSCs grown in adherence maintain their stemness properties

To better evaluate the effect of the screened drugs on the cellular phenotype, we decided to perform our screening on the two GSC lines grown as adherent cultures.

GSC lines are usually cultured in suspension as neurospheres. Recently, Pollard *et al.* have demonstrated that GSCs can also be efficiently grown as adherent cultures without losing their stemness properties (Pollard et al. 2009). In addition, Rahman and colleagues have shown no statistically meaningful differences between GSCs when grown in both ways (Rahman et al., 2015). Therefore, I optimized the growth of COMI and VIPI lines as adherent cultures using laminin as substrate (**Figure 3.1a**). I also demonstrated that these cells still maintained their stemness properties by analyzing the expression levels of stemness (SOX2 and NESTIN), and differentiation (GFAP, O4 and MAP2) markers by immunofluorescence. Both lines expressed high levels of stemness markers (SOX2 and NESTIN) but low or null levels of astrocytic (GFAP), oligondedrocytic (O4) and neuronal (MAP2) differentiation markers (**Figure 3.1b**).

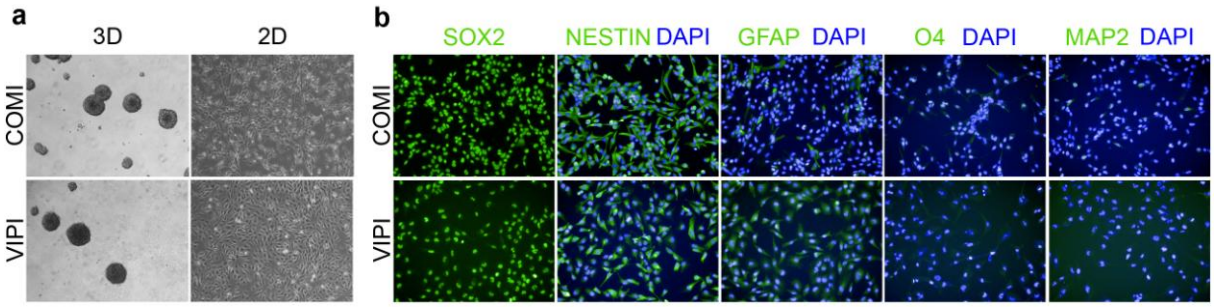

Figure 3.1 GSCs grown as adherent cultures maintain their stemness properties.

a. Two grade IV GBM patient-derived GSC lines, COMI and VIPI, were adapted to grow as adherent cultures on laminin. **b.** COMI and VIPI grown as adherent cultures maintain their stemness properties, as assessed by immunofluorescence using SOX2 and NESTIN as stemness markers and GFAP (astrocytic differentiation), O4 (oligodendrocytic differentiation) and MAP2 (neuronal differentiation) as differentiation markers. Representative immunofluorescence images. n=2 biological replicates.

GSCs rely on OXPHOS respiration for their energy production

To confirm that GSC lines indeed rely on OXPHOS rather than on glycolysis to supply ATP for their energy demand, I treated them with OXPHOS and glycolysis inhibitors for 72h and assessed their viability. As depicted in **Figure 3.2**, all the OXPHOS inhibitors used (rotenone, antimycin A and oligomycin, 1 µM each, as described for rotenone in (Janiszewska et al., 2012)) significantly decreased cellular viability, whereas the glycolysis inhibitors 2-deoxy-D-glucose (2-DG) and sodium dichloroacetate (DCA) did not. This is in line with already published data (Janiszewska et al., 2012; Vlashi et al., 2011).

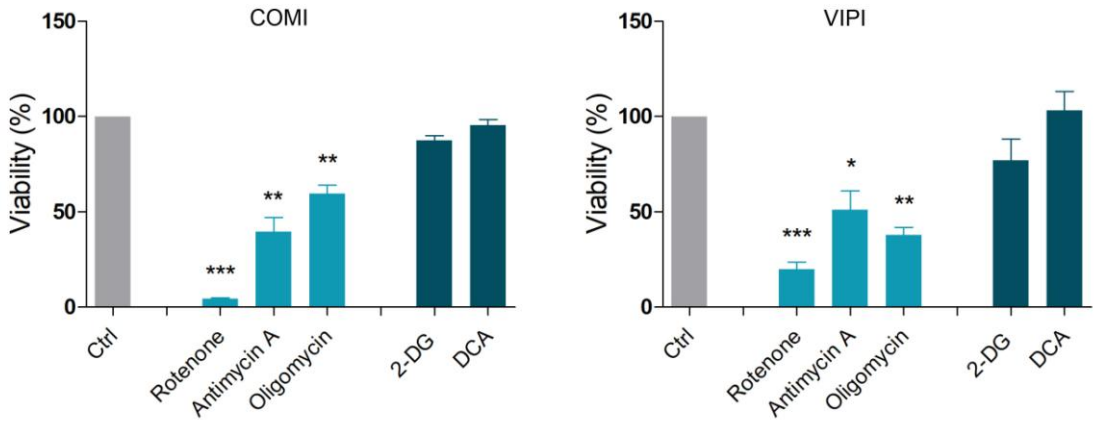

Figure 3.2 GSCs grown as adherent cultures rely on OXPHOS respiration for their energy production. COMI and VIPI cells respond to OXPHOS inhibitors (rotenone, oligomycin and antimycin A, 1 μM each) but not to glycolysis inhibitors (2-deoxy-D-glucose (2-DG) 250 μM and dichloroacetic acid (DCA) 5 mM). Cell viability was assessed by Hoechst 33342 and propidium iodide (PI) 72h after treatment. PI positive cells were subtracted from Hoechst 33342 positive cells, in order to calculate the number of live cells. n=3 biological replicates, mean ± SD. *p < 0.05 **p < 0.01 ***p < 0.001, unpaired two-tailed t test.

3.1.2 A high-content screening identifies the antibiotic classes most effective on GSCs

We reasoned that mitochondrial translation inhibition could be explored to selectively target the GSC compartment, which relies on OXPHOS for energy supply. Based on the bacterial evolutionary origin of mitochondria (Gray, 2012; Gray et al., 1999; Sagan, 1967), on the structural similarity between the bacterial ribosome and the mammalian mitoribosome (Amunts et al., 2015; Greber et al., 2015), as well as on the documented fact that several bacterial ribosome-targeting antibiotics damage human mitochondria in patients (Greber and Ban, 2016; Guan, 2011; Soriano et al., 2005; De Vriese et al., 2006; Zhang et al., 2005), we hypothesized that bacterial ribosome-targeting antibiotics could be exploited to affect the mitoribosome and, hence, OXPHOS complexes assembly and functionality.

By mining the abundant pharmacology of antibiotic drugs acting on bacterial ribosomes (reviewed in Tenson and Mankin 2006; Lambert 2012), I designed a focused custom-made library consisting of 54 molecules (71 molecules including redundant compounds conjugated to different salts or derived from two different companies). The majority of these compounds can be grouped into eight molecular classes of antibiotics known to act *via* inhibition of bacterial ribosomes, among which most are approved by FDA for treating bacterial infections in humans. These classes include the tetracyclines, the streptogramins,

the aminoglycosides, the lincosamides, the macrolides, the amphenicols, the oxazolidinones and the pleuromutilins. The 54-molecule library also included eight compounds which have a known inhibitory effect on the bacterial translation apparatus, but do not belong to a specific molecular class and have been, hence, classified as 'other'. Lastly, I included three additional compounds (rotenone, oligomicyn A, and FCCP) as positive controls. In detail, rotenone acts *via* complex I inhibition, oligomycin A is an ATP synthase inhibitor, and FCCP uncouples the H^+ gradient from ATP synthesis. **Table 3.2** reports all the compounds tested in the high-content screening on GSCs.

Table 3.2 Compounds evaluated in the high-content screening on GSCs

CLASS	COMPOUND	SUPPLIER [a)]
TETRACYCLINES	CHLORTETRACYCLINE HYDROCHLORIDE	MSD, cat. 1500186
	DEMECLOCYCLINE HYDROCHLORIDE	S, cat. S4279
	DEMECLOCYCLINE HYDROCHLORIDE	MSD, cat. 1500226
	DOXYCYCLINE HYDROCHLORIDE	MSD, cat. 1500266
	MECLOCYCLINE SULFOSALICYLATE	MSD, cat. 1501118
	METHACYCLINE HYDROCHLORIDE	S, cat. S2527
	METHACYCLINE HYDROCHLORIDE	MSD, cat. 1501104
	MINOCYCLINE HYDROCHLORIDE	MSD, cat. 1500414
	OXYTETRACYCLINE	MSD, cat. 1500457
	OXYTETRACYCLINE	S, cat. S1773
	OXYTETRACYCLINE DIHYDRATE	S, cat. S2052
	ROLITETRACYCLINE	MSD, cat. 1505684
	TETRACYCLINE HYDROCHLORIDE	S, cat. S2574
	TETRACYCLINE HYDROCHLORIDE	MSD, cat. 1500566
	TIGECYCLINE	S, cat. S1403
LINCOSAMIDES	CLINDAMYCIN HYDROCHLORIDE	MSD, cat. 1500193
	CLINDAMYCIN	S, cat. S2830
	CLINDAMYCIN PALMITATE HYDROCHLORIDE	MSD, cat. 1505470
	LINCOMYCIN HYDROCHLORIDE	S, cat. S2479
	LINCOMYCIN HYDROCHLORIDE	MSD, cat. 1500368
AMPHENICOLS	CHLORAMPHENICOL	MSD, cat. 1500174
	CHLORAMPHENICOL	S, cat. S1677
	CHLORAMPHENICOL HEMISUCCINATE	MSD, cat. 1500173
	CHLORAMPHENICOL PALMITATE	MSD, cat. 1500172
	FLORFENICOL	MSD, cat. 1505978
	THIAMPHENICOL	MSD, cat. 1503136

AMINOGLYCOSIDES	AMIKACIN SULFATE	MSD, cat. 1500111
	APRAMYCIN	MSD, cat. 1505249
	CAPREOMYCIN SULFATE	MSD, cat. 1500157
	DIHYDROSTREPTOMYCIN SULFATE	MSD, cat. 1500249
	GENETICIN	MSD, cat. 1505302
	GENTAMICIN SULFATE	MSD, cat. 1500314
	HYGROMYCIN B	MSD, cat. 1505362
	KANAMYCIN A MONOSULFATE	MSD, cat. 1500360
	KANAMYCIN B SULFATE	MSD, cat. 1500812
	NEOMYCIN SULFATE	MSD, cat. 1500427
	NETILMICIN SULFATE	MSD, cat. 1505482
	RIBOSTAMYCIN SULFATE	MSD, cat. 1503939
	SISOMICIN SULFATE	MSD, cat. 1500536
	SPECTINOMYCIN DIHYDROCHLORIDE	MSD, cat. 1500538
	SPECTINOMYCIN HYDROCHLORIDE	S, cat. S2510
	STREPTOMYCIN SULFATE	MSD, cat. 1500541
	TOBRAMYCIN	MSD, cat. 1500579
MACROLIDES	AZITHROMYCIN	S, cat. S1835
	CLARITHROMYCIN	S, cat. S2555
	DIRITHROMYCIN	MSD, cat. 1504144
	ERYTHROMYCIN	MSD, cat. 1500280
	ERYTHROMYCIN	S, cat. S1635
	ERYTHROMYCIN ESTOLATE	MSD, cat. 1501176
	ERYTHROMYCIN ETHYLSUCCINATE	MSD, cat. 1500279
	NATAMYCIN	MSD, cat. 1505560
	OLEANDOMYCIN PHOSPHATE	MSD, cat. 1500675
	ROXITHROMYCIN	MSD, cat. 1503276
	ROXITHROMYCIN	S, cat. S2506
	TILMICOSIN	MSD, cat. 1505112
	TROLEANDOMYCIN	MSD, cat. 1502203
	TYLOSIN TARTRATE	MSD, cat. 1505312
STREPTOGRAMINS	VIRGINAMYCIN M1	Sigma Aldrich, cat. V2753
	DALFOPRISTIN + QUINUPRISTIN (7:3 w/w)	Santa Cruz Biotech., cat. sc-391726
OXAZOLIDINONES	LINEZOLID	S, cat. S1408
	TEDIZOLID	Santa Cruz Biotech., cat. sc-475055
PLEUROMUTILINS	VALNEMULIN HYDROCHLORIDE	S, cat. S4216
	TIAMULIN	Sigma Aldrich, cat. 34044

OTHER	ACTINONIN	MSD, cat. 210477
	ANISOMYCIN	MSD, cat. 1503906
	AURINTRICARBOXYLIC ACID	MSD, cat. 1505163
	FUSIDIC ACID	MSD, cat. 1500311
	HELVOLIC ACID	Santa Cruz Biotech., cat. sc-396538
	L-1-TOSYLAMIDE-2-PHENYLETHYL CHLOROMETHYL KETONE	Santa Cruz Biotech., cat. sc-201297
	MUPIROCIN	MSD, cat. 1505706
	THIOSTREPTON	Santa Cruz Biotech., cat. sc-sc-203412
POSITIVE CONTROL	FCCP	Cayman Chemical, cat. 15218
	OLIGOMICYN A	Cayman Chemical, cat. 11342
	ROTENONE	MSD, cat. 200013

a) MSD = MicroSource Discovery library; S = Selleck Translation Inhibitors library

I then screened the compound library on the two GSC lines (COMI and VIPI) using a high-content screening approach, which allowed to consider both cytotoxicity and mitotoxicity parameters. The screening was done in technical triplicate, and all the steps were performed in an automated way with the help of the High Throughput Screening (HTS) facility present at CIBIO. The cells were seeded, and 24h later treated with the drugs at a concentration of 100 µM for 24h, and subsequently stained and fixed. As readouts for the screening I used DRAQ5, which allowed to assess morphological features related to cytotoxicity, and the mitochondrial staining MitoTracker Orange (MTO), which accumulates in healthy mitochondria, allowing to observe features related to mitotoxicity. The data were acquired using Operetta High-Content Imaging System and analyzed using the Harmony Software **Figure 3.3a** gives an outline of the screening workflow.

As positive controls for late cellular toxicity deriving from OXPHOS inhibition I utilized rotenone, oligomycin A and FCCP at the same concentration and length of treatment used for the antibiotics being tested (100 µM, 24h). At this concentration and time point all the three OXPHOS inhibitors clearly induced strong cytotoxic effects, causing alteration in cell morphology and cell death. Moreover, since these compounds act by directly inhibiting OXPHOS chain, the effect they induced on cellular toxicity represented the maximum cytotoxic effect I could obtain by hampering the OXPHOS process *via* mitochondrial translation inhibition. Instead, I used FCCP acute administration (100 µM, 30min) as positive control accounting for mitochondrial toxicity. At this concentration and length of treatment, FCCP clearly caused mitochondrial toxicity by altering mitochondrial membrane potential, but did not have any effect on cellular morphology or viability. **Figure 3.3b** reports representative images from the “positive control” treatments.

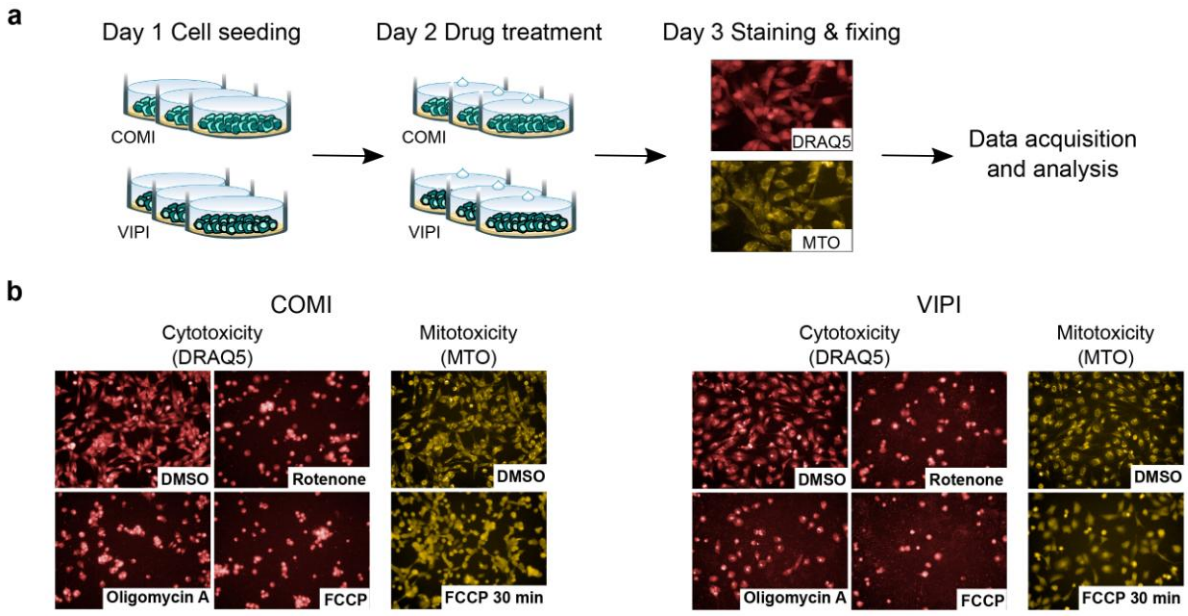

Figure 3.3 Screening workflow and representative images from the positive control treatments used in the screening. a. An outline of the screening workflow. Each treatment was performed in technical triplicate. All screening steps were performed in automated manner, data were acquired using Operetta High-Content Imaging System and analyzed using the Harmony Software. **b.** Example images of control treatments used in the screening. Rotenone, Oligomycin A and FCCP "long treatments" (100μM, 24h) were used as positive controls for cellular totoxicity, whereas FCCP acute administration (100μM, 30min) was used as positive control for mitochondrial toxicity.

In order to evaluate the drug effect on the cells, different morphological features related either to cellular or mitochondrial toxicity were extracted and evaluated. The informative content of a feature was assessed by testing whether the positive controls resulted in statistically significantly different measurements of that specific feature (t-test, FDR < 0.05). Based on this, six morphological features were selected, three of them related to cellular toxicity and three of them related to mitochondrial toxicity. The features were proven to be non-redundant between each other, as depicted in **Figure 3.4a**, which gives the correlation existing between the different features. **Figure 3.4b** shows the behavior of the selected features for the positive control compounds.

In detail, the cellular toxicity was described by the cell number, the nucleus area and the nucleus roundness features, while the mitochondrial toxicity was described by the area of disrupted mitochondria, the number of MTO-selected spots detected in the cytoplasmic regions of cells (mitochondrial spot number), and the area covered by the mitochondrial spot features (mitochondrial spot area). **Table 3.3** describes the selected features.

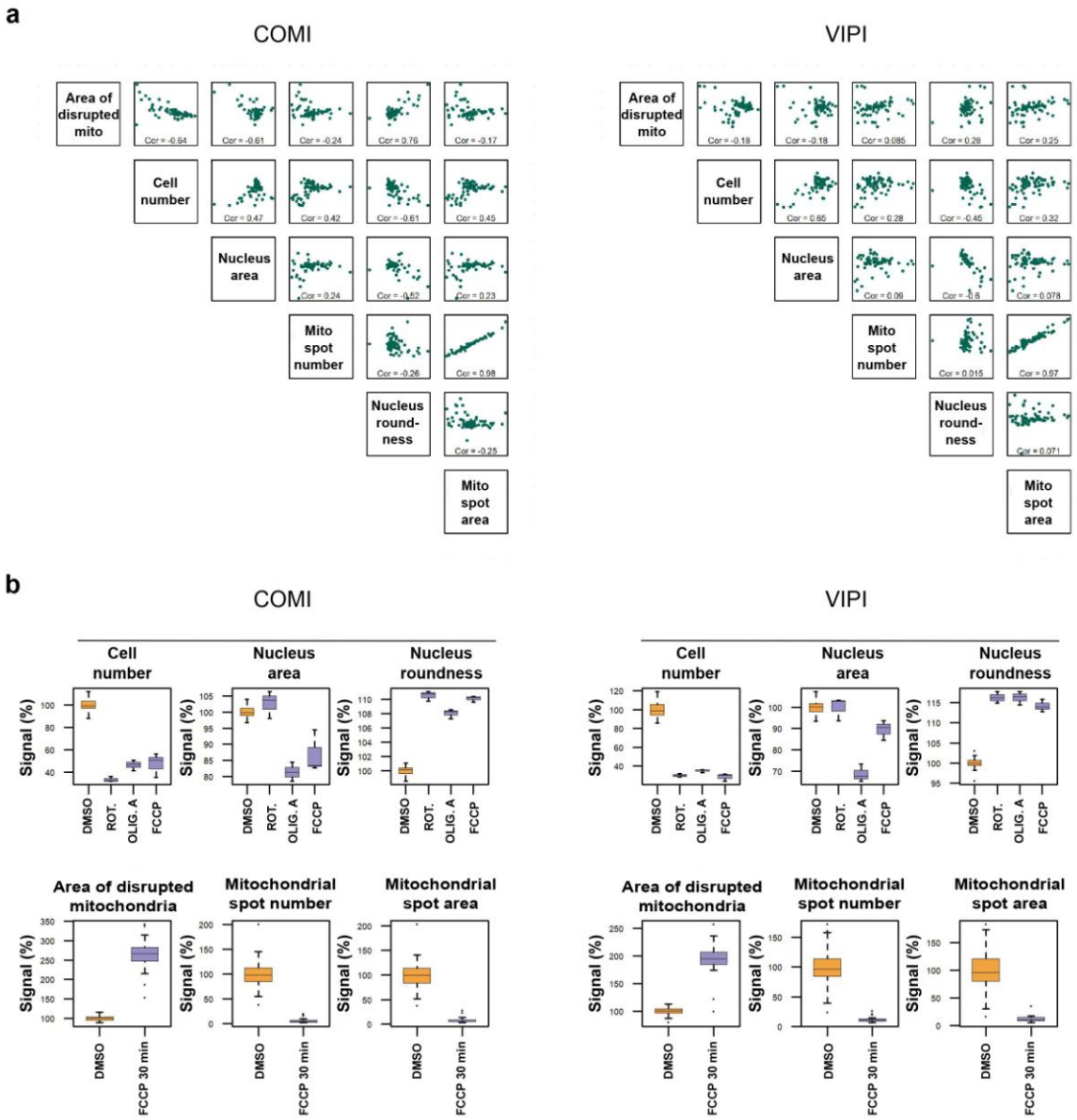

Figure 3.4 Characterization of the features used in the screening analysis.

a. Relationship between features related to cellular and mitochondrial toxicity shown with pairwise Pearson's correlation coefficients. **b.** Behavior of features for positive control compounds. The data were normalized to vehicle treatment (DMSO, yellow) while different positive controls were adopted depending on whether they possessed informative content for cytotoxicity or mitotoxicity (purple).

Table 3.3 Description of the features used in the screening

FEATURE	DESCRIPTION	TOXICITY
Cell number	Total number of DRAQ5-selected nuclei per well. This parameter represents the number of cells per well.	**Cellular**
Nucleus area	Mean area covered by DRAQ5-selected nuclei per well (pixel unit).	**Cellular**
Nucleus roundness	Mean roundness of DRAQ5-selected nuclei per well.	**Cellular**
Area of disrupted mitochondria	Mean per well of the total area covered by > 10 μm^2 regions of MTO dye accumulation identified in each cell (pixel unit). This parameter identifies the area of aggregation of disrupted mitochondria.	**Mitochondrial**
Mitochondrial spot area	Mean per well of the total area of MTO-selected spots detected in the cytoplasmic regions of cells (pixel unit).	**Mitochondrial**
Mitochondrial spot number	Mean per well of the number of MTO-selected spots detected in the cytoplasmic regions of cells.	**Mitochondrial**

With the help of our bioinformatician, I evaluated each compound of the library by assessing the size of the effect it induced on the six selected features. A feature was defined as affected by a given compound when it was found to deviate from the median value of all compounds by a distance larger than 1.5 times the median absolute deviation (**Figure 3.5a**). In order to identify the most effective classes of drugs, each compound was first given an individual score based on the number of features affected and then each class was scored based on the average scores of the compounds it contained (see **Table 3.4**). Three classes, namely streptogramins, pleuromutilins and tetracyclines, presented a class score higher than 25% for at least one of the cell lines tested. Streptogramins presented a class score of 83.33% for COMI and of 66.67% for VIPI, pleuromutilins presented a class score of 50% for both COMI and VIPI, and tetracyclines presented a class score of 28.89% for COMI and of 11.11% for VIPI (**Figure 3.5b**).

In the light of these results, these three most promising classes were chosen for further evaluation.

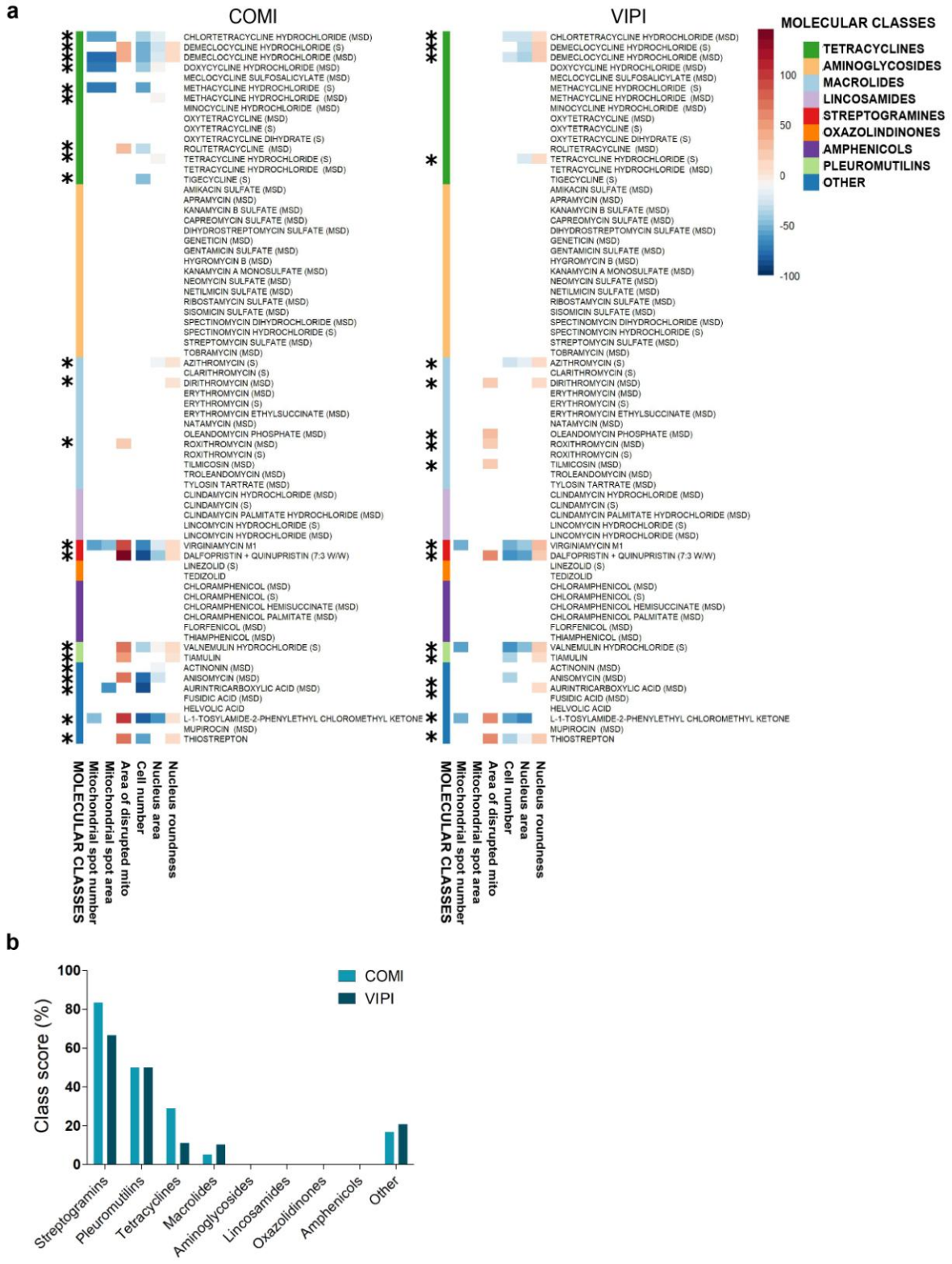

Figure 3.5 Hit identification. a. Hit identification by cytotoxicity-related features (DRAQ5 staining) and mitochondria-related feature (MitoTracker Orange staining) analysis on COMI and VIPI cells. **b.** Class score. Each compound was first given an individual score based on the number of features affected, and then the scores of all compounds in a given class were averaged to obtain the class score. Streptogramins, pleuromutilins and tetracyclines emerged as the most promising classes and were selected for further studies.

Table 3.4 Class score calculation

		COMI			VIPI		
CLASS	**COMPOUND**	**No of positive features**	**Compound Score (%)**	**Total class score (%)**	**No of positive features**	**Compound Score (%)**	**Total class score (%)**
Tetracyclines	Chlorotetracycline HCl (MSD)	4	66.67	**28.89**	3	50	**11.11**
	Demeclocycline HCl (S)	4	66.67		2	33.33	
	Demeclocycline HCl (MSD)	6	100		3	50	
	Doxycycline HCl (MSD)	4	66.67		0	0	
	Meclocycline sulf. (MSD)	0	0		0	0	
	Methacycline HCl (S)	3	50		0	0	
	Methacycline HCl (MSD)	1	16.67		0	0	
	Minocycline HCl (MSD)	0	0		0	0	
	Oxytetracycline (MSD)	0	0		0	0	
	Oxytetracycline (S)	0	0		0	0	
	Oxytetracycline HCl (S)	0	0		0	0	
	Rolitetracycline (MSD)	2	33.33		0	0	
	Tetracycline HCl (S)	1	16.67		2	33.33	
	Tetracycline HCl (MSD)	0	0		0	0	
	Tigecycline (S)	1	16.67		0	0	
Aminoglycosides	All tested compounds	0	0	**0**	0	0	**0**
Macrolides	Azithromycin	2	33.33	**5.13**	3	50	**10.26**
	Clarithromycin (S)	0	0		0	0	
	Dirithromycin (MSD)	1	16.67		2	33.33	
	Erythromycin (MSD)	0	0		0	0	
	Erythromycin (S)	0	0		0	0	
	Erythromycin ethylsuc. (MSD)	0	0		0	0	
	Natamycin (MSD)	0	0		0	0	
	Oleandomycin phosphate (MSD)	0	0		1	16.67	
	Roxithromycin (MSD)	1	16.67		1	16.67	
	Roxithromycin (S)	0	0		0	0	
	Tilmicosin (MSD)	0	0		1	16.67	
	Troleandromycin (MSD)	0	0		0	0	
	Tylosin tartrate (MSD)	0	0		0	0	
Lincosamides	All tested compounds	0	0	**0**	0	0	**0**
Streptogramins	Virginiamycin M1	6	100	**83.33**	4	66.67	**66.67**
	Dalfo+Quinu	4	66.67		4	66.67	
Oxazolidinones	All tested compounds	0	0	**0**	0	0	**0**
Amphenicols	All tested compounds	0	0	**0**	0	0	**0**
Pleuromutilins	Valnemulin HCl (MSD)	4	66.67	**50**	4	66.67	**50**
	Tiamulin	2	33.33		2	33.33	
Other	Actinonin (MSD)	1	16.67	**16.67**	0	0	**20.83**
	Anisomycin (MSD)	3	50		1	16.67	
	Aurintricarboxylic acid (MSD)	2	33.33		1	16.67	
	Fusidic acid (MSD)	0	0		0	0	
	Helvolic acid	0	0		0	0	
	TPCK	1	16.67		4	66.67	
	Mupirocin (MSD)	0	0		0	0	
	Thiostrepton	1	16.67		4	66.67	

3.1.3 Hit classes validation: streptogramins are selected

In a further step to validate the previous results, I bought other commercially available compounds belonging to the three hit classes and evaluated their effect on cellular growth. In detail, I bought 7 compounds belonging to the streptogramin class, 9 belonging to the tetracycline class and 2 belonging to the pleuromutilin class.

Streptogramins are a class of antibiotics consisting of a mixture of two structurally different compounds: the group A (or M) streptogramins, which are polyunsaturated macrolactones, and the group B (or S) streptogramins, which are cyclic hexadepsipeptides (Barrière et al., 1998). Group A and B streptogramins are usually produced by the same *Streptomyces* strain, in a fixed 70:30 (w/w) ratio (Bonfiglio and Furneri, 2001). Streptogramin A and B are known to act synergistically in bacteria (Di Giambattista et al., 1989), and therefore are usually used in combination in a fixed 70:30 (w/w) ratio. While streptogramins are used as combination of two chemically different compounds, tetracyclines and pleuromutilins are used in therapy as single agents.

According to this use, I tested tetracyclines and pleuromutilins as single agents, whereas I assayed streptogramins both as single agents and as combination of group A and B compounds in a 70:30 (w/w) ratio. I treated COMI and VIPI cells with a range of drug concentrations (0.1, 0.3, 1, 3, 10, 30 and 100 μM) for 48h, and then I assessed the cellular viability using Hoechst 33342 and propidium iodide (PI) staining. Hoechst 33342 and PI are both DNA dyes but, while Hoechst 33342 is capable to penetrate both live and dead cells, PI enters only the cells with a compromised cytoplasmic membrane, i.e. dead cells. By subtracting PI positive cells from Hoechst 33342 positive cells, it is possible to count the number of living cells. I normalized the data obtained for each concentration tested on the number of cells present in the control (DMSO-treated cells) and then, by plotting the data using GraphPad Prism software, I constructed dose-response curves for each compound (**Figure 3.6**). In general, VIPI cells were more resistant to treatments than COMI cells. Moreover, the compounds belonging to the three classes had different behaviors. While the majority of compounds belonging to the streptogramin and the tetracycline classes were able to affect cellular growth in a dose-dependent manner for both cell lines, the pleuromutilins (valnemulin and tiamulin) had a minimal effect on cellular growth. Valnemulin affected cellular growth only at the highest dose tested (100 μM), and tiamulin did not affect it at all.

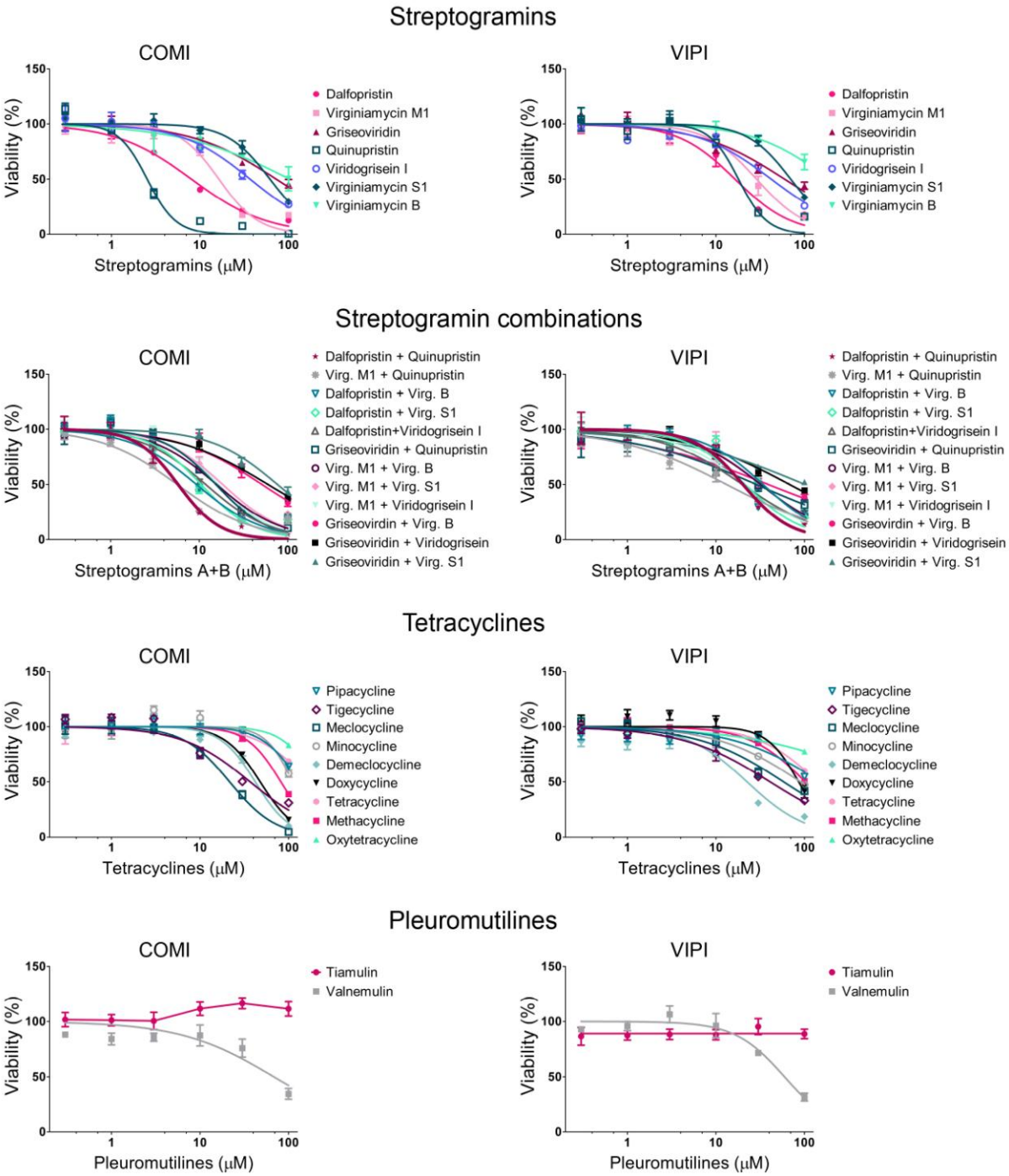

Figure 3.6 Hit classes validation and selection: dose-response curves. Representative curves are shown for all compounds tested for streptogramins (tested both as single agents and as group A and B combinations), tetracyclines and pleuromutilins. The cells were treated with compounds for 48h, after which they were stained with Hoechst 33342 and PI, and the number of live cells was evaluated using Operetta-High Content Imaging System and Harmony software. Dose-response curves were plotted using GraphPad Prism software.

In order to better compare the potency of the tested drugs, I calculated for each compound the growth inhibition 50 (GI_{50}) value deriving from the dose-response curves. The GI_{50} value is defined as the compound concentration causing the 50% inhibition of the cellular growth, and is, therefore, a parameter to evaluate a compound cytotoxicity. Compounds with the lowest GI_{50} values are the most potent in reducing or inhibiting cellular growth and are, therefore, the most interesting. **Figure 3.7** shows the GI_{50} values for all the tested compounds, which are grouped according to the class they belong to.

I set an arbitrary threshold at GI_{50} value equal to 50 µM and focused on the compounds having GI_{50} values lower than the fixed threshold for both cell lines.

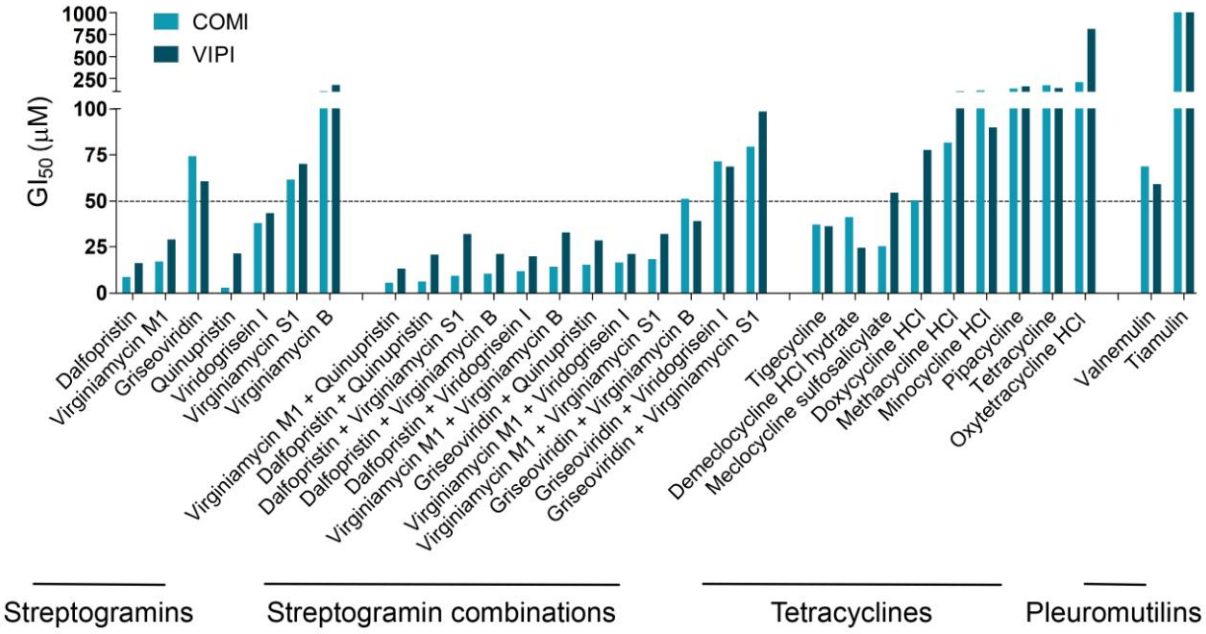

Figure 3.7 Hit classes validation and selection: GI_{50} values. The GI_{50} values calculated from the dose-response curves constructed for all the tested compounds, which are divided according to the class they belong to. Streptogramins were tested both as single agents and as combinations of group A and B compounds in a 70:30 (w/w) ratio.

The streptogramin class, both as single agents and as combinations of group A and B compounds, presented the highest number of compounds/combinations with GI_{50} values lower than 50 µM. The chemical structures of the streptogramins tested are given in **Figure 3.8**.

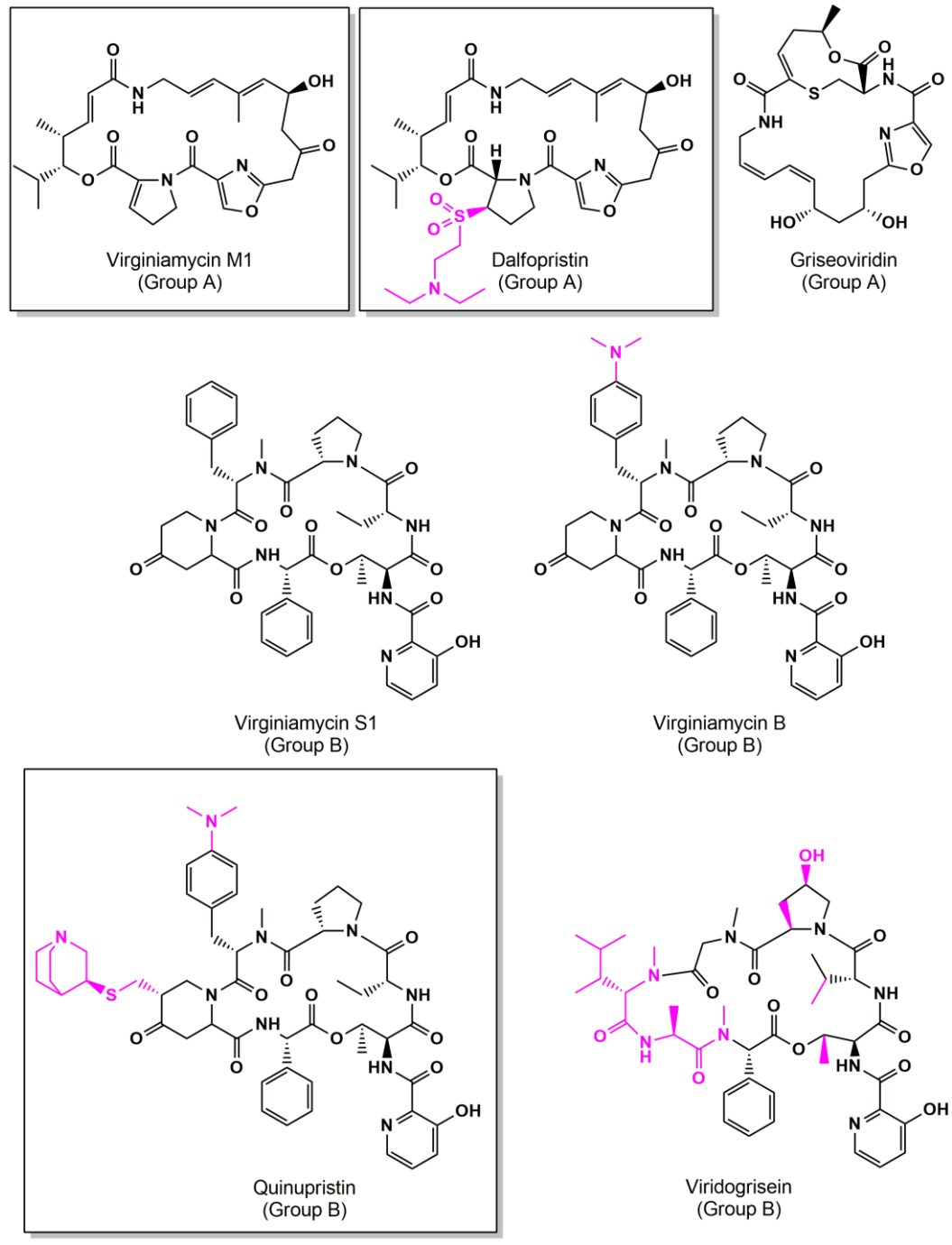

Figure 3.8 Chemical structures of the streptogramins tested. Streptogramins consist of a mixture of two structurally different compounds: the group A (or M) streptogramins, which are polyunsaturated macrolactones, and the group B (or S) streptogramins, which are cyclic hexadepsipeptides. Virginiamycin M1, dalfopristin and griseoviridin belong to group A, whereas virginiamycin S1, virginiamycin B, quinupristin and viridogrisein belong to group B. The core scaffold is presented in black, whereas the chemical substituents specific for the different compounds are highlighted in pink. Dalfopristin and virginiamycin M1 emerged as the most potent compounds among group A, whereas quinupristin emerged as the most potent compounds among group B.

Dalfopristin and virginiamycin M1, which share a very similar chemical scaffold, emerged as the most potent compounds among group A streptogramins. Griseoviridin, which belong to group A but presents a chemical scaffold totally different to that of dalfopristin and virginiamycin M1, showed less activity, with GI_{50} values of 74.1 μM for COMI and of 60.7 μM for VIPI. These data clearly indicated that the chemical scaffold shared by dalfopristin and virginiamycin M1 inhibit GSC proliferation more effectively than that of griseoviridin. Among group B streptogramins, quinupristin emerged as the most potent. Notably, virginiamycin S1 and virginiamycin B, which differ from quinupristin for few small substituent groups, were much less potent than quinupristin.

In general, streptogramins used as combinations of group A and B compounds were more potent than streptogramins used as single agents. Only the combinations between griseoviridin and the members of the group B streptogramins, with the exception of quinupristin, had GI_{50} values higher than 50 μM, proving again that the scaffold shared by dalfopristin and virginiamycin M1 is more prosing. Among all, the combinations between quinupristin/virginiamycin M1 (Q/VM1) and quinupristin/dalfopristin (Q/D) (70:30 w/w) emerged as the most potent in inhibiting GSCs growth.

No compounds belonging to the pleuromutilin class had GI_{50} values lower than 50 μM.

Among all the tetracyclines tested, only two compounds, namely tigecycline and demeclocycline, had a GI_{50} value lower than 50 μM for both cell lines. An additional compound, meclocycline, had a GI_{50} value of 25.3 μM for COMI and of 54.5 μM for VIPI. The chemical structures of the tetracycline compounds tested are presented in **Figure 3.9**.

Compared to the basic “tetracycline” chemical scaffold, demeclocycline, tigecycline and also meclocycline present a substituent group in position 7. Both demeclocycline and meclocycline present an electron-withdrawing group (fluorine atom) in this position. Considering that both molecules presenting a fluorine atom in position 7 emerged among the three most potent tetracyclines, the presence of this substituent could be important for the biological activity of this class. Tigecycline is substituted in position 7 with an electron-donating group (dimethylamino group). The importance of this group for the biological activity is not clear given that minocycline, which also presents a dimethylamino group in position 7, had GI_{50} values around 100 μM for both COMI and VIPI cells. In position 9, tigecycline presents a *tert*-butyl-glycylamido side chain, which has been reported to increase the antibacterial activity of the compound (Jenner et al., 2013) and, therefore, could also play a crucial role in mitoribosome binding and GSC growth inhibition.

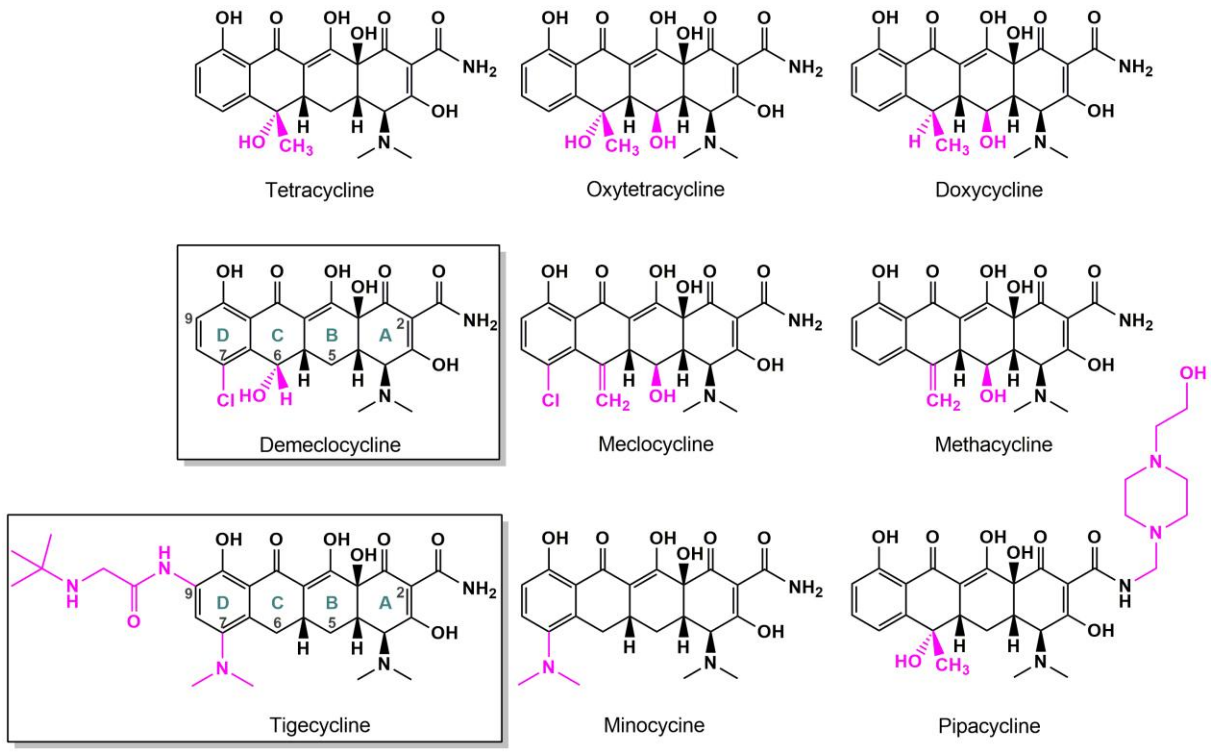

Figure 3.9 Chemical structures of the tetracycline compounds tested. The basic tetracycline structure consists of four six-membered rings (A, B, C and D) fused together to form a octahydro napthacene. The core scaffold is substituted with several hydroxyl and carbonyl groups. The core scaffold is presented in black, whereas the chemical substituents specific for the different compounds are highlighted in pink. Demeclocycline and tigecycline emerged as the most potent compounds among all the tetracycline compounds tested.

In summary, among all the bacterial ribosome-targeting antibiotic classes, streptogramins used as combination of group A and B compounds were identified as the most effective in inhibiting GSC growth based on the GI_{50} values. In detail, the combinations quinupristin/virginiamycin M1 (Q/VM1) and quinupristin/dalfopristin (Q/D) (70:30 w/w) were selected for further investigation.

3.2 QUINUPRISTIN/DALFOPRISTIN (Q/D) AS LEAD COMPOUND

3.2.1 Q/D is the most cytotoxic among the streptogramins and is selected as lead compound

As previously described, virginiamycin M1 and dalfopristin (**Figure 3.8**) share a common chemical scaffold and are structurally very similar. Interestingly, dalfopristin is a virginiamycin M1 semi-synthetic derivative, which is known to hydrolyze very rapidly to virginiamycin M1 at pH 7.4 and 37°C (half-life of 11 min; Noeske et al. 2014). Therefore, it is not surprising that

dalfopristin and virginiamycin M1 and their respective combinations with quinupristin (Q/D and Q/VM1) have similar activities.

Notably, the Q/D (30:70 w/w) combination has been approved as an antibiotic by FDA in 1999 with the name of Synercid® for treating infections caused by susceptible strains of vancomycin-resistant *Enterococcus faecium* (VREF) and for treating complicated skin and skin structure infections caused by *Staphylococcus aureus* (methicillin-susceptible) or *Streptococcus pyogenes* (Gurk-Turner, 2000). Based on its promising GI_{50} value and on the already existing FDA approval as antibiotic, the Q/D combination was selected as lead compound. The chemical structure of the Q/D combination is represented in **Figure 3.10**.

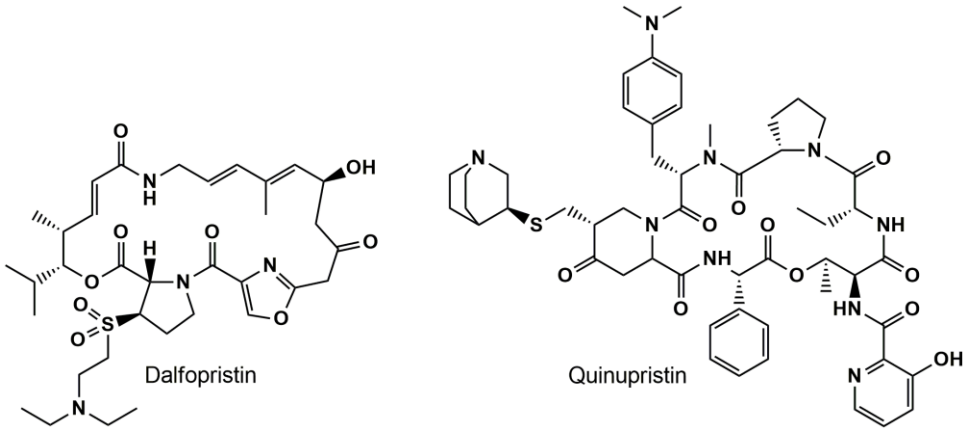

Figure 3.10 Chemical structure of the Q/D combination selected as lead compound. Q/D is composed of quinupristin, group B streptogramins, and dalfopristin, group A streptogramins, in 30:70 w/w ratio.

3.2.2 Q/D has a universal activity on GSC lines

Subsequently, I evaluated the cytotoxicity of Q/D on a larger panel of GSCs. The panel was composed of COMI and VIPI and of other six GSC lines, namely 030616, GB6, GB7, GB8, G144 and G166. 030616 line was a kind gift from Rossella Galli (San Raffaele Hospital, Milan, Italy), whereas the other five GSC lines were a kind gift from Prof. Luciano Conti (CIBIO, University of Trento, Italy). All the GSC lines derive from patients who were diagnosed with GBM and were characterized as GSCs (Alessandrini et al., 2015; Conti et al., 2012; Pollard et al., 2009; Vecchio et al., 2014, 2015). I treated the eight GSC lines, which were grown as adherent cultures on laminin, with a range of Q/D concentrations for 48h and then I assessed the cellular viability using Hoechst 33342 and PI staining. Next, I constructed dose-response curves and calculated the deriving growth inhibition 50 (GI_{50}) values, which ranged from 4.2 to 24 μM for all the lines tested, confirming the inhibitory effect of Q/D on GSCs growth (**Figure 3.11**). In detail, GI_{50} values for COMI and VIPI were of 6.5 μM ±1.1 and 20.2 μM ±1.4, respectively.

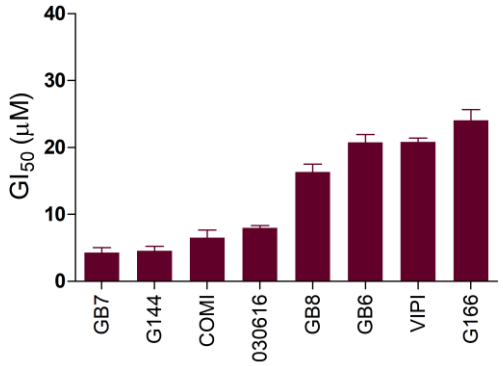

Figure 3.11 Q/D effect on a panel of eight GSC lines. GI_{50} values of Q/D on a panel of 8 GSCs (indicated on the x-axis). The cells were treated with several concentrations of Q/D (0.1, 0.3, 1, 3, 10, 30 and 100 µM) for 48h, after which they were stained with Hoechst 33342 and PI, and the number of living cells was evaluated using Operetta-High Content Imaging System and Harmony software. The GI_{50} values were calculated from n=3 biological replicates (n=4 technical replicates each), mean ± SD.

Similar results were obtained by our collaborators in the laboratory of Dr. Lucia Ricci-Vitiani at the Istituto Superiore di Sanità in Rome, who tested Q/D on a panel of GSC lines derived from 18 patients (three cell lines were isolated from different areas of the tumor in three patients). **Table 3.5** reports information on the clinical data of the patients and on the molecular characterization of the derived cell lines.

Table 3.5 Patient clinical data and GSC line molecular characterization

GSC LINE	DATE	AGE (years)	SEX	OS (mos)	PFS (mos)	MGMT	EGFR vIII	PTEN	VEGF	Ki67 (%)
1	02/12/2003	40	M	12,5	6	M	Neg	Normal	Iper	20
23	24/05/2004	77	M	2	1	UM	Neg	Normal	Iper	50
28	12/07/2004	72	M	11,5	6	M	Neg	Ipo	Iper	5
30	02/08/2004	44	M	7,5	5	M	Pos	Normal	Iper	10
61	19/04/2005	59	M	6	3	UM	Pos	Normal	Normal	35
62	05/05/2005	64	M	14	10	M	Neg	Normal	Iper	10
67	06/06/2005	48	M	2	1	UM	Neg	Ipo	Iper	20
68	07/06/2005	58	M	10,5	4	UM	Neg	Normal	Normal	10
70	14/07/2005	67	F	9	6	UM	Pos	Ipo	Iper	20
74	18/08/2005	70	F	8	2	UM	Pos	Normal	Iper	15
76	25/08/2005	48	F	16	11	UM	Neg	NA	Iper	15
83	21/11/2005	52	M	8	3	UM	Pos	Normal	Iper	40
112	08/01/2007	49	F	6	3	M	Pos	Ipo	Iper	18
120	01/03/2007	53	M	16,5	8	UM	Neg	Normal	Iper	30
147	21/02/2008	69	F	11	7	UM	Neg	Normal	Iper	25
148	25/02/2008	55	M	8	5	UM	Neg	Normal	Iper	70
151	04/04/2008	69	M	72	60	M	Neg	Ipo	Iper	30
163	05/01/2009	56	M	2	1	UM	Neg	Ipo	Normal	15

The 21 GSC lines derived from the 18 patients were grown in suspension as neurospheres and treated with Q/D for 48 and 72h. The GI_{50} values derived ranged from 2.5 to 32.5 μM after 48h of treatment and from 1.7 to 12.2 μM after 72h of treatment (**Figure 3.12**), in line with the values that I obtained.

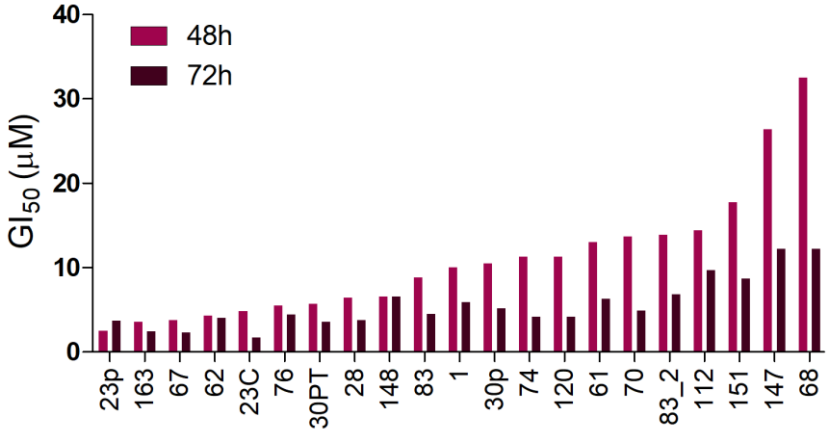

Figure 3.12 Q/D has a universal activity on GSC lines. The GSCs wide sensitivity to Q/D was tested by calculating the GI_{50} values on a panel of 21 GSC lines (indicated on the x-axis) derived from 18 tumor samples at 48 and 72h post-Q/D treatment using CellTiter-Glo Assay, n=4, technical replicates.

With the help of our bioinformatician, I tried to correlate the GI_{50} values determined at the two different time points with the clinical and molecular data available. However, no correlation resulted to be significant (p-value > 0.05) as reported in **Table 3.6**.

Table 3.6 Correlation between GI_{50} values and clinical and molecular data

	AGE (years)	**SEX**	**OS** (mos)	**PFS** (mos)	**MGMT**	**EGFR vIII**	**PTEN**	**VEGF**	**Ki67** (%)
GI_{50} (48h)	0.58	0.31	0.29	0.39	0.73	0.87	0.59	0.22	0.54
GI_{50} (72h)	0.72	0.28	0.26	0.30	0.79	0.90	0.58	0.48	0.90

In a parallel experiment, I also confirmed the cytotoxic effect of Q/D on GSCs grown as neurospheres. I seeded 10 COMI cells per well in media containing various Q/D concentrations and measured the growth of neurospheres over the course of nine days (**Figure 3.13a**). By measuring the area of the sphere, I observed that 1 μM Q/D treatment slightly inhibited neurosphere growth while 5 and 10 μM treatment nearly completely abolished its formation (**Figure 3.13b**).

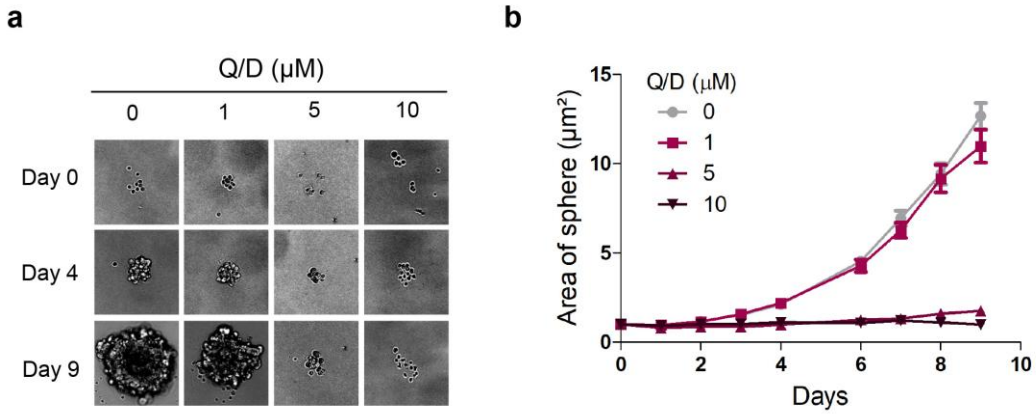

Figure 3.13 Q/D affects GSC sphere growth. a-b. Effects of Q/D treatment on GSCs grown in suspension. Ten COMI cells were seeded in each well and treated with Q/D (1, 5 and 10 μM). Cell growth was monitored over the course of nine days. **a.** Example images from days 0, 4 and 9. **b.** Sphere area quantification over the course of nine days. Data was collected using Operetta-High Content Imaging System and analyzed using Harmony Software. n=30 technical replicates, mean ± SEM. One representative experiment is shown, n=3 biological replicates.

3.2.3 Q/D combination is selectively cytotoxic for GSCs compared to normal cells, is more potent than TMZ on GSCs, and decreases GSCs neurosphere forming ability

A good anticancer drug should be able to discriminate between normal and cancer cells and specifically target the latter.

I evaluated the selectivity of Q/D for GSCs by assessing its effect in inhibiting the growth of normal astrocytes derived by differentiation from human neural fetal stem cells (CB660) and of normal lung fibroblasts (MRC5). I treated CB660 and MRC5 cells with different concentration of Q/D for 48h and assessed the cellular viability using Hoechst 33342 and PI staining. Next, I constructed dose-response curves and calculated the deriving growth inhibition 50 (GI_{50}) values, which were of 68.3 μM ±15.5 and 72.7 μM ±15.7 for CB660 and MRC5, respectively. **Figure 3.14a** shows the GI_{50} values for CB660 and MRC5 cells (in purple) compared to those for the 8 GSC lines (in gray) reported in **Figure 3.11**. Considering that the GI_{50} values of the GSC lines tested ranged from 4.2 to 24 μM, Q/D proved to be 3 to 16 times more selective for GSC lines compared to normal cell lines, showing a discrete therapeutic window.

GSCs are characterized by self-renewal capabilities (Galli et al., 2004; Singh et al., 2004; Yuan et al., 2004). Since Q/D inhibits GSCs growth, I wondered whether it could impact on GSCs self-renewal and maintenance. Therefore, I investigated the functional effects of Q/D on GSCs, by examining the neurosphere forming ability upon Q/D treatment. I treated COMI cells grown in suspension with various concentrations of Q/D for 72h and subsequently dissociated them and seeded 10 or 100 cells per well. After 10 days, I evaluated neurosphere formation, considering and counting the neurospheres with a diameter bigger than 100 µm (**Figure 3.14b**). Q/D decreased the neurosphere forming ability of COMI cells in a dose-dependent manner, implicating its substantial impact on GSCs maintenance.

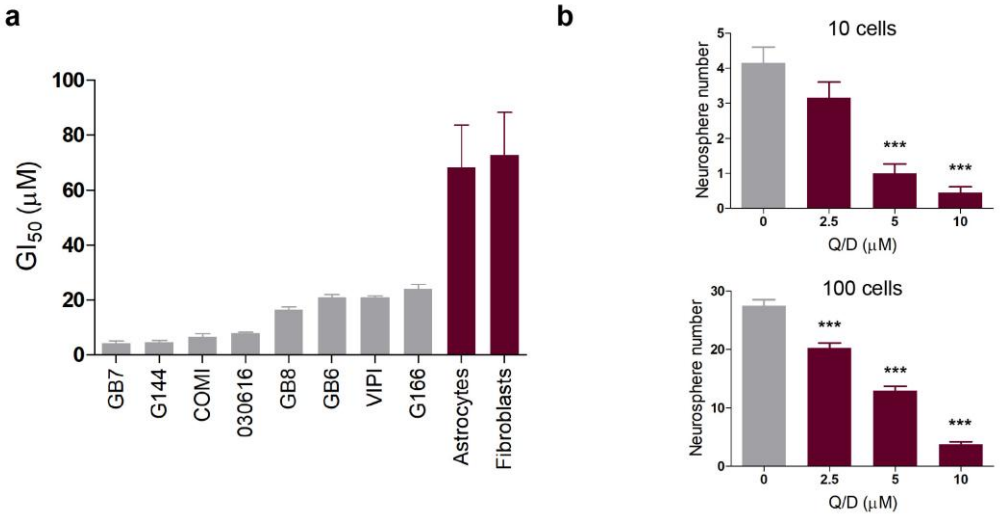

Figure 3.14 Q/D is selectively cytotoxic for GSCs and decreases GSC neurosphere forming ability. a. GI_{50} values of Q/D on 8 GSC lines compared to GI_{50} values of Q/D on astrocytes derived from human fetal neural stem cells (CB660) and on human lung fibroblasts (MRC5). The cells were treated with Q/D (0.1, 0.3, 1, 3, 10, 30 and 100 µM) for 48h, after which they were stained with Hoechst 33342 and PI, and the number of live cells was evaluated using Operetta-High Content Imaging System and Harmony software. The GI_{50} values were calculated from n=3 (biological replicates, n=4 technical replicates each), mean ± SD. **b.** Neurosphere formation assay. COMI grown in suspension were pre-treated with different concentration (2.5, 5 and 10 µM) of Q/D for 72h, after which the spheres were dissociated and 10 or 100 cells/well were plated in 96 well plate. The number of spheres greater than 100 µm was quantified after 10 days. n=20 technical replicates, mean ± SEM. ***p < 0.001, unpaired two-tailed t test. One representative result is shown, n=3 biological replicates.

GSCs are known to be resistant to TMZ (Chen et al., 2012). I compared the cytotoxic effect of the Q/D combination to that of TMZ on two different GSC lines. I treated COMI and VIPI cells with various concentrations of either Q/D or TMZ, constructed dose-response curves and calculated the deriving GI_{50} values. Q/D combination proved to be at least 14 times more potent than TMZ for GSCs. In fact, Q/D had GI_{50} values of 6.5 µM ±1.1 and 20.2 µM ±1.4 for COMI and VIPI, respectively, whereas TMZ GI_{50} values were of 96.5 µM ±15.2 for COMI and of 337.7 µM ±35.5 for VIPI (**Figure 3.15**). Notably, VIPI were 3 times more resistant than COMI to both Q/D and TMZ treatments. Unfortunately, no data on the methylation status of the MGMT gene, which could explain the different sensitivity to TMZ, are available for COMI and VIPI lines. According to the molecular characterization of COMI and VIPI performed by Vecchio and colleagues (**Table 3.1**, (Vecchio et al., 2015)), VIPI line presents a mutated form of TP53 gene, which could contribute to its more drug-resistant phenotype.

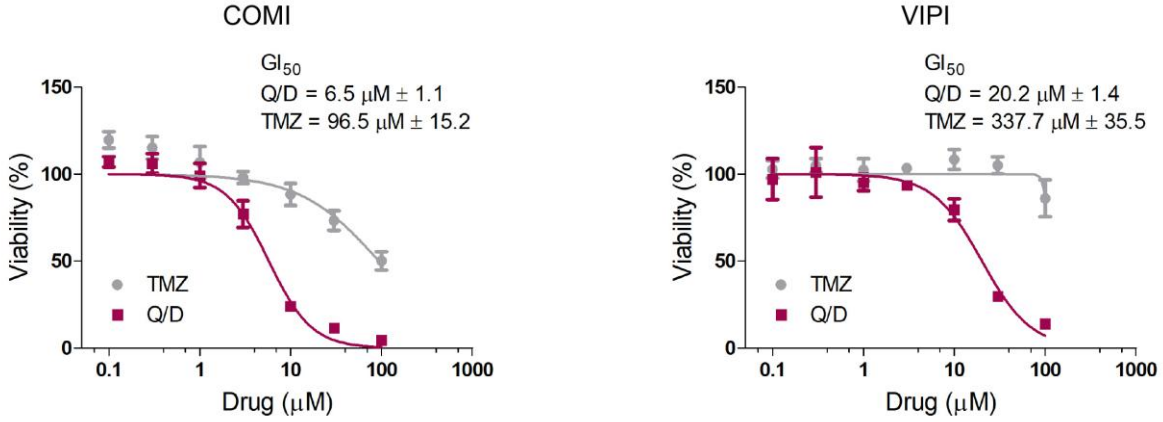

Figure 3.15 Q/D is more potent than TMZ on GSCs. Representative dose-response curves for Q/D and temozolomide (TMZ) on COMI and VIPI cells. The cells were treated with Q/D or TMZ (0.1, 0.3, 1, 3, 10, 30 and 100 µM) for 48h, after which they were stained with Hoechst 33342 and PI, and the number of live cells was evaluated using Operetta-High Content Imaging System and Harmony software. The GI_{50} values were calculated from n=3 biological replicates, n=4 technical replicates each, mean ± SD.

3.3 Q/D INHIBITS MITOCHONDRIAL TRANSLATION, LEADING TO OXPHOS IMPAIRMENT

3.3.1 Q/D inhibits mitochondrial translation in GSCs leading to OXPHOS dysregulation and impairment

As an antibiotic Q/D combination exerts its bactericidal activity by inhibiting the bacterial ribosome, thus preventing protein synthesis. Following our initial working hypothesis grounded on the evolutionary similarity between bacterial and mitochondrial ribosomes, we reasoned that a bacterial ribosome-targeting antibiotic could exert inhibitory effects also on mitoribosomes. I, therefore, started to investigate the effect of Q/D on mitochondrial translation and mitochondrial metabolism.

^{35}S-methionine metabolic labeling allows to detect nascent proteins, which are being actively translated by either the cytosolic or the mitochondrial translation system. If the translation apparatus is inhibited, a decrease or absence of newly synthesized proteins is observed. To perform ^{35}S-methionine metabolic labeling experiments, I moved to Dr. Joanna Rorbach's lab, at the Karolinska Institute, where I investigated Q/D effect on both mitochondrial and cytosolic nascent proteins. Q/D was very effective in inhibiting mitochondrial translation and nearly completely abolished it at 0.5 μM concentration in COMI cells treated for 24h. Importantly, no effects on cytosolic translation were noted at this or even at 5 fold higher Q/D concentrations (up to 2.6 μM tested, **Figure 3.16a**).

I further confirmed Q/D effects on mitochondrial and cytosolic translation by performing immunofluorescence and immunoblotting on COMI and VIPI cells treated for 48h (**Figure 3.16b,c**). In detail, I studied the expression levels of cytochrome *c* oxidase subunit 1 (COX1) and cytochrome *c* oxidase subunit 4 (COX4), two proteins belonging to complex IV of the electron transport chain (ETC). COX1 is mitochondrially encoded and translated by the mitochondrial translation system, whereas COX4 is nuclearly encoded and translated by the cytosolic translation system. If Q/D acts by inhibiting selectively mitochondrial translation, a selective decrease in COX1 expression levels, but not in those of COX4, should be observed. Upon treatment with Q/D, the expression of COX1 was markedly decreased, whereas the expression of COX4 remained unchanged (**Figure 3.16b,c**), confirming selective mitochondrial translation inhibition.

A decrease in mitochondrially translated proteins could also be due to a decrease in the levels of mRNAs coding for those proteins. On the other hand, inhibition of translation could also lead to a compensatory upregulation of mRNA levels coding for those proteins whose translation is blocked. To clarify this point, I assessed Q/D effects on the levels of mRNAs

coding for COX1 and COX4. Upon treatment with a range of Q/D concentrations, I did not observe any significant changes in mRNAs levels (**Figure 3.16d**). Taken together, these results prove that mitochondrial translation is the primary target of the Q/D combination.

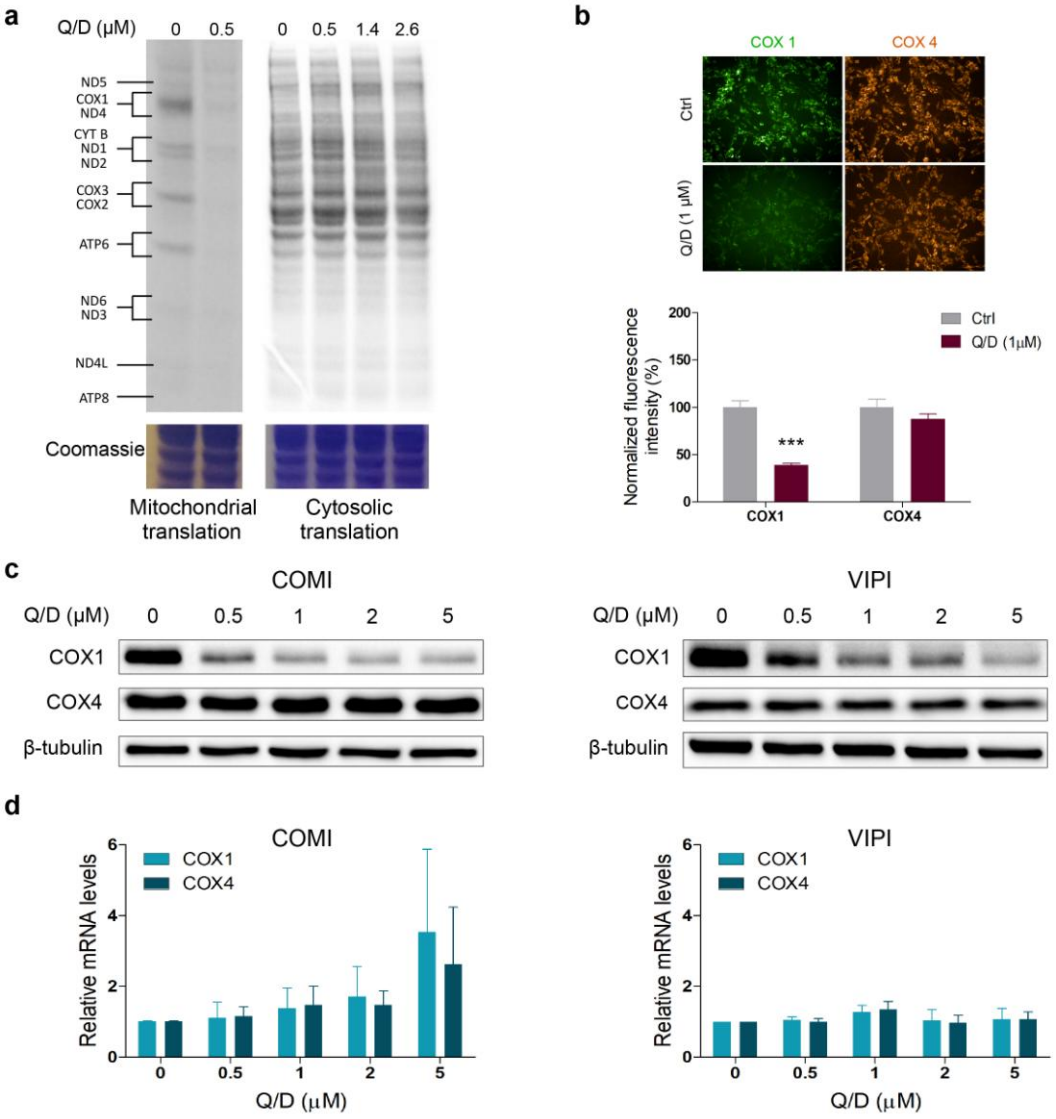

Figure 3.16 Q/D inhibits mitochondrial translation in GSCs. a. ^{35}S metabolic labeling assay on mitochondrial (left) and cytosolic (right) translation on COMI cells after 24h treatment with Q/D (0.5 μM for mitochondrial translation and 0.5, 1.4 and 2.6 μM for cytosolic translation). Emetine was used to inhibit cytosolic translation when assessing for mitochondrial translation inhibition. One representative result is shown, n=3 biological replicates. **b.** Effects of Q/D (1 μM) on COX1, COX4 proteins as assayed by immunofluorescence on COMI cells after 72h treatment. *Top.* Representative images. *Bottom.* Fluorescence intensity quantification. One representative result is shown, n=3 biological replicates. **c.** Effects of increasing concentrations of Q/D (0.5, 1, 2 and 5 μM) on COX1, COX4 and beta tubulin proteins as assayed by immunoblotting on COMI and VIPI cells after 48h treatment. One representative result is shown, n=2 biological replicates. **d.** Effects of increasing concentrations of Q/D (0.5, 1, 2 and 5 μM) on COX1 and COX4 mRNA levels as assayed by RT-qPCR on COMI and VIPI cells after 48h treatment. Data presented as fold change over control. n=4-5 biological replicates, mean ± SD. Unpaired two-tailed t test.

The 13 polypeptides synthesized by the mitoribosomes are coordinately assembled with the cytosolic-translated polypeptides to correctly form the OXPHOS complexes (Couvillion et al., 2016; Richter-Dennerlein et al., 2016). The 13 mitochondrially translated proteins are essential for functional OXPHOS complexes. By performing blue native polyacrylamide gel electrophoresis (BN-PAGE) followed by in-gel activity assays on COMI and VIPI cells, I investigated Q/D effects on OXPHOS complexes functionality. The activity of complex I, IV and V, which are formed by both mitochondrially and cytosolically translated proteins, was decreased upon Q/D treatment, whereas the activity of complex II, which is composed entirely of nuclearly encoded proteins, was unaffected (**Figure 3.17a**). In particular, when performing in-gel activity on complex V I observed the emergence of two new bands in the treated samples, with a lower size compared to that observed in the untreated cells. In line with Nijtmans and colleagues, the band with the highest molecular weight can be attributed to a full F_1F_0 ATP synthase, whereas the lower bands can be assigned to a non-full ATP synthase intermediate form, composed of the F_1 domain plus several polypeptides belonging to the F_0 domain, and to the F_1 domain, respectively (Nijtmans et al. 1995, **Figure 3.17a**). Upon mitochondrial translation inhibition the ATP synthase intermediate form and the F_1 domain, which are composed of only cytosolically translated proteins, can still be assembled, whereas assembly of the complete complex is impaired, leading to decreased steady-state levels of F_1F_0 ATP synthase (Nijtmans et al., 1995).

In parallel, I assessed the complexes protein levels using BN-PAGE followed by immunoblotting and confirmed that protein levels of complex I, IV and V were decreased by Q/D treatment, but not those of complex II (**Figure 3.17b**). Also in this case, it was possible to detect protein bands for the ATP synthase intermediate form and for the F_1 domain, when incubating with the antibody directed to complex V (Ab anti-ATP5A).

Dysfunctional complexes should lead, in consequence, to a decreased mitochondrial respiratory capacity. Using high-resolution respirometry, the oxygen consumption and the mitochondrial respiratory capacity of COMI and VIPI cells treated with Q/D were measured. For both cell lines, 1 μM Q/D treatment caused a decreased in oxygen consumption by complex I, and complex I and II and a loss in the reserve respiratory capacity, detected as a decrease in the maximal oxygen consumption after injection of the mitochondrial uncoupler FCCP. Complex II oxygen consumption was, instead, not significantly altered by Q/D treatment (**Figure 3.17c**). Overall, these results demonstrate that Q/D treatment has detrimental effects on the functionality of the OXPHOS chain.

A defective mitochondrial oxidative phosphorylation could lead cells to metabolically switch toward glycolysis for ATP supply. I investigated the effect of Q/D treatment on the cellular glycolytic metabolism, by measuring the levels of L-lactate, which is the final product of the

glycolytic pathway. Upon Q/D treatment, I observed a small but significant increase in the L-lactate production starting from 1 µM for both COMI and VIPI cells (**Figure 3.17d**).

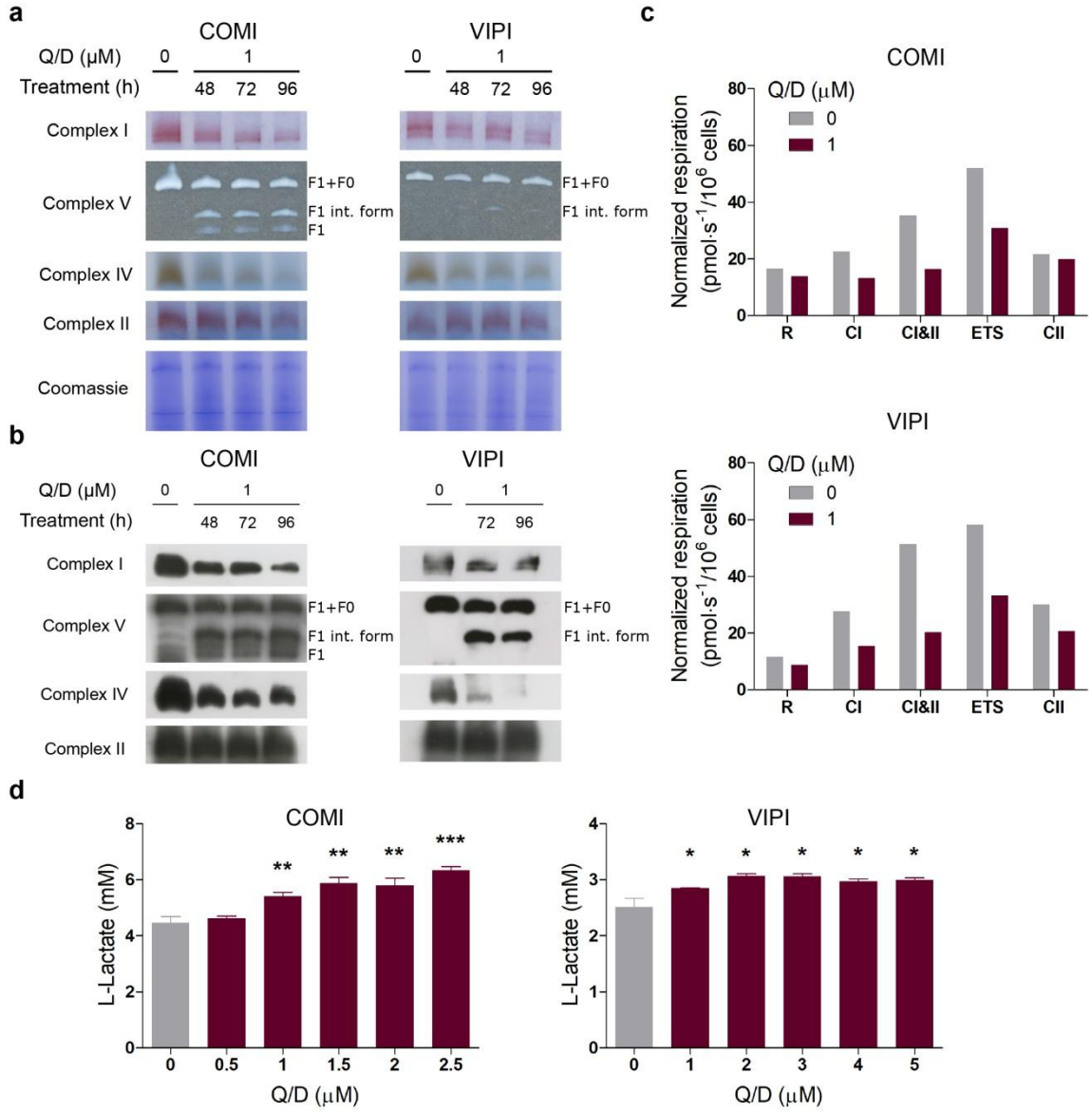

Figure 3.17 Q/D dysregulates and impairs OXPHOS in GSCs. a. Effects on the functionality of OXPHOS complexes as assessed using BN-PAGE and in-gel activity assay on COMI and VIPI cells after 48, 72 and 96h of Q/D treatment (1 µM). Fifty micrograms of the mitochondrial extracts were loaded onto gels. Coomassie® staining serves as loading control. One representative result is shown, n=2 biological replicates. **b.** Immunoblotting subsequent to BN-PAGE to assay for proteins belonging to complex I, V, IV and II. One representative result is shown, n=2 biological replicates. **c.** Oxygen consumption of COMI and VIPI cells upon 48h treatment with Q/D (1 µM) as measured using Oxygraph-2k. Cells were evaluated for routine (R), complex I (CI), complex I and II (CI&II), uncoupled (ETS) and complex II (CII) respiration. Representative results of n=3 biological replicates. **d.** Effects of increasing concentrations of Q/D on L-lactate production in COMI and VIPI cells after 48h treatment of Q/D. The L-lactate levels were normalized on number of cells as estimated by Hoechst 33342 staining. n=3 technical replicates, mean ± SD. *p < 0.05, **p < 0.01, ***p < 0.001, unpaired two-tailed t test. One representative result is shown, n=3 biological replicates.

3.3.2 Q/D inhibits translation by directly binding to the mitoribosome

To obtain the proof that Q/D inhibits mitochondrial translation by directly binding to the mitoribosome, our collaborators in the laboratory of Alexey Amunts at the SciLifeLab in Stockholm used cryo-electron microscopy (cryo-EM) to determine the structure of the mitoribosome extracted from HEK293 cells treated with 5 μM of Q/D for 24h. The structure solved at 3.9Å resolution revealed that Q/D binds to the large ribosomal subunit (mt-LSU), with dalfopristin in the peptidyl-transferase center (PTC) and quinupristin at the entrance of the exit channel (**Figure 3.18a**). The cryo-EM density for dalfopristin indicates that, as expected, it was hydrolyzed with the loss of the diethylaminoethylsulfonyl group to form virginiamycin M1 (**Figure 3.18b**), an effect reported also in the pharmacology studies on Q/D (Bearden, 2004). By comparing the Q/D bound structure to the previously published unbound state (Amunts et al., 2015), it was possible to identify a number of molecular rearrangements induced by Q/D binding. The most prominent molecular rearrangement is the 90 degrees shift of adenine 2725 (A2725) (**Figure 3.18c**). Other residues affected by Q/D presence are uracil 2993 and 3072 (U2993 and U3072, **Figure 3.18c**), although uracil 3072 was not well resolved in the unbound structure (EMD2876), probably due to inherent flexibility.
Structure of Q/D bound to *E.coli* and *D. radiodurans* ribosome have been previously resolved (Harms et al., 2004; Noeske et al., 2014), with dalfopristin binding within the PTC and quinupristin at the entrance of the exit channel, as in our structure. A comparison with those structures shows that bacterial counterpart of A2725 (bacterial A2062) adopts a similar shift, whereas the equivalent of U3072 (bacterial U2585) is displaced by nearly 180 degrees, which has not been observed in the mitoribosome due to the absence of the diethylaminoethylsulfonyl group of dalfopristin that was hydrolyzed in the cellular media. In addition, a shift in the mitoribosomal U2993 that could not be detectedd in the bacterial counterpart was observed.

The high resolution cryo-EM structure defines the specific binding site of Q/D on the human mitoribosome and the consequent rearrangements it induces. Since Q/D was added to the cells and not during any of the purification steps, the structural data suggest that it is able to penetrate the mitochondrial outer and inner membranes and that it exerts the inhibitory effect on mitochondrial translation by directly binding to the mitoribosome.

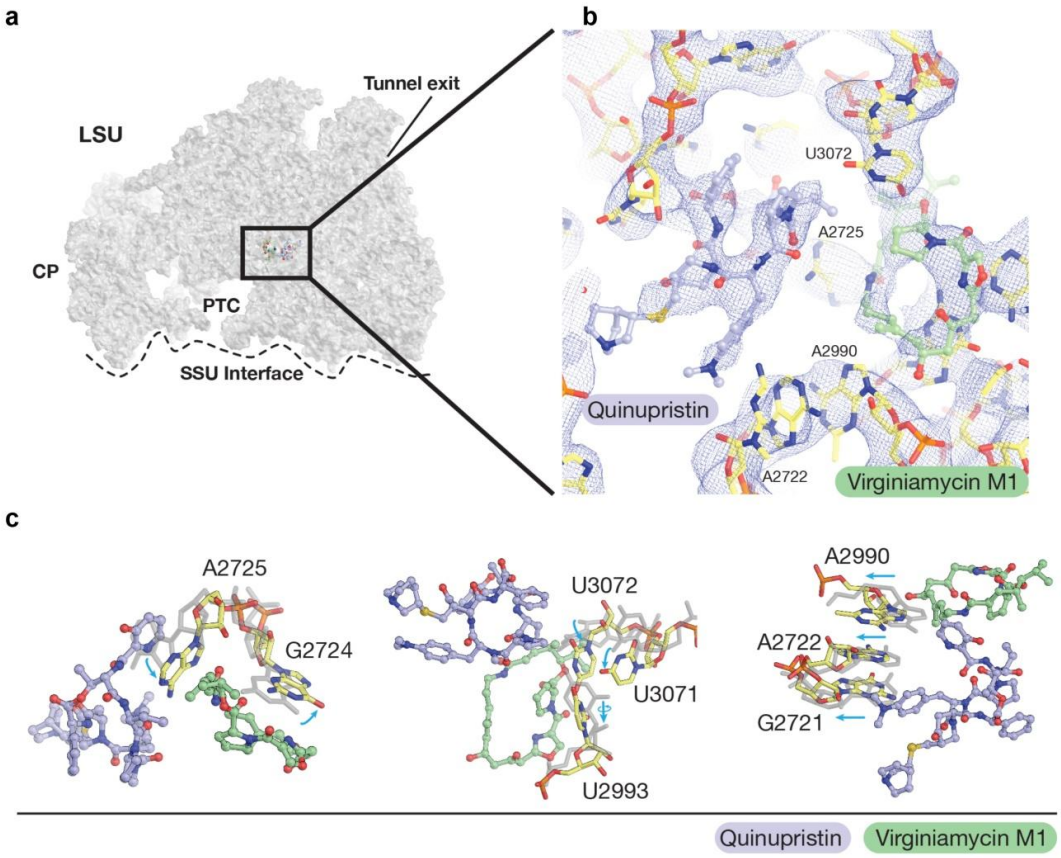

Figure 3.18 Cryo-EM structure of Q/D bound to the mitoribosome. a. Overall binding location of dalfopristin (hydrolyzed to virginiamycin M1) and quinupristin in the large subunit (LSU) of the human mitochondrial ribosome. HEK293 cells were incubated with 5 μM Q/D for 24h, after which mitoribosomes were prepared for cryo-EM. The two compounds are found just in the entrance to the exit tunnel after the peptidyl transferase center (PTC). **b.** View of the cryo-EM density around virginamycin M1 (green) and quinupristin (purple). The two compounds make interactions with the surrounding rRNA. **c.** Detailed comparison between the human mitochondrial ribosomal rRNA when bound to virginiamycin M1 and quinupristin (yellow) and when unbound (PDB ID: 3J9M, gray). Sky blue arrows indicate the rRNA movement to accommodate the molecules.

3.3.3 Inhibition of mitochondrial translation leads to Q/D-induced cytotoxicity on GSCs

I next investigated whether inhibition of mitochondrial translation and in consequence dysregulation of OXPHOS might be functionally related to Q/D-induced cytotoxicity on GSCs. First, I assessed the mitochondrial mass of eight GSC lines (COMI, VIPI, 030616, GB6, GB7, GB8, G144 and G166) by counting the number of COX4 positive spots per area of cytoplasm (approximate measurement of mitochondrial mass). Then, I treated the GSC lines with different concentration of Q/D (2.5, 5 and 10 μM) for 48h and, with the help of our

bioinformatician, I correlated the cell line susceptibility to Q/D treatment to their mitochondrial mass (**Figure 3.19**). I found that the cellular viability after Q/D treatment was negatively correlated to the mitochondrial mass (r=-0.882, p<0.001 at 2.5 µM; r=-0.758, p<0.05 at 5 µM; and r=-0.682, p=0.06 at 10 µM treatments), indicating that GSCs with higher mitochondrial mass are more susceptible to Q/D-induced cytotoxicity.

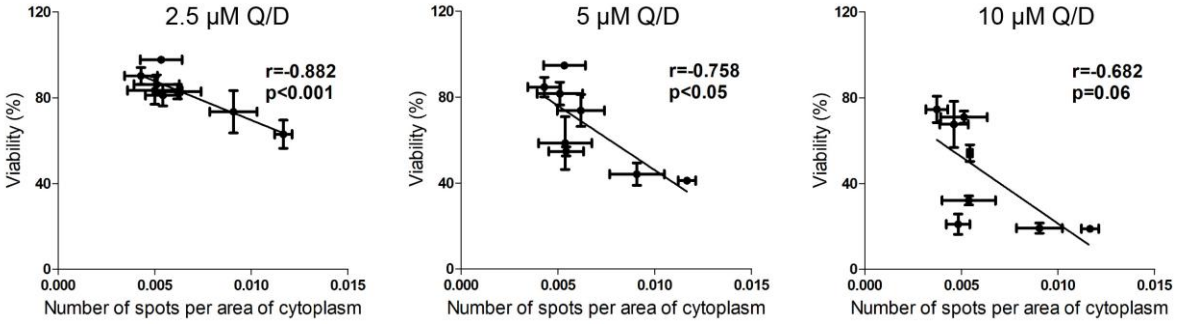

Figure 3.19 GSCs with higher mitochondrial mass are more susceptible to Q/D-induced cytotoxicity. Correlation analysis of mitochondrial mass (assessed by immunofluorescence with COX4 antibody and analysis of the number of COX4 spots per area of cytoplasm) and viability (Hoechst 33342 and PI staining) after 48h of Q/D treatment at 2.5, 5 and 10 µM for 8 GSC lines (COMI, VIPI, 030616, GB6, GB7, GB8, G144 and G166). n=3-5 biological replicates, mean, ± SD. Correlation values (r) and p values were calculated using the Pearson correlation coefficient.

GSCs are known to reside in dedicated tumor niches, anatomical regions defined by a unique microenvironment and presenting morphologically and functionally distinct features. GSCs have been found enriched also in the so called hypoxic niches (Li et al., 2009), characterized by hypoxic conditions. However, hypoxia does not preclude OXPHOS-reliance, in fact it has been shown that 1% oxygen is sufficient for GSCs to maintain OXPHOS (Janiszewska et al., 2012). In this context, we tested the sensitivity of COMI and VIPI cells to Q/D under different O_2 concentrations by assessing their viability after Hoechst 33342 and PI staining (**Figure 3.20a**). The O_2 concentration conditions used were: 21%, which I called "normoxic conditions", since it is the concentration of O_2 at which cells are normally grown *in vitro* and at which I usually performed the experiments, 1%, which I called "hypoxic conditions" and 0%, which I called "anoxic conditions", meaning that no O_2 was present. I also investigated the effect of Q/D on mitochondrial translation by COX1 and COX4 immunoblotting under these different O_2 concentrations (**Figure 3.20b**). I observed that cell viability of untreated cells was not affected under hypoxic conditions (1% O_2) and that the cells still responded to Q/D treatment in a dose-dependent manner (**Figure 3.20a**).

Moreover, the decrease in COX1 protein levels upon Q/D treatment was similar to that in normoxic conditions (21% O_2) (**Figure 3.20b**). Instead, anoxic conditions (0% O_2) deeply affected the viability of both lines but there was no further loss of viability upon Q/D treatment and the effect on the decrease of COX1 levels was no longer present. Further experiments could clarify the absence of effect of Q/D on COX1 protein levels under anoxic conditions (0% O_2).

Taken together, these findings show that under hypoxic conditions (1% O_2) Q/D can perfectly exert its cytotoxic effects due to mitochondrial translation inhibition, indicating that Q/D could also be able to affect those GSCs present in hypoxic niches.

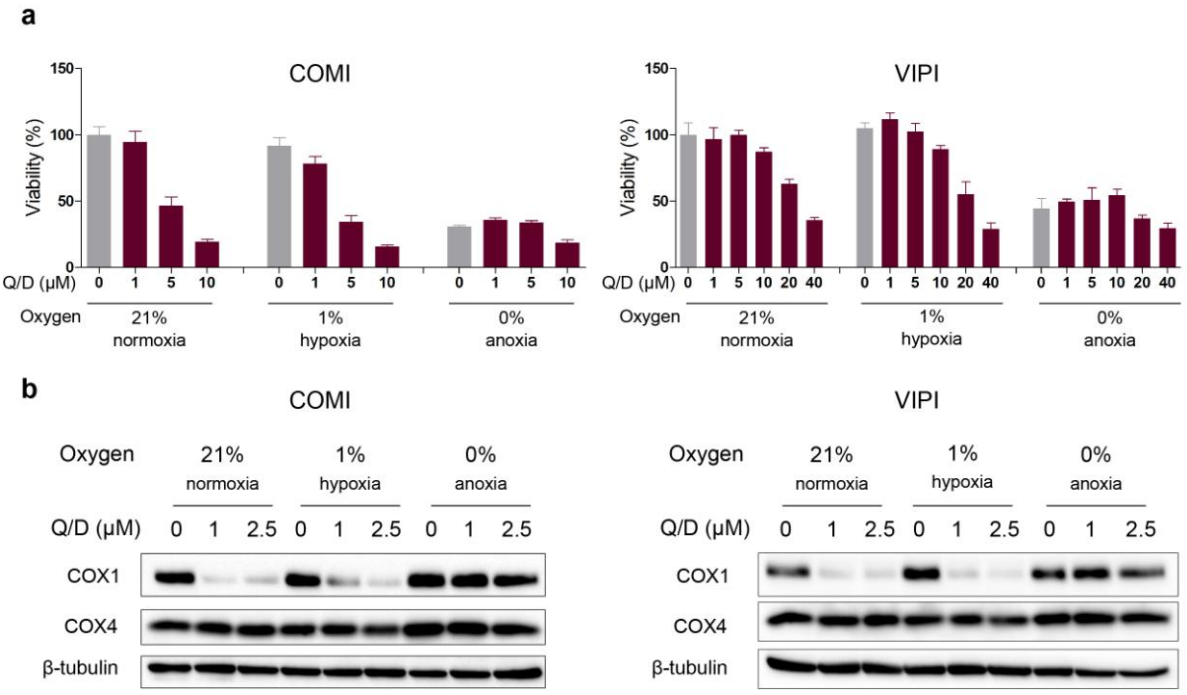

Figure 3.20 GSCs grown in hypoxic conditions (1% O_2) are sensitive to Q/D treatment. **a.** COMI and VIPI cells were treated with Q/D (1, 5, 10 μM for COMI and 1, 5, 10, 20, 40 μM for VIPI) under different oxygen concentrations (21%, 1% and 0%) for 48h and the viability was assessed after Hoechst 33342 and PI staining. n=4 technical replicates, mean ± SD. Representative result of n=3 biological replicates. **b.** Effects of varying oxygen and Q/D concentrations (1 and 2.5 μM) on COX1, COX4 and beta tubulin protein expression as assayed by immunoblotting on COMI and VIPI cells after 48h of treatment. Representative result of n=2 biological replicates.

I, then, examined the effect of Q/D treatment on the differentiated GSC progeny. To this aim, I differentiated three GSC lines (namely COMI, VIPI and GB7) by culturing them in media deprived of growth factors and supplemented with 10% FBS for 14 days, and assessed the level of differentiation by checking the expression of stemness (SOX2 and NESTIN) and differentiation (GFAP) markers by immunofluorescence, as reported in **Figure 3.21a**.

COMI and GB7 cells differentiated to a greater extent than VIPI, as evidenced by a higher increase in the expression of GFAP and decrease of SOX2 and NESTIN upon differentiation (**Figure 3.21b**).

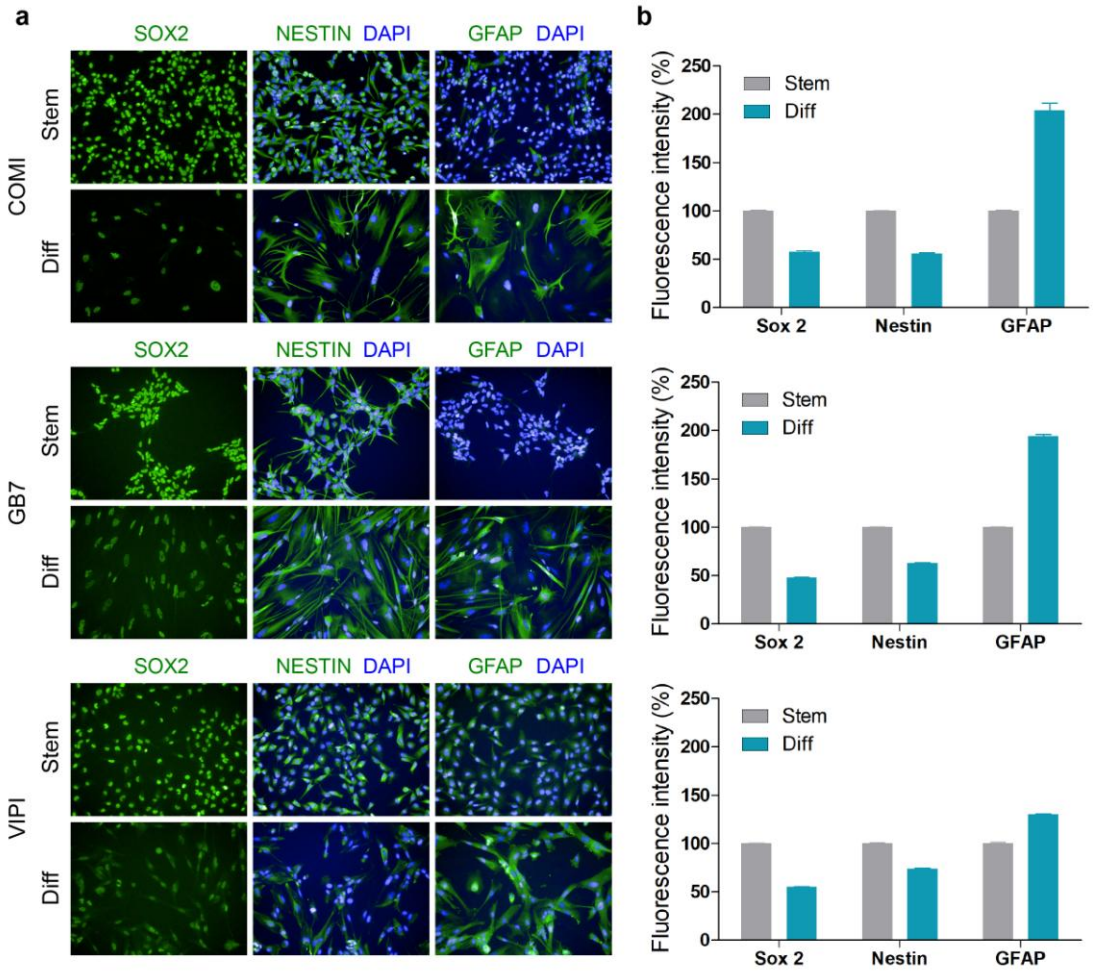

Figure 3.21 Differentiation analysis of GSCs. a,b. Immunofluorescence staining on COMI (*top*), GB7 (*middle*) and VIPI (*bottom*) cells for stemness (SOX2 and NESTIN) and differentiation (GFAP) markers. COMI, GB7 and VIPI lines were grown in standard cancer stem cell medium or differentiated for 14 days in medium deprived of growth factors and supplemented with 10% FBS. **a.** Representative immunofluorescence images. **b.** Quantification of the normalized intensity of immunostaining of SOX2, NESTIN and GFAP. n=6000 objects for stem cells and n=1000 objects for differentiated cells, mean, ± SEM. Representative result of n=2 biological replicates.

Next, I assessed the mitochondrial mass of the three GSC lines and of their differentiated progeny by measuring the number of MitoTracker Orange positive spots per area of cytoplasm (approximate measurement of the mitochondrial mass). In parallel, I treated the cells (GSCs and their differentiated progeny) with different concentrations of Q/D for 48h, I assessed cellular viability, constructed dose-response curves and calculated the deriving GI_{50} values. The differentiated progeny of all the three GSC lines tested presented higher GI_{50} values compared to their stemness counterpart, indicating that the differentiated cells

are less sensitive to Q/D treatment (**Figure 3.22a**). In detail, for COMI and GB7 lines, which differentiated to a greater extent than VIPI, the change in the GI_{50} values between stem and differentiated cells was remarkable. In fact, the GI_{50} values were of 6.5 μM ±1.1 and of 73.5 μM ±17.8 for COMI cells and their differentiated progeny, respectively, and of 4.3 μM ±0.8 and of 33.0 μM ±9.9 for GB7 cells and their differentiated progeny, respectively. The GI_{50} values increased from 7 to 11 fold upon differentiation in these two cell lines. The decrease in sensitivity of the differentiated cells corresponded to a lower mitochondrial mass as shown in **Figure 3.22b**. For VIPI cells, instead, which differentiated less than COMI and GB7, the change in the GI_{50} values between stem and differentiated cells was modest. The GI_{50} values were of 20.2 μM ±1.4 and of 33.0 μM ±9.3 for VIPI cells and their differentiated progeny, respectively. The smaller decrease in Q/D sensitivity of the less differentiated VIPI cells is also concordant with the lack of change in the mitochondrial mass, and could be due to worse differentiation efficiency. Taken together, these results demonstrate that differentiated cells show lower responsiveness to Q/D, suggesting that Q/D is preferentially more active on GSCs than on differentiated cancer cells.

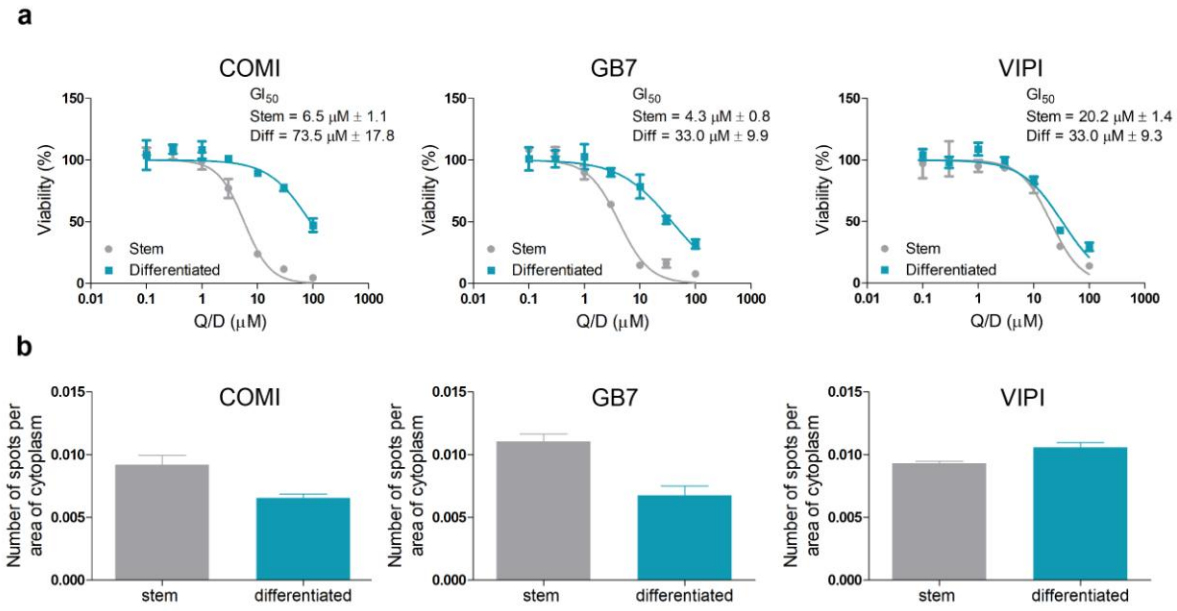

Figure 3.22 Differentiated GSCs are less sensitive to Q/D compared to their stemness counterpart. a. Representative dose-response curves for COMI, GB7 and VIPI cells (stem) and their differentiated counterpart (differentiated, diff). The cells were treated with Q/D (0.1, 0.3, 1, 3, 10, 30 and 100 μM) for 48h, after which they were stained with Hoechst 33342 and PI and the number of live cells was evaluated using Operetta-High Content Imaging System and Harmony software. The GI_{50} values were calculated using n=4-7 biological replicates, mean ± SD. **b.** COMI, GB7 and VIPI lines were grown in standard cancer stem cell medium or differentiated for 14 days in medium deprived of growth factors and supplemented with 10% FBS. Mitochondrial mass was assessed by counting the number of MitoTracker Orange positive spots per area of cytoplasm as defined with Cell Mask staining. Analysis was performed using Operetta High-Content Imaging System and Harmony Software. n=10 technical replicates, mean ± SD. Representative result of n=3 biological replicates.

3.4 Q/D DYSREGULATES CELL CYCLE AND INDUCES AUTOPHAGY

I next investigated the effect of Q/D on cell cycle, by performing EdU-PI staining upon treatment with increasing concentrations of Q/D (48h), and by measuring the percentage of cells in each phase of the cell cycle (**Figure 3.23a,b**). Increasing concentrations of Q/D led to a marked dose-dependent decrease in the number of cells in the S-phase, indicating inhibition of proliferation. In addition I observed a significant increase in the number of cells in the G0/G1 phase at 5 μM D/Q treatment, indicating an accumulation of cells in this phase, followed by an increase in the number of cells in the G2/M starting at 5 μM and culminating at 10 μM D/Q treatment (**Figure 3.23a,b**). These results suggest that Q/D critically dysregulates cell cycle progression.

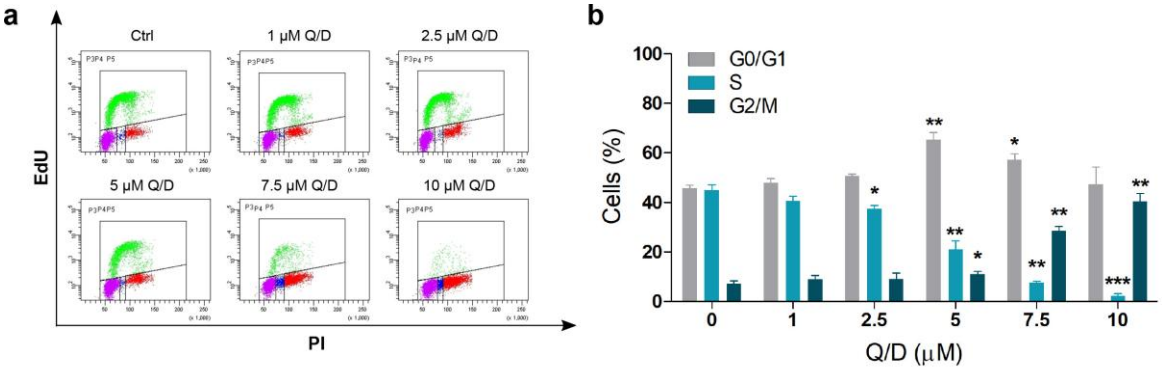

Figure 3.23 Q/D dysregulates cell cycle progression. a-b. Effects of Q/D on the cell cycle in COMI cells assayed using EdU incorporation and PI staining. **a.** Representative images of one biological replicate. **b.** Quantification of the percentage of cells in each phase. n=3 biological replicates, mean ± SD. *p < 0.05 **p < 0.01 ***p < 0.001, unpaired two-tailed t test.

As Q/D decreases cell proliferation and dysregulates cell cycle, I next studied the cell death mechanism induced by Q/D. I performed a flow cytometric analysis using Annexin V and PI staining, and estimated the percentage of apoptotic cells by calculating the percentage of Annexin V positive cells (**Figure 3.24a,b**). Treatments with a concentration of Q/D corresponding to the GI_{50} value for this cell line (6.5 μM) did not lead to a statistical significant increase in the percentage of apoptotic cells, which was observed only at higher Q/D concentration (10 μM) (**Figure 3.24a,b**). Further experiments to elucidate the fate of the cells treated with Q/D are necessary and are currently being performed in our laboratory.

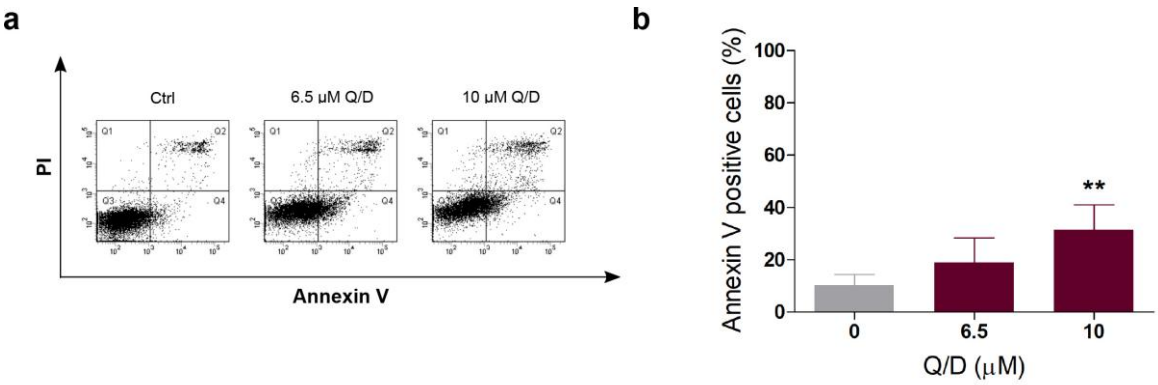

Figure 3.24 Q/D and apoptosis. a-b. Assessment of apoptosis upon treatment with Q/D (6.5 and 10 µM) in COMI cells by Annexin V and PI staining. **a.** Representative images of one biological replicate. **b.** Quantification of Annexin V positive cells. n=6 biological replicates, mean ± SD. **p < 0.01, unpaired two-tailed t test.

Since induction of autophagy upon drug treatment has been reported in some cases (Angeletti et al., 2016; Shchors et al., 2015), I investigated whether GSCs treated with Q/D undergo autophagy induction. Autophagy is a self-degradative mechanism that has been linked to cellular starvation and metabolic stress. In cancer, autophagy has been indicated either as a cell death mechanism, or as an adaptive and protective survival promoting mechanism (Angeletti et al., 2016). In both the cases, upon autophagy induction, the autophagosomes are formed and then, in the presence of a functional autophagic flux, the autophagosomes fuse with the lysosomes, resulting in lysosomal cargo degradation. Autophagy induction can be assessed by performing immunofluorescence (IF) and immunoblotting using the autophagy marker LC3B. Upon induction of autophagy, the LC3B isoform I (LC3B-I) gets converted into the isoform II (LC3B-II) through lipidation. LC3B-II is observed as LC3-positive puncta in IF or as a faster migrating LC3 band in SDS-PAGE (Mizushima et al., 2010). Autophagy can be better observed in the presence of lysosomal inhibitors, which prevent cargo degradation and lead to LC3B-II accumulation (Jawhari et al., 2016).

I treated GSCs with the lysosomal inhibitors chloroquine (CQ), bafilomycin (Baf) and ammonium chloride (NH_4Cl) alone or in combination with Q/D, and further evaluated if Q/D induces autophagic flux by visualizing the LC3B autophagic marker. First, I performed immunofluorescence analysis and observed autophagosomes formation by assessing the LC3B puncta formation (**Figure 3.25a**). All treatments resulted in an increase in the number of LC3B puncta, which were further augmented when Q/D was used in combination with lysosomal inhibitors (**Figure 3.25b**). I obtained the same results by immunoblotting using anti-LC3B antibody. Here, I observed an increase in the LC3B-II band upon treatments,

which was stronger in the Q/D combination treatments (**Figure 3.25c,d**). Overall, these results suggest that Q/D causes an increase in the autophagic flux.

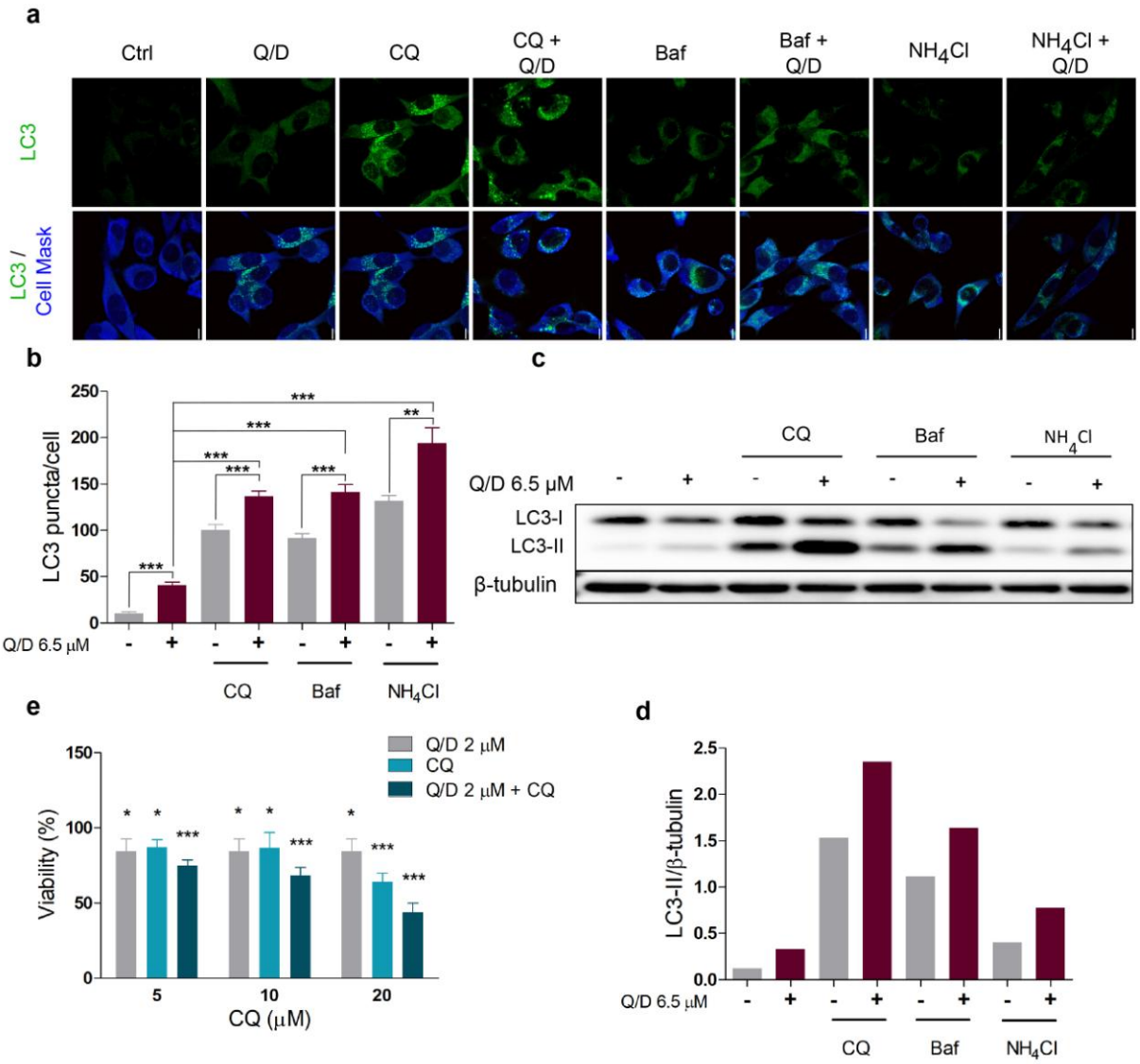

Figure 3.25 Q/D induces autophagy. a-d. Effects of Q/D treatment (6.5 μM) on autophagy in COMI cells. **a.** Autophagy induction was assessed by immunofluorescence using anti-LC3B antibody. Treatment with chloroquine (CQ), bafilomycin (Baf) and ammonium chloride (NH_4Cl) was used to assay for autophagic flux. Example images for each treatment condition are shown. **b.** The number of LC3B puncta per cell was quantified from at least 25 cells for each condition using ImageJ Software. One representative result is shown, n=2 biological replicates. **c.** Autophagy induction was assessed by immunoblotting on LC3B protein. Representative images of one biological replicate. **d.** LC3B-II form was quantified using densitometric analysis and normalized on β-tubulin. One representative result is shown, n=3 biological replicates. **e.** Evaluation of the role of autophagy in Q/D cytotoxic activity on GSCs. COMI cells were treated with Q/D 2 μM (black bars), chloroquine (CQ) 5, 10 and 20 μM (gray bars) or with the combination of all doses of the two drugs for 48h (pre-treatment with CQ for 3h); Cell viability was assessed by Hoechst 33342-PI assay. n=3 biological replicates, mean ± SD. *p < 0.05 **p < 0.01 ***p < 0.001, ANOVA followed by Dunnett's *post-hoc* test.

As previously described, autophagy has been indicated not only as a cell death mechanism but also as a protective mechanism. Thus, I investigated whether Q/D induced autophagy could have a pro-death or pro-survival function in GSCs. I inhibited the autophagic flux using chloroquine (CQ) and investigated the cell sensitivity to Q/D. If autophagy induction functions as a pro-death mechanism, I would expect a decrease in the drug sensitivity when combined with CQ, whereas I would expect an increase in sensitivity in the case of a pro-survival function. I observed a small but significant decrease in the viability upon the combination treatment (**Figure 3.25e**). Therefore, these results suggest that autophagy is a pro-survival mechanism, which is activated by GSCs to counteract the anti-proliferative effect induced by Q/D treatment. These data are in line with those reported by Angeletti and colleagues on GSCs treated with givinostat, a pan-histone deacetylase inhibitor endowed with anti-proliferative and pro-apoptotic activities (Angeletti et al., 2016).

3.5 Q/D IS ACTIVE *IN VIVO*, BEING ABLE TO REDUCE THE GROWTH AND INVASION OF GSC BRAIN XENOGRAFTS

Human GSCs grown under serum-free culture conditions are able to generate tumors that reproduce the histological and molecular features of the parent neoplasm when orthotopically injected in immunocompromised mice (Eramo et al., 2006; Galli et al., 2004; Singh et al., 2004). A feature of the deriving tumor xenografts is the highly infiltrative cellular growth pattern that closely mimics the behavior of malignant human gliomas. Our collaborator group headed by Prof. Roberto Pallini at the Università Cattolica del Sacro Cuore, in Rome, tested the effect of systemic administration of Q/D *in vivo* on tumor xenografts generated by GSCs injection. To produce tumor xenografts, they used a stable GFP-expressing GSC line (GFP-GSC#1) endowed with a high propensity to invade the brain. At eight weeks after implantation, the mice were treated with Q/D (200 mg/kg ip in PBS) or with PBS as control, three times a week for three weeks. One week after discontinuation of therapy, the mice were sacrificed and the brains were analyzed. Control mice (n=4) harbored tumors that invaded the homolateral striatum, piriform cortex, corpus callosum, anterior commissure, internal capsule, optic tract, septal nuclei, and fimbria (**Figure 3.26a**). In Q/D-treated mice (n=4; **Figure 3.26a**), these brain regions were also populated by tumor cells, however, the degree of brain invasion was dramatically reduced. The treatment with Q/D significantly lowered the density of tumor cells in the thalamus, fimbria, and optic tract of the grafted brain (**Figure 3.26b** for quantification).

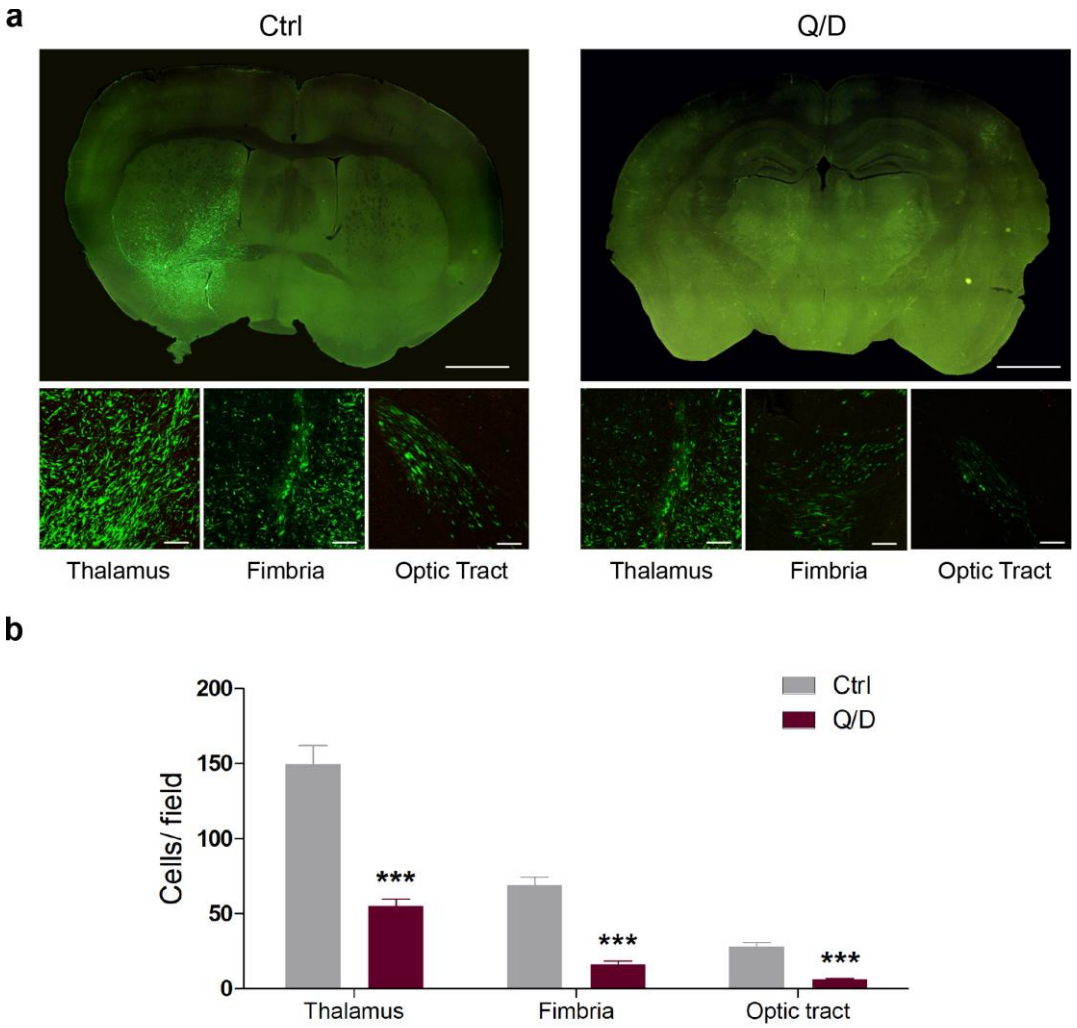

Figure 3.26 Q/D reduces the growth and invasion of GSC brain xenografts. a. Coronal brain sections of GFP-expressing GSC xenografts (*upper panels*), scale bar 1000 μm. Details of brain regions invaded by GSCs (*lower panels*), scale bar 200 μm. **b.** Number of GFP-expressing GSCc per high-power field in Q/D-treated and in control mice brain xenografts.

Being Q/D an already FDA approved drug, its pharmacokinetic properties have been studied in depth. In 1997, Bergeron and Montay reported a study on the pharmacokinetic profile of Q/D performed in rats, monkeys and healthy human volunteers (Bergeron and Montay, 1997). Using a radiolabelled form of Q/D, they studied its distribution profile both in rat and in monkey animal models. Q/D did not penetrate into the central nervous system in significant amount. Moreover, Q/D levels in the brain were the lowest among all the organs tested, with values around 0.01 mg of equivalent Q/D per gram of tissue (Bergeron and Montay, 1997). Clearly, Q/D is not able to cross an intact blood-brain barrier (BBB). In this contest, the evaluation of the integrity of the BBB in the GSC brain xenografts used to evaluate Q/D efficacy in mouse models was important to have a complete picture of Q/D activity *in vivo*.

The integrity of the blood-brain barrier (BBB) in the tumor region was assessed by performing immunofluorescence against the BBB glucose transporter Glut1, which stains for the endothelial component of the BBB. The microvasculature of the tumor xenografts showed different degrees of BBB integrity. In the tumor core, most of the microvessels lacked a continuous Glut1 staining, suggesting a completely disrupted BBB, whereas in the periphery of the tumor, microvessels with an unharmed BBB were frequently found (**Figure 3.27a,b**).

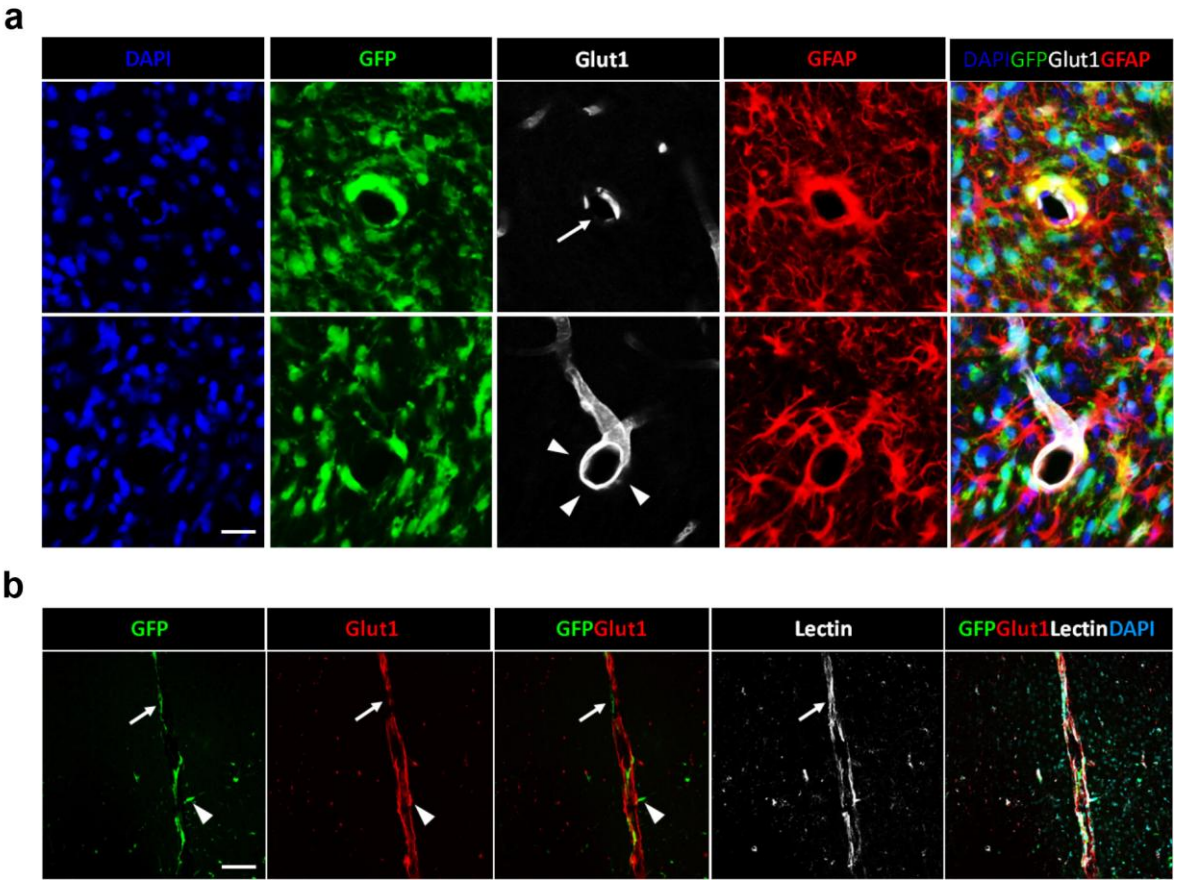

Figure 3.27 Assessment of blood brain barrier (BBB) in brain xenografts of GFP-expressing GSC#1. a. The microvasculature of the tumor xenografts shows different degrees of BBB changes, as assessed by anti-Glut1 immunofluorescence. In the tumor core (*upper panel*), most of microvessels lack continuous Glut1 staining (*arrow*), suggesting disruption of BBB. In the periphery of tumor (*lower panel*), microvessels with preserved BBB are frequently found (*arrowheads*). GSCs, *green*; astrocytes, *red*; nuclei, *blue*. Scale bar, 25 µm. **b.** Single tumor cells spreading along perivascular spaces of the BBB, which is either disrupt (*arrow*) or preserved (*arrowhead*). GSCs, *green*; BBB, *red*; endothelium, *white*; nuclei, *blue*. Scale bar, 150 µm.

In parallel, the presence of Q/D-induced systemic toxicity was evaluated by performing histological analysis on different organs (liver, spleen, lung and kidney). A small vacuolation of epatocytes around the arterioles and central vein of hepatic lobules was detected in Q/D treated mice, but no pathological changes were detected in the other systemic organs (**Figure 3.28**).

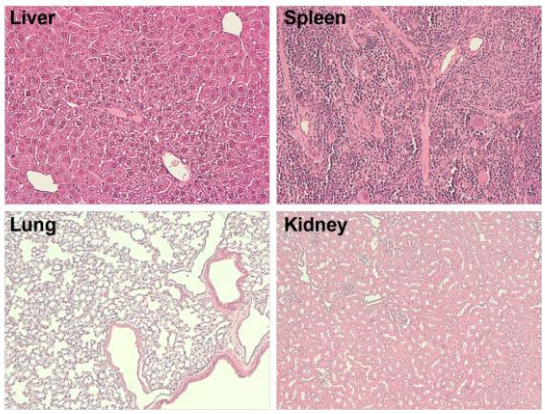

Figure 3.28 Histological examination of liver *(top left)*, spleen *(top right)*, lung *(bottom left)* and kidney *(bottom left)*. Mice were treated i.p. with 200 mg/kg of Q/D three times a week for 3 weeks. Treatment with Q/D resulted in vacuolation of hepatocytes located around the arteriole and central vein of hepatic lobules. No pathological changes were detected in the other systemic organs.

Taken together, these results show that Q/D administrated by i.p. injection is able to overcome the BBB when it is partially compromised and to reduce the growth of GSCs also *in vivo*, potently reducing the degree of brain invasion.

4. DISCUSSION

Strenuous efforts have been made in the past years searching for novel therapeutic strategies in the treatment of GBM, although none of the studies has produced satisfying outcomes (Khosla, 2016), underlying the urgent medical need for developing novel approaches and more effective drugs. GBM aggressiveness is associated with its glioblastoma stem cells (GSCs) component that is responsible for tumor invasiveness and therapy resistance (Bao et al., 2006; Chen et al., 2012). Hence, new therapies specifically leading to GSCs eradication could affect tumor invasiveness and prevent disease recurrence. Cancer stem cells (CSCs) of different tumor types, including glioblastoma stem cells (GSCs) (Janiszewska et al., 2012; Vlashi et al., 2011), have been shown to depend on mitochondrial respiration for their high energy demand (reviewed in Sancho et al., 2016; Viale et al., 2015). A growing body of literature suggests that targeting mitochondria, and in particular mitochondrial respiration, in tumors results in destabilization of energy homeostasis in cancer stem cells therefore providing a new target for therapy (reviewed in Ashton et al., 2018; Marchetti et al., 2015; Martinez-Outschoorn et al., 2017; Weinberg and Chandel, 2015).

We reasoned that by inhibiting mitochondrial translation we could hamper oxidative phosphorylation (OXPHOS) complex formation, leading to detrimental effect on GSCs viability. Based on the evolutionary similarity between mitochondrial and bacterial translation systems (i.e. ribosomes) (Amunts et al., 2015; Brown et al., 2014; Greber et al., 2014b, 2014a, 2015), we decided to evaluate the cytotoxic potential of bacterial ribosome-targeting antibiotics on GSCs.

We performed a high-content imaging driven screening on a library of compounds known to affect bacterial translation that led to the identification of three classes of antibiotics, namely streptogramins, pleuromutilins and tetracyclines, having cytotoxic and/or mitotoxic effect on two GSC lines (**Figure 3.5**). The potential use in cancer therapy has already been described for tetracyclines, and in particular for tigecycline, which acts by directly inhibiting mitochondrial translation in myeloid leukemia stem cells (Kuntz et al., 2017; Škrtić et al., 2011). The promising results obtained by Skrtić *et al.* have led to a phase I clinical trial to evaluate tigecycline in the treatment of acute myeloid leukemia (clinicaltrials.gov ID: NCT01332786). Recently, another tetracycline antibiotic, doxycycline, has been shown to prevent TMZ-induced increase of GSCs tumorigenicity in GBM (William et al., 2018),

supporting the idea of mitochondrial translation inhibition as anti-cancer targeted therapy in GBM. Interestingly, streptogramins have not been assayed as cancer therapy before.

We evaluated the cytotoxic effects of several commercially-available members of the three selected classes on GSCs growth and identified the streptogramins class as the most effective on GSCs (**Figure 3.6** and **Figure 3.7**). In our hands, streptogramins were more potent than tetracyclines in reducing GSCs growth *in vitro*. Among all the streptogramins, the combination of quinupristin/ dalfopristin (Q/D) was identified as the most effective compound. Compared to tigecycline and doxycycline, Q/D resulted at least two times more cytotoxic on GSCs (6 times on COMI cells compared to tigecycline and 8 times on COMI cells compared to doxycycline). Interestingly, in the previously reported studies tigecycline and doxycycline were not chosen based on a comparative study of bacterial ribosome inhibitors (Škrtić et al., 2011; William et al., 2018), as Q/D was in our case.

Q/D is an FDA-approved drug traded as Synercid® and used in the hospitals for the treatment of infections associated with vancomycin-resistant *Enterococcus faecium* and complicated skin and skin structure infections caused by methicillin-susceptible *Staphylococcus aureus* or *Streptococcus pyogenes* (Delgado et al., 2000; Gurk-Turner, 2000). Quinupristin belongs to group B streptogramins, whereas dalfopristin belongs to group A streptogramins. Quinupristin and dalfopristin are produced by semisynthesis starting from virginiamycin S1 and virginiamycin M1, respectively, and are used in a specific 30:70 (w/w) ratio. Streptogramin A and B are known to act synergistically in bacteria (Di Giambattista et al., 1989) and this has been proven for Q/D as well (Barriere et al., 1992).

We showed that Q/D is cytotoxic on a wide panel of GSCs, both grown as adherent cultures and as neurospheres (**Figure 3.11**, **Figure 3.12** and **Figure 3.13**). We also demonstrated that this combination is able to reduce the neurosphere formation ability of GSCs (**Figure 3.14b**), a feature associated to the tumorigenic nature of this cell population. A critical point when evaluating a potential anticancer drug is to determine its ability to discriminate between cancer and normal cells. We showed that Q/D preferentially targets GSCs rather than normal astrocytes or normal fibroblasts (**Figure 3.14a**), showing a discrete therapeutic window. GSCs are known to be resistant to radio and chemotherapies (Bao et al., 2006; Chen et al., 2012). Indeed, we showed that Q/D is over ten times more potent than the currently used drug TMZ on GSCs (**Figure 3.15**). Importantly, the concentration of Q/D necessary to inhibit the 50% of GSCs growth (GI_{50} values) corresponds to concentrations achievable in patients' blood, which vary between 10.7 and 24.2 µg/mL, with an injection of 12.6 to 29.4 mg/kg respectively (corresponding to 14 – 32 µM) (Bergeron and Montay, 1997).

A critical role of OXPHOS in the energetic metabolism of GBMs and GSCs has been recently emerging by different lines of evidence. The degree of activation of the OXPHOS chain in GBM tumors has been associated to GBM malignancy, since high levels of complex IV functionality are an independent negative prognostic factor in GBM (Griguer et al., 2013). Targeting the function of this complex by two different small molecule inhibitors was recently shown to be effective on GSCs both *in vitro* and *in vivo* (Oliva et al., 2016, *ibid.* 2017). Moreover, acquisition of chemoresistance to TMZ in glioblastomas is associated with increased mitochondrial coupling and decreased reactive oxygen species (Oliva et al., 2011), thus linking altered OXPHOS also to chemoresistance. Interestingly, remodeling of OXPHOS chain complexes as adaptation to TMZ selection could be different from a general overactivation (Oliva et al., 2010). Moreover, depletion of the oncofetal insulin-like growth factor 2 mRNA-binding protein 2 (IMP2), which is elevated in aggressive GBMs and promotes translation of the mtDNA encoded OXPHOS proteins thus maintaining OXPHOS functionality, also induces GSCs loss of clonogenic potential and tumorigenicity *in vivo* (Janiszewska et al., 2012). Taken together these data reinforce the connection between altered OXPHOS activity and GSC aggressiveness and/or treatment resistance.

A compelling evidence of this relationship was provided with a study describing the molecular outcome of the rare *FGFR3-TACC3* (F3–T3) gene fusion present in 3% of GBM cases and in other kind of cancers (Frattini et al., 2018; Singh et al., 2012). This fusion activates OXPHOS and mitochondrial biogenesis and has been shown to possess a powerful oncogenic activity (Frattini et al., 2018). Importantly, increased OXPHOS activity triggered by F3-T3 confers special sensitivity to OXPHOS inhibitors.

In this exciting landscape of increasing awareness of the oncogenic role of dysregulated OXPHOS in GBM, we identified Q/D as a potent cytotoxic drug able to affect GSCs growth and provided important insights into the molecular mechanism of its action. We proved that Q/D acts *via* mitochondrial translation inhibition (**Figure 3.16a**, *left panel*) and therefore, by reducing mtDNA encoded proteins' expression levels (**Figure 3.16b,c**). This is in line with previous findings describing a similar mechanism of action for tigecycline in leukemia cells (Škrtić et al., 2011). We also showed that Q/D does not have any effect on cytosolic translation, even at five times higher concentrations of that used to inhibit mitochondrial translation (**Figure 3.16a**, *right panel*). We demonstrated that Q/D impairs OXPHOS complexes functionality and decreases mitochondrial respiratory capacity as a consequence of mitochondrial translation inhibition (**Figure 3.17a,b,c**). Furthermore, using Cryo-electron microscopy (Cryo-EM) we confirmed that Q/D binds to the mitoribosome by solving the structure of the mitoribosome with the drug bound inside at 3.9 Å resolution (**Figure 3.18**). In detail, the data indicate that Q/D binds to the large ribosomal subunit mt-(LSU), with dalfopristin in the peptidyl-transferase center (PTC) and quinupristin at the entrance of the

exit channel, as it happens in bacteria (Harms et al., 2004; Noeske et al., 2014). In our hands, dalfopristin was hydrolyzed to virginiamycin M1 in the cell culture media as previously described by Noeske and colleagues who reported that dalfopristin hydrolyzes very rapidly at pH 7.4 and 37°C (Noeske et al., 2014).
The fact that the density for quinupristin and virginiamycin M1 was observed from samples prepared using cells treated with Q/D for a period of 24 hours, indicates that not only these two compounds are able to directly bind to the mitoribosome but also that the molecules are able to penetrate three biological membranes to reach the mitochondrial matrix. The electron density revealed additional important aspects on Q/D binding to the mitoribosome and on the residues shifts Q/D induces.

Importantly, the structural information obtained by solving Q/D-mitoribosome structure paves the way toward a rational design of chemical analogues with potential improved potency and specificity and opens the route to medicinal chemistry optimization. By this approach it is possible to define the structural positions that can be chemically modified to confer a specific biological advantage. Even if we already showed that Q/D is capable to cross the outer and inner mitochondrial membrane and to accumulate in the mitochondrial matrix, a rational design driven by the structural information could guide the introduction of chemical moieties directed to increase the mitochondria-targeting potential of the drugs. A clear proof-of-concept of this approach has been recently demonstrated for metformin and biguanides (Cheng et al., 2016). Metformin is an anti-diabetic drug which has been shown to reversibly inhibit OXPHOS complex I (Wheaton et al., 2014), resulting in cytotoxic effects in different cancer stem cell lines, including breast, pancreatic, colon and also glioblastoma (Gou et al., 2013; Song et al., 2012; Würth et al., 2013; Zhang et al., 2013). Cheng and colleagues enhanced metformin antitumor activity by increasing its mitochondrial-targeting potential through the insertion of a positively-charged unit on a lipophilic substituent in the molecular structure. The synthetic derivative Mito-Met_{10} was almost 3 orders of magnitude more efficacious than metformin in inhibiting pancreatic cancer cell proliferation (Cheng et al., 2016).

On the other side, our structure could also help in the design of antibacterial analogues with higher bacterial ribosome selectivity and deprived of off-target mitochondrial side effects.

Q/D treatment leads to inhibition of mitochondrial respiration and dysfunctional OXPHOS complexes but it also slightly increases glycolysis (**Figure 3.17d**), therefore indicating that the cells try to compensate for ATP production loss by altering their bioenergetic homeostasis. This metabolic flexibility has been previously demonstrated by showing that inhibition of either glycolysis or OXPHOS has only marginal effects on the overall ATP

content, suggesting that the inhibition of glycolysis could be compensated by OXPHOS and *vice versa* (Vlashi et al., 2011). The ability to upregulate glycolysis appears to be cell type dependent, as for example pancreatic cells treated with mitochondrial respiration inhibitors were unable to compensate in this way (Viale et al., 2014). Future experiments will reveal the nature of this metabolic reprogramming and whether additional inhibition or dysregulation of compensatory metabolic pathways activated by mitochondrial metabolism inhibition could have a beneficial effect on tumor elimination. Promising results obtained by the simultaneous inhibition of glycolysis and mitochondrial metabolism have been reported. Sahra and colleagues showed that the mitochondrial complex I inhibitor, metformin, and 2-deoxyglucose used in combination were able to severely affect ATP production, leading to a dramatic cytotoxicity in prostate cancer cells, without any significant effect on normal prostate epithelial cells. Moreover, the combination of the two drugs was much more harmful compared to either the single drug used alone (Sahra et al., 2010). In line with these results, metformin cooperates with the FDA-approved GLUT4 inhibitor, ritonavir, to kill multiple myeloma cancer cells both *in vitro* and *in vivo* (Dalva-Aydemir et al., 2015), and the mitochondrial-targeted drugs Mito-CP and Mito-Q synergize with 2-deoxyglucose to significantly reduce breast cancer cells tumor in a xenograft mouse model (Cheng et al., 2012).

Our current findings show that under hypoxic conditions (1% oxygen) Q/D can perfectly inhibit mitochondrial translation and exerts its cytotoxic effects (**Figure 3.20**). This finding is central for future Q/D therapy of GBM, given the largely hypoxic nature of these tumors. GSCs have been found enriched in different tumor niches, comprising also the highly hypoxic niches (Li et al., 2009). Hypoxia have been demonstrated to not preclude OXPHOS; in fact it has been shown that 1% oxygen is sufficient for GSCs to maintain OXPHOS (Janiszewska et al., 2012).

We showed that Q/D preferentially targets GSCs rather than their differentiated progeny (**Figure 3.22a**). The preferential GSCs targeting by Q/D raises a fundamental key question. Would this be sufficient to eradicate GBM tumor or would the differentiated progeny then revert to a GSCs phenotype and lead to tumor relapse? It has been demonstrated that, under specific stimuli such as chemotherapeutic agents, GSCS progeny can undergo a plasticity transition and reacquire GSC features and tumorigenic potential (Auffinger et al., 2014). Therefore, it has been suggested that the combination of conventional treatments and GSCs or, more in general, CSCs targeted therapy should have better and faster therapeutic effects in total tumor elimination and patients' outcome improvement compared to monotherapies (reviewed in Cojoc et al., 2015). As for example, Chen and colleagues

showed that the combination of TMZ and GSCs ablation impeded tumor development in a gliomas mouse model. On the other hand, GSCs ablation alone was only successful in arresting tumor growth (Chen et al., 2012). On the same line, the co-delivery of doxorubicin and thioridazine, reported to be selectively cytotoxic for CSCs, showed a stronger antitumor effect both *in vitro* and *in vivo* in breast cancer tumors compared to monotherapies (Ke et al., 2014). In the light of these considerations, the co-administration of Q/D and TMZ could be taken into account for more effective and faster therapeutic effects for GBM treatment.

A critical point to consider when studying a drug candidate for the treatment of GBM is its ability to cross the blood-brain barrier and to reach the brain. The blood-brain barrier (BBB) is a highly selective semi-permeable membrane fundamental for central nervous system (CNS) homeostasis regulation and protection from toxins, pathogens and exogenous agents (Abbott et al., 2010; Daneman and Prat, 2015). It is the site for blood-CNS exchange, providing a total area of between 12 and 18 m^2 in the human adult (Abbott et al., 2010). The BBB is composed of a network of capillaries paved by vascular endothelial cells, which are highly connected by adherens and tight junctions and are surrounded by a discontinuous layer of pericytes. Microglia, nerve terminals and astrocyte end-feet encircle endothelial cells and cover the basal lamina of brain capillaries, playing an important role in BBB integrity maintenance (Abbott et al., 2010; Daneman and Prat, 2015).

The BBB regulates tightly the blood-CNS exchange. Very small molecules, gaseous molecules and solutes can cross the barrier by passive diffusion, depending on their physico-chemical properties. Essential nutrients uptake is mediated by carriers or receptors. On the other hand, potentially harmful exogenous compounds are efficiently extruded by different efflux transporters, such as ATP Binding cassette proteins (Abbott, 2013; van Tellingen et al., 2015).

Despite the common belief that GBM patients present a leaky and disrupted BBB, accumulating clinical evidence suggests that this is not completely true (Sarkaria et al., 2018). GBM are characterized by a highly infiltrating nature and consist of different regions endowed with different degrees of BBB integrity. While the BBB is completely compromised in bulky tumor areas, it is slightly leaky or even intact in more invasive peripheral tumor regions (Sarkaria et al., 2018; van Tellingen et al., 2015, **Figure 4.1**). Therefore, the evaluation of drug distribution across the BBB is still essential when designing therapies for treating GBM. In fact, compounds and macromolecules that are normally excluded from the brain by an intact BBB can cross the barrier and reach the brain in those regions where the BBB is compromised, but not where the BBB is still unharmed. Cancer cells that are not hit by chemotherapy would, then, be free to proliferate and give rise to tumor recurrence.

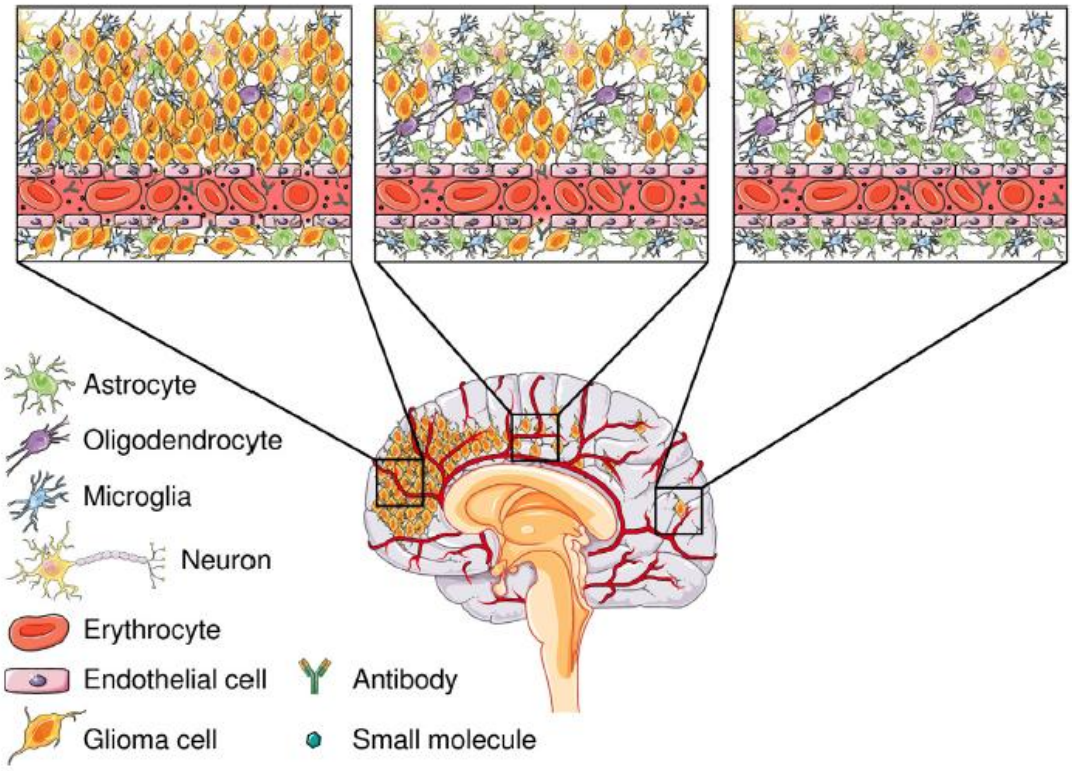

Figure 4.1 BBB integrity in different GBM regions. Glioblastoma BBB is completely compromised in bulky tumor areas *(left panel)*, whereas it is slightly leaky *(middle panel)* or even completely unharmed *(right panel)* in more peripheral tumor regions (van Tellingen et al., 2015).

By using patient-derived GSCs mouse brain xenografts, we evaluated the ability of Q/D to exert its anticancer effect *in vivo*. Systemically administered Q/D was able to dramatically reduce the degree of brain invasion (**Figure 3.26a,b**), decreasing the density of tumor cells in the thalamus, fimbria, and optic tract of the grafted brain.

In a previous study aimed at evaluating Q/D pharmacokinetic properties, Q/D was proposed not to be able to cross the BBB (Bergeron and Montay, 1997). In our xenografts of patient-derived GSCs, Glut1 immunofluorescence indicated that the tumor infiltrated brain harbors microvessels with regions presenting an unharmed BBB and other regions presenting a completely disrupted BBB (**Figure 3.27**). The partial BBB disruption explains the successful response to Q/D observed in the treated mice. A better understanding of Q/D ability to cross the BBB in GBM is warranted. In addition, alternative ways of administration or delivery could be explored. Numerous strategies to circumvent the BBB and to improve the delivery of agents to brain tumors have been investigated in the last decades. For example, the BBB can be transiently and reversibly opened using different agents, such as osmotic or biochemical disruptors, ultrasounds or magnetic radiation, resulting in an increased permeability. The use of ultrasounds and magnetic radiation is relatively safer compared to

osmotic or biochemical disruptors, since they allow a site-specific local BBB opening, preventing side effects caused by BBB generalized opening, such as neurological toxicity, aphasia and hemiparesis (reviewed in Tajes et al., 2014; van Tellingen et al., 2015). Alternatively, therapeutic agents can be delivered directly into the brain tumor parenchyma. One of the most promising approaches is the convection enhanced delivery, based on intraparenchymal placed microcatheters which, by creating a positive pressure gradient, allow the direct and continuous drug injection (reviewed in Jahangiri et al., 2017). Therapeutic agents can be directly delivered into the tumor resection cavity also by the use of biodegradable drug-impregnated polymer wafer implanted into the brain upon tumor surgical resection, as in the case of Gliadel wafers (Brem et al., 1995). Lastly, therapeutic agents can be entrapped, dissolved, encapsulated or attached to specific drug carrier systems, which are able to cross the BBB and deliver their “cargo” to the brain. Several drug carrier systems are being studied, including microspheres, liposomes, nanoparticles and exosomes (reviewed in Patel and Patel, 2017).

5. CONCLUSIONS

By performing a high-content imaging driven screening on a focused library of bacterial ribosome targeting antibiotics, we identified quinupristin/dalfopristin (Q/D) as a promising lead compound candidate due to its cytotoxic and mitotoxic effects on GSCs.

Q/D belongs to the streptogramin family of antibiotics and is traded with the name of Synercid®. Q/D was approved by the Food and Drug Administration (FDA) in 1999 to treat infections caused by susceptible strains of vancomycin-resistant *Enterococcus faecium* (VREF) and to treat complicated skin and skin structure infections caused by *Staphylococcus aureus* (methicillin-susceptible) or *Streptococcus pyogenes.*

We demonstrated that Q/D effectively prevents GSCs clonogenic expansion and that it exerts a cytotoxic effect on a wide panel of GSCs grown both as adherent cultures and as neurospheres. We showed that Q/D is over an order of magnitude more potent than TMZ, the only drug used in first line GBM therapy. In addition, Q/D displays a discrete degree of selectivity for GSCs compared to normal cells, such as astrocytes or lung fibroblasts. We also provided detailed evidence on Q/D mechanism of action. We showed that it acts *via* mitochondrial translation inhibition, leading to OXPHOS dysregulation and mitochondrial respiration capacity reduction. Moreover, using cryo-electron microscopy we obtained the structure of Q/D bound to the human mitoribosome, which provides the basis for the development of potentially more potent derivatives. Finally, we tested Q/D efficacy *in vivo* using xenograft mouse models of GBM and showed that it is able to dramatically reduce the degree of tumor cell brain invasion, decreasing the density of GFP-expressing GSCs in the thalamus, fimbria, and optic tract of the grafted brain.

Our results suggest that mitochondrial translation represents a therapeutic target for GBM and show that Q/D, acting *via* inhibition of mitochondrial translation, is effective against GSCs.

Drug repurposing of clinically used drugs for new useful therapeutic applications is an effective way of fast-tracking new drugs since toxicological and pharmacokinetic properties are already known. In this context, the extent of Q/D action, its degree of specificity, its successful effect in xenotransplanted mouse models after systemic administration and its known pharmacokinetics and toxicological profile make this antibacterial antibiotic a candidate drug for repositioning in GBM treatment. Given the urgent medical need for novel therapeutic approaches in GBM treatment, Q/D represents a promising therapeutic solution that is worth further preclinical and clinical investigations.

6. ONGOING WORK

6.1 DALFOPRISTIN IS SELECTED AS LEAD COMPOUND

Given that Q/D combination is already FDA approved as antibiotic and that its pharmacokinetic and toxicological properties are known, we speculated that it could be repurposed for GBM treatment. Nevertheless, quinupristin (Q) and dalfopristin (D) chemical structures could be modified in order to improve their affinity toward the mitoribosome and, hence, potentially increase their specificity and potency. By solving the structure of the mitoribosome with bound Q/D we defined the specific binding site of the two molecules and the consequent rearrangements they induce. This structural information gave us the possibility to investigate the design of new chemical derivatives. In order to determine whether to focus on one or both the molecular scaffolds we evaluated Q and D as separate molecules, taking into account both their cytotoxicity and their ability to inhibit mitochondrial translation.

Firstly, I assessed Q and D effect on cell growth by treating for 48h two GSC lines (COMI and VIPI) with a range of drug concentrations. I then determined cell viability using Hoechst 33342 and PI, constructed dose-response curves and calculated the deriving GI_{50} values (**Figure 6.1a**). Both Q and D resulted to be cytotoxic for GSCs more or less to the same extent of Q/D combination (Synercid®). Next, I determined the effect of the single molecules on mitochondrial translation by ^{35}S metabolic labeling and immunoblotting (**Figure 6.1b, c**). While D was able to inhibit mitochondrial translation as efficiently as Q/D combination, Q was not. The lack of mitochondrial translation inhibition by Q could be explained by the observation that streptogramins B alone have a lower affinity for the ribosome compared to streptogramins A and B combination, as previously described in bacteria (Contreras and Vázquez, 1977; Parfait et al., 1978). In fact, streptogramins A binding to the bacterial ribosome induces a “prepositioning” of A2062 residue (corresponding to A2725 in the mitoribosome), which creates a more defined binding pocket for the subsequent binding of streptogramins B (Noeske et al., 2014). On the contrary, streptogramins A do not need streptogramins B to bind to the bacterial ribosome, even though their activity in bacteria is potentiated by the presence of streptogramins B.

Based on these results, we decided to start the “derivatives design” by focusing on dalfopristin structure.

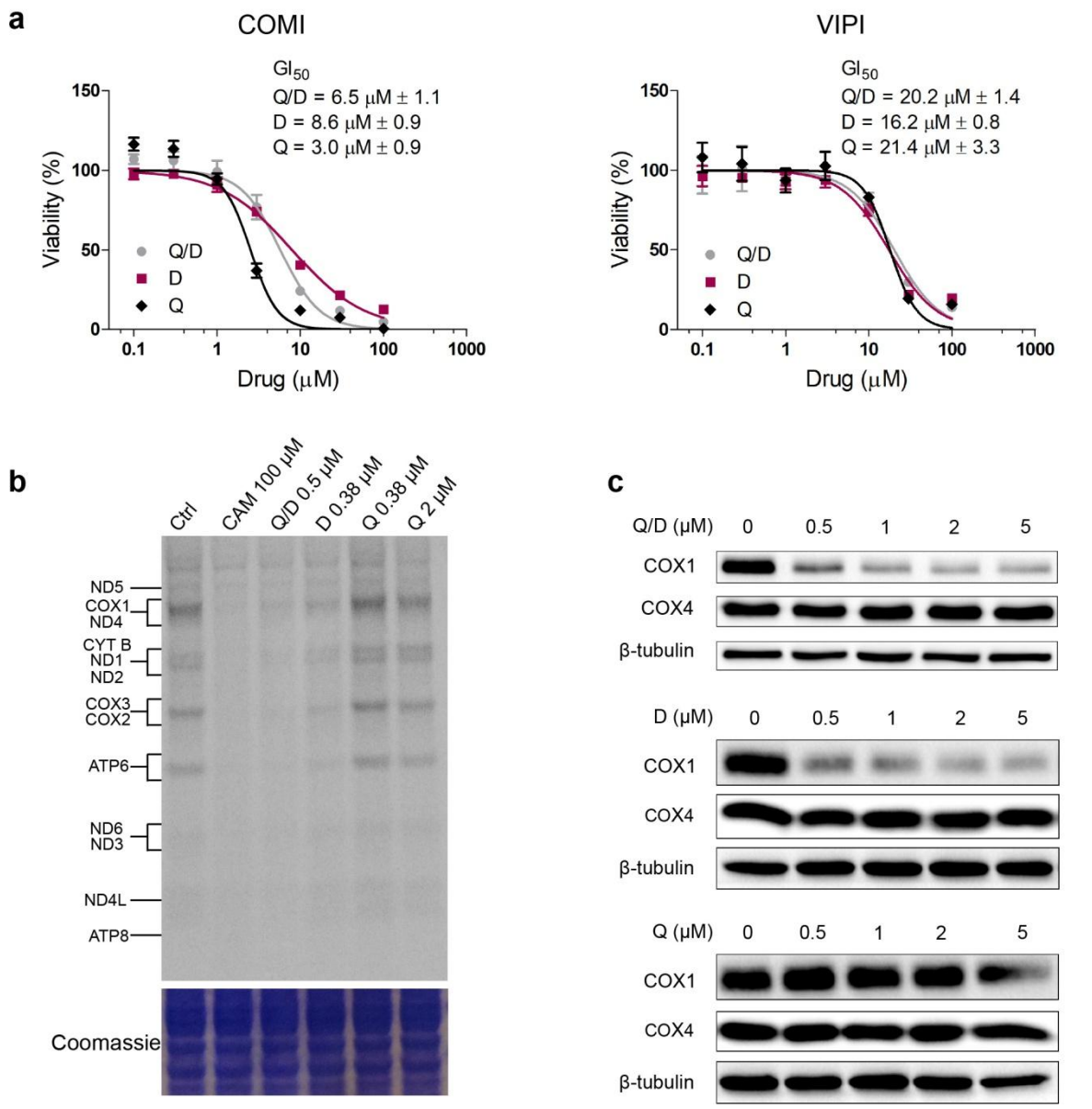

Figure 6.1 Dalfopristin is selected as lead compound. **a.** Representative dose-response curves for Q/D, quinupristin (Q) and dalfopristin (D) on COMI and VIPI cells. Chloramphenicol (CAM) was used as positive control. The cells were treated with Q/D or Q or D for 48h, after which they were stained with Hoechst 33342 and PI, and the number of live cells was evaluated using Operetta-High Content Imaging System and Harmony software. The GI_{50} values were calculated from n=3 biological replicates, n=4 technical replicates each, mean ± SD. **b.** ^{35}S metabolic labeling assay on mitochondrial translation on COMI cells after 24h treatment with Q/D, Q or D. Emetine was used to inhibit cytosolic translation. One representative result is shown, n=3 biological replicates. **c.** Effects of increasing concentrations of Q/D (*top*, as in **Figure 3.16c**), D (*middle*) or Q (*bottom*) on COX1, COX4 and beta tubulin proteins as assayed by immunoblotting on COMI cells after 48h treatment. One representative result is shown, n=2 biological replicates.

6.2 COMPUTATIONAL APPROACH FOR STRUCTURE BASED DESIGN

The cryo-EM structure of Q/D bound to the mitoribosome that we obtained set the basis for the design of more specific and potent derivatives. Computational methods have proven to be a powerful toolbox for the optimization of drug candidate molecules. In order to identify the best derivatives to be synthesized, we have recently started a collaboration with Prof. Stefano Moro at the University of Padova, who is currently using structure-based ligand design (SBLD) approaches to select D derivatives with higher affinity for the human mitoribosome (**Figure 6.2**).

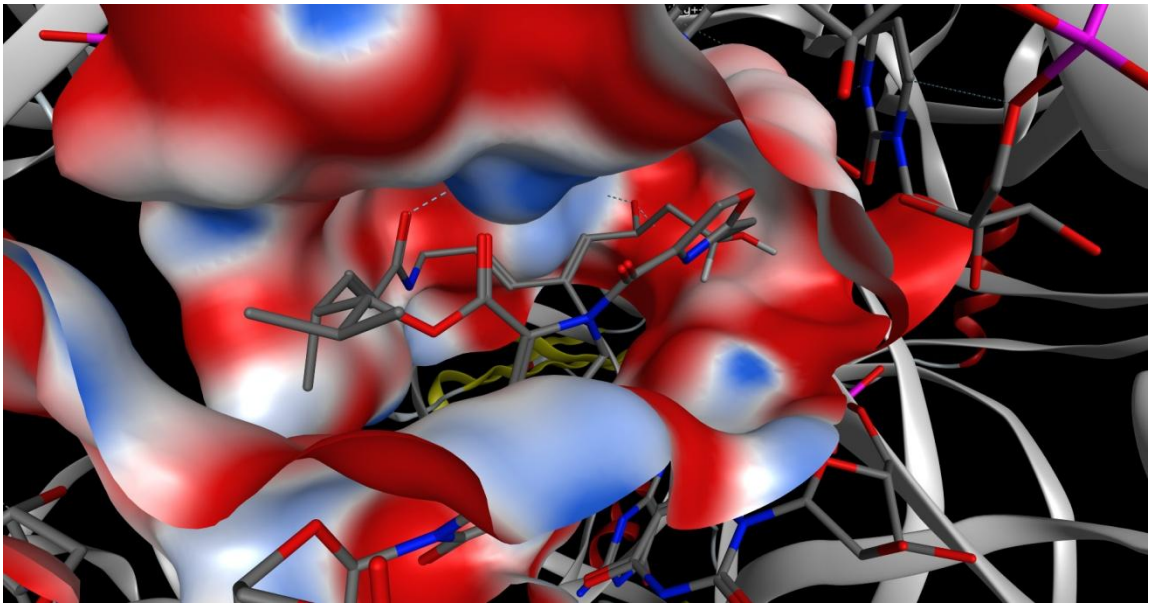

Figure 6.2 Docking calculation 3D view of dalfopristin in its binding site inside the mitoribosome. The mitoribosomal RNA secondary structure is represented in gray while the protein portion secondary structure is represented in yellow. The ribonucleosides that define the putative antibiotic binding site recognition site are represented by their colored Connolly surface based on the local electrostatic potential (in red the negative potential regions, in blue those with positive potential, in white those with potential close to zero, kcal/mol). Dalfopristin (D) makes interactions with several residues of the binding site. Hydrogen bonding interactions are represented by dashed lines, one involving the carbonyl oxygen at position 7 of the dalfopristin moiety and the guanine 2724 of the ribosome structure (*left*), and one involving the hydroxyl oxygen at position 14 of the dalfopristin moiety and the guanine 2992 of the ribosome structure (*right*). The interaction energy ($IE_{complex}$) based on the force field potential (AMBER10) is calculated in -110 kcal/mol ($IE_{complex} = Ep_{complex} – Ep_{RNA} – Ep_{lig}$).

By introducing new substituent groups in suitable positions on D scaffold, it is possible to increase the number and the strength of the interactions between D and the mitoribosome, resulting in more stable D derivative-mitoribosome complexes. The selection of the most promising D derivatives will therefore be based on the energy values of the corresponding derivative-mitoribosome complexes and on the interactions involved. In addition, state-of-the-art open sources algorithms, such as StarDrop, will be used to evaluate the drug-likeness of the identified derivatives and to predict *in silico* their ADME (adsorption, distribution, metabolism, excretion) profiles.

6.3 DEFINING DALFOPRISTIN DERIVATIVES

Dalfopristin (D) and virginiamycin M1(VM1) are polyunsaturated 23-membered rings group A streptogramins (Barrière et al., 1998). VM1 is produced by different *Streptomyces* strains, such as *Streptomyces pristinaespiralis* and *Streptomyces virginiae*, whereas D is produced by semisynthesis starting from VM1 (Bonfiglio and Furneri, 2001). A fully synthetic route to VM1 consisting of 8 linear steps and presenting a final yield of 15% has been published for the first time only very recently (Li and Seiple, 2017).

In order to produce a first series of derivatives, we decided to adopt a semisynthetic approach starting from D. There are several positions on D scaffold where it is possible to introduce novel chemical moieties by semisynthesis (**Figure 6.3**) and many D derivatives have already been synthesized in the light of developing more potent antibiotic derivatives.

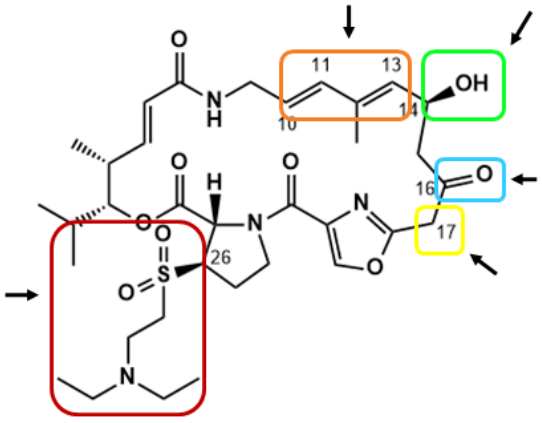

Figure 6.3 Possible sites of structural modification on dalfopristin scaffold.

By observing the molecule arrangement in the mitoribosome binding site, we noticed that the replacement of the ketone group in position C16 with a small substituent, such as a halogen atom, could increase the interaction with the mitoribosome.

In addition, we noted that the conjugated diene that is present in the D scaffold (C10-13) assumes a *cisoid* conformation upon binding. This observation led us to investigate the possibility to perform a Diels-Alder reaction on this position. Diels-Alder adducts of D have not been previously described, hence we decided to start our "derivative semisynthesis" by generating a series of Diels-Alder adducts ("Diels-Alder series").

6.4. SEMISYNTHESIS OF A FIRST DALFOPRISTIN DIELS ALDER ADDUCT

The amount of D necessary to perform semisynthetic chemistry is not easily and cost-effective accessible, e.g. 1 mg of the molecule costs 280 Euros from Santa Cruz Biotechnology. Therefore, we decided to buy the commercially available Q/D combination (Synercid®) and to separate D by liquid chromatography from the drug mixture. After trying different solvent combinations, I found that dichloromethane (DCM) and ethanol (EtOH) in a 8:2 v/v ratio had the highest separatory power on silica gel as stationary phase (Retention factor, Rf_D = 0.86, Rf_Q = 0.16) . Next, I used this solvent mixture as eluent to separate D and Q by a preparative layer chromatography (PLC) and obtained pure D, with a recovery yield of 85%. Dalfopristin identity was confirmed by nuclear magnetic resonance spectroscopy (NMR) (**Figure 6.4**) and electrospray mass spectrometry (ESI-MS) analyses (*m/z* = 692 $[M+H]^+$).

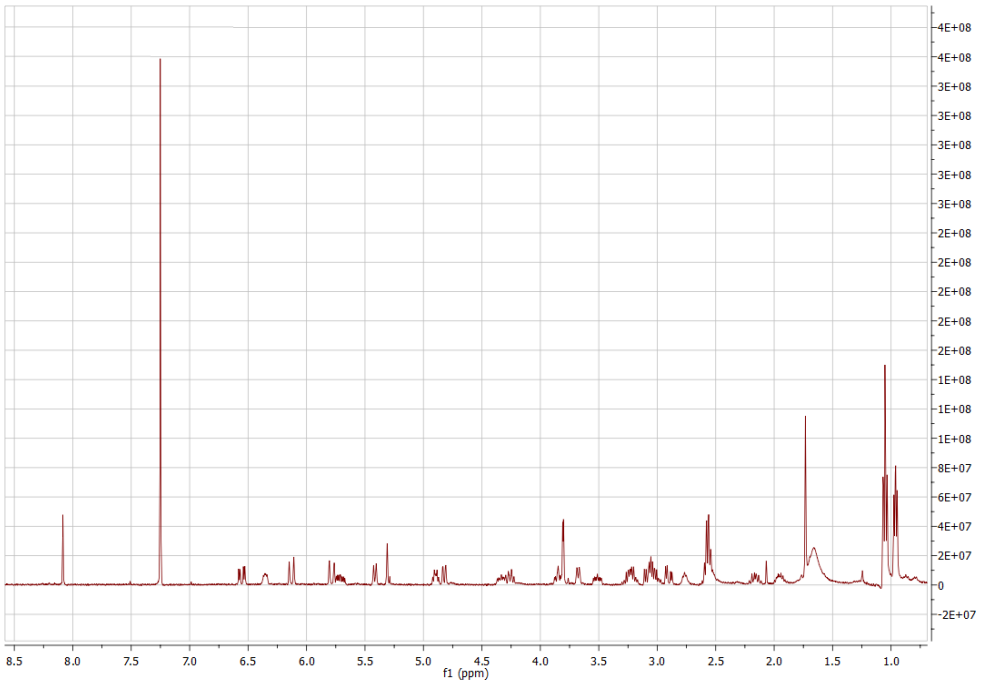

Figure 6.4 ^{1}H NMR ($CDCl_3$, 400MHz) spectrum of dalfopristin (D).

Next I performed a Diels-Alder reaction using maleic anhydride as dienophile. I evaluated several reaction conditions, including different reaction times and temperatures, microwave irradiation and the presence of $AlCl_3$ (Li et al., 2008). The best reaction condition (1.5 equivalents of maleic anhydride and 1 equivalent of $AlCl_3$ in DCM 3h at -35°C followed by reflux for 12h) (**Scheme 6.1**) allowed to obtain a first D derivative (**1**) which I further purified by PLC using DCM:EtOH = 8.2 (v/v) as eluent. ^{1}HNMR (**Figure 6.5a**) and ESI-MS spectra (*m/z* = 789 $[M+H]^+$, and *m/z* = 787 $[M-H]^-$) (**Figure 6.5b**) are in agreement with the predicted structure. We are currently fully characterizing the structure of the obtained compound by 2D heterocorrelated NMR experiments.

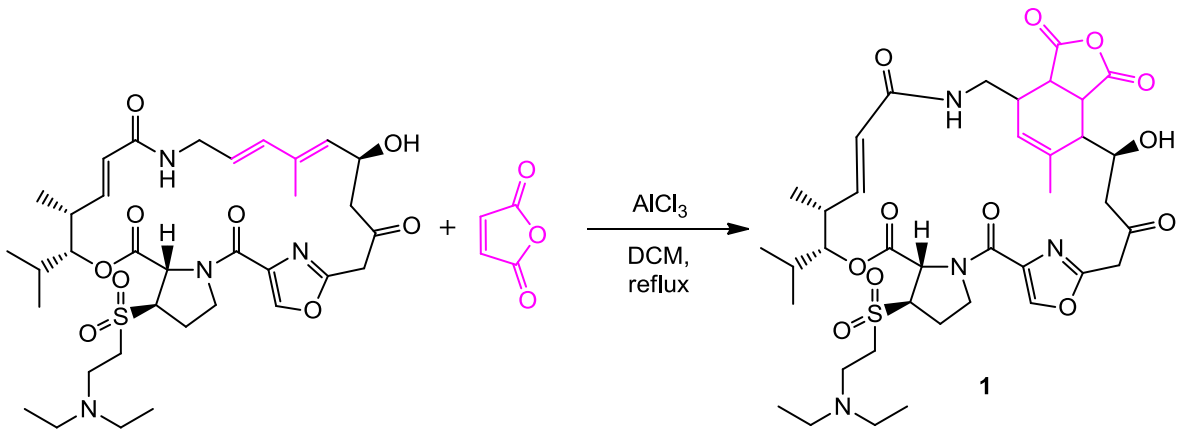

Scheme 6.1 Reaction conditions to produce 1. Dalfopristin was reacted with 1.5 equivalents of maleic anhydride and 1 equivalent of $AlCl_3$ in DCM 3h at -35°C followed by reflux for 12h. The parts of the molecules reacting together are highlighted in pink.

a

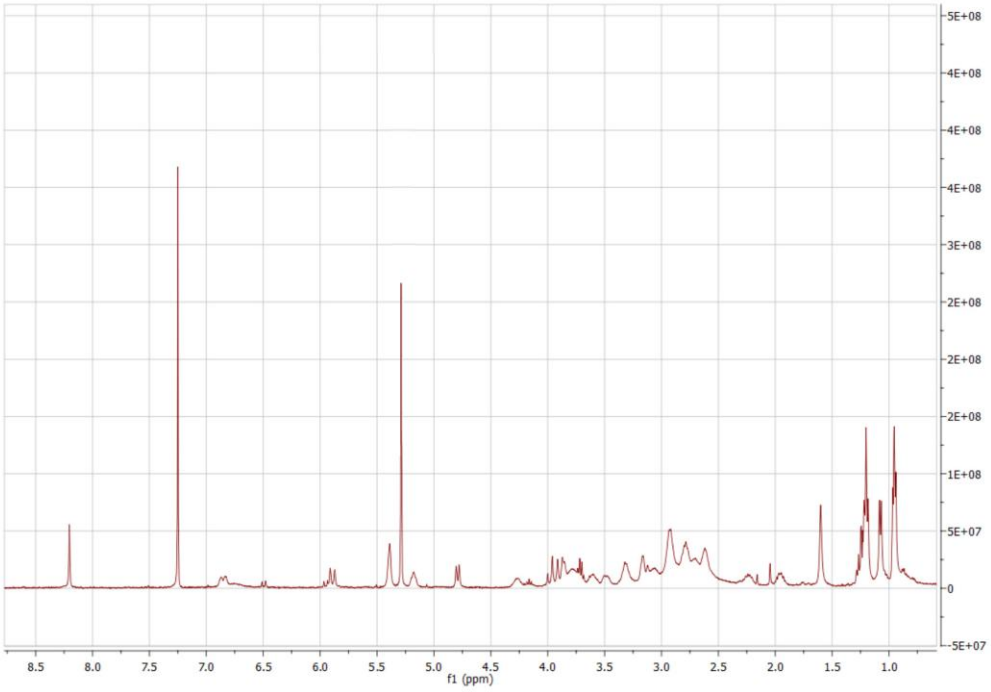

b

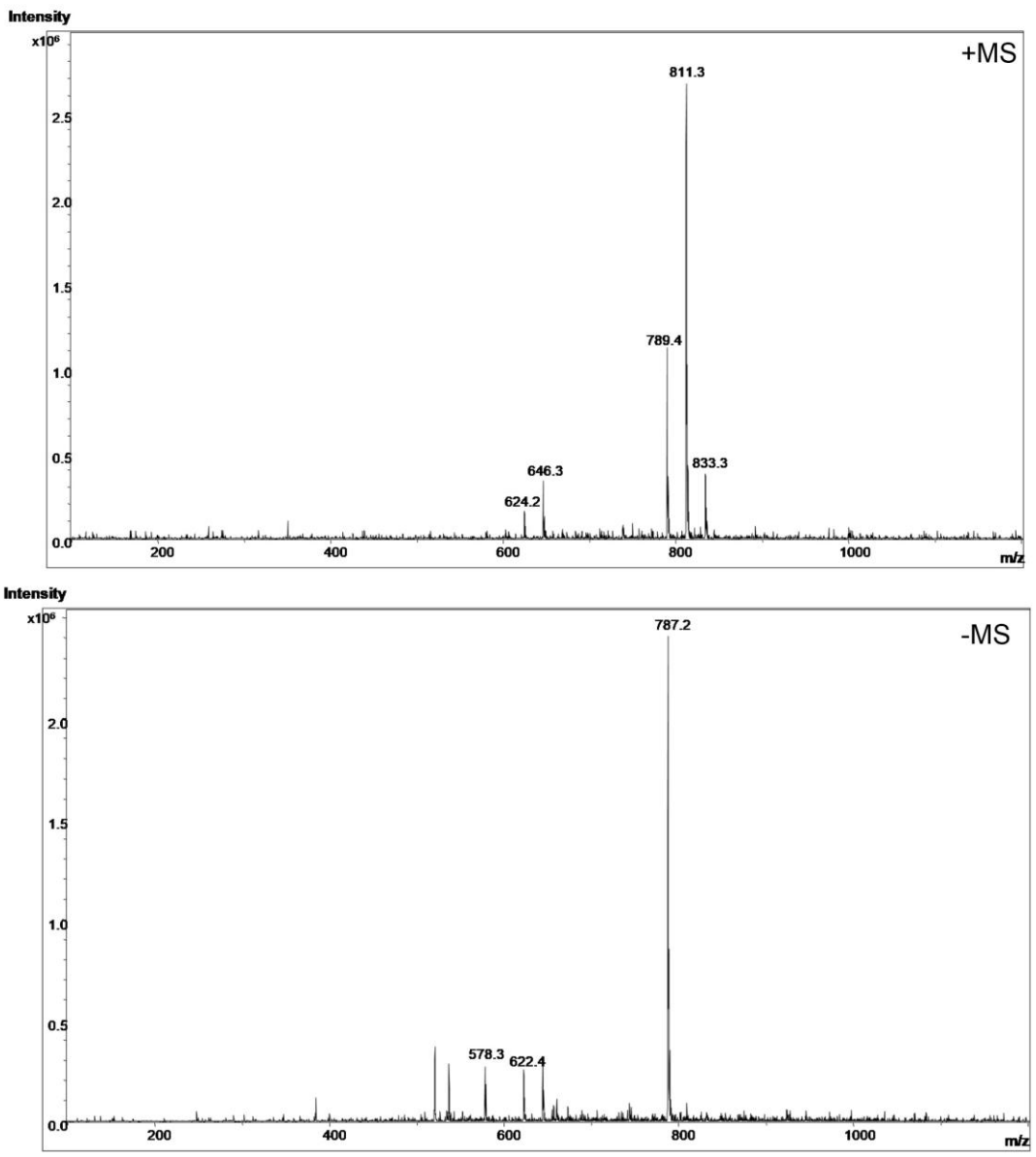

Figure 6.5 Maleic anhydride Diels-Alder adduct (1) characterization. a. ^{1}H NMR ($CDCl_3$, 400MHz) spectrum. **b.** ESI-MS spectra, showing the signals at *m/z* 811 $[M+Na]^+$ and *m/z* 789 $[M+H]^+$ in positive ion mode, and *m/z* 787 $[M-H]^-$ in negative ion mode.

Further high-performance liquid chromatography (HPLC) analysis will allow to define whether the obtained product is a single isomer or not. The stereochemistry of the obtained maleic anhydride Diels Alder adduct represents a critical point and extensive NMR experiments could help in its definition. Additional docking calculation considering the different isomeric forms could determine if the isomer(s) we obtained is/are the one(s) with the strongest interaction capability.

7. FUTURE PERSPECTIVES

In the light of the successful result obtained by performing the Diels-Alder reaction using maleic anhydride as dienophile, we plan to produce more derivatives belonging to the "Diels-Alder series" using 1,4 benzoquinone and maleimide as dienophiles, whose structures are reported in **Figure 7.1**. Contrarily to the maleic anhydride adduct that presents a H-bond acceptor (O), the maleimide adduct presents a H-bond donor group (NH) pointing toward the pocket of the binding site, which confers the ability to interact with H-bond acceptor residues. Diels-Alder derivatives of dalfopristin (D) have not been previously described, and therefore represent novel molecules whose biological activity is worth of further investigation.

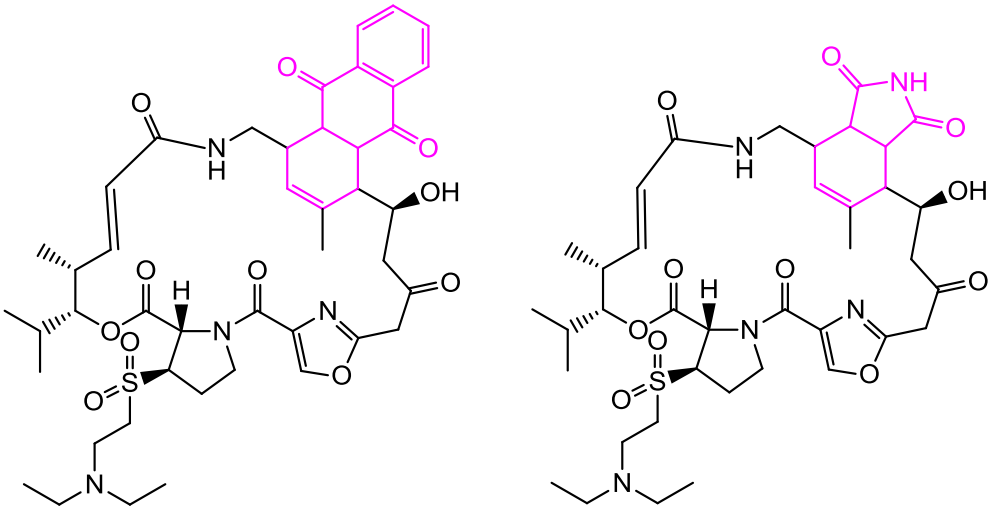

Figure 7.1 Diels-Alder derivatives of dalfopristin. 1,4 benzoquinone-Diels-Alder derivative (*left*) and maleimide-Diels-Alder derivative (*right*). The new groups introduced in the scaffold of dalfopristin are highlighted in pink.

Next, we will move toward the exploration of the positions on the D scaffold where it is possible to introduce new chemical moieties. These positions are represented by C14, C16 and C26, as depicted in **Figure 7.2**.

As pointed out by docking calculation, the binding site pocket present around the hydroxyl group in position C14 could accommodate small substituents, possibly able to act as H bonds donors, such as NH_2, NHOH, $NHNH_2$. In addition, we could also try to functionalize the hydroxyl group to small carbanilates (-$OCONH_2$, -OCONHMe) as reported in Lam *et al.*, 1993 (**Figure 7.2**).

The replacement of the ketone group (C=O) in position C16 with a small substituent, such as a halogen atom (**Figure 7.2**), could increase the interaction with the mitoribosome as predicted by docking calculation. The R configuration at this position has been reported to possess a greater biological activity compared to the S configuration (Bacque et al., 2005), therefore we will focus on producing R isomers.

Finally, the position in C26 has been largely studied from a chemical point of view, because it allows to introduce side chains able to increase the water solubility of streptogramin A molecules. The diethylaminoethylsulfonyl chain present on the dalfopristin scaffold is known to be easily hydrolyzed at pH 7.4 (Noeske et al., 2014). Starting from virginiamycin M1 and exploiting a Michael addition reaction, we will add several N-alkyl or S-alkyl chemical moieties in position C26. The "alkyl" chain $(CH_2)_n$ will present a variable length (with n=2-4) and will end with a tertiary amine, which could also be a cyclic amine, such as a pyrrolidine, a piperazine or a morpholine. The presence of an amino group offers the possibility of obtaining conjugates salts, further increasing the compound's water solubility.

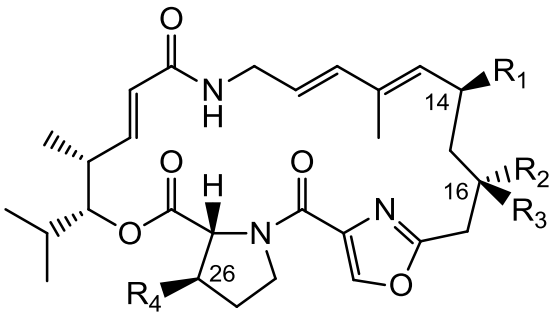

Figure 7.2 Derivatives of dalfopristin in C14, C16, C26 positions. R_1 = OH, NH_2, NHOH, $NHNH_2$, $OCONH_2$, OCONHMe. R_2 = H, R_3 =OH, NH_2, F, Cl, I, Br, CN, SCN, NCS, N_3, CF_3. R_2 =R_3 = O. R_4 = N-Alkyl, S-alkyl.

Most if not all the derivatives which are obtainable introducing chemical moieties in C14, C16 and C26 positions have been already reported, therefore their chemical synthesis should be easily performed. Even if these molecules are not completely new, their activity in the context of GBM, and more in general in the context of cancer, have never been evaluated before. Moreover, considering that the modification introduced would increase the affinity for the mitoribosome, these derivatives are endowed with a greater therapeutic potential compared to dalfopristin.

The choice of the derivatives to be synthesized will be guided both by docking calculation, which will allow to select the most promising compounds based on the interactions with the binding site, and by predicting *in silico* their ADME properties and the BBB penetration parameters.
Each newly synthesized derivative will be fully characterized and its chemical purity will be assessed by HPLC analysis.

The synthesized derivatives (30-40 molecules) will be tested *in vitro* on COMI and VIPI cells for their ability to inhibit cellular growth using the Hoechst 33342-PI assay previously described in the Results chapter. The derivatives with the strongest effect on cell growth (~10 molecules) will be then evaluated for their capability to cross the BBB *in vitro*, using a BBB *in vitro* model, such as BBB-like endothelial monolayers obtained by differentiation of iPSCs (Lauschke et al., 2017).
Finally, the compounds endowed with the greatest potential to cross the BBB (3 molecules) will be tested *in vivo* in comparison to dalfopristin for their ability to reduce tumor cells invasion in a patient derived-GSCs xenograft mouse model as described in the Results chapter.

8. EXPERIMENTAL PROCEDURES

8.1 CELL CULTURE

Human glioblastoma stem cell lines COMI and VIPI were kind gifts from Antonio Daga (Azienda Ospedaliera Universitaria San Martino di Genova, Italy), and 030616 from Rossella Galli (San Raffaele Hospital, Milan, Italy). COMI, VIPI and 030616 were cultured in DMEM/F-12 and Neurobasal media (Thermo Fisher Scientific, 1:1 ratio), supplemented with GlutaMAX (2 mM; Thermo Fisher Scientific), B27 supplement (1%; Thermo Fisher Scientific), Penicillin G (100 U/mL; Sigma Aldrich), recombinant human fibroblast growth factor-2 (bFGF) (10 ng/mL; R&D Systems), recombinant human epidermal growth factor (EGF) (20 ng/mL; R&D Systems) and heparin (2 µg/mL; Sigma Aldrich) at 37°C, 5% CO_2. Cells were grown either as spheres in suspension or as adherent cultures on laminin-coated flasks where they maintain intact self-renewal capacity (Pollard et al., 2009).
Human glioblastoma stem cell lines GB6, GB7, GB8, G144, G166 and the human fetal neural stem cell line CB660 were kind gifts from Luciano Conti (CIBIO, University of Trento, Italy) and were cultured as adherent cultures on laminin-coated flasks in Euromed-N media (Euroclone), supplemented with GlutaMax (2 mM), B27 supplement (2%), N2 (1%; Thermo Fisher Scientific), Penicillin G (100 U/mL), recombinant human fibroblast growth factor-2 (bFGF) (20 ng/mL), and recombinant human epidermal growth factor (EGF) (20 ng/mL) at 37°C 5% CO_2. Culture flasks were coated with laminin (10 µg/mL, Thermo Fisher Scientific, cat. 23017015) and incubated for 3h at 37°C or overnight at 4°C prior to use.
Human lung fibroblasts, MRC5, were cultured in EMEM media (Thermo Fisher Scientific), supplemented with 10% FBS, GlutaMAX (2 mM; Thermo Fisher Scientific) and Penicillin G (100 U/mL) at 37°C, 5% CO_2.

For GSCs differentiation, cells were grown on laminin-coated plates in the above media without growth factors and with the addition of 10% FBS (Thermo Fisher Scientific) for 10-14 days. For astrocyte differentiation, CB660 cells were grown on laminin-coated plates in the above media without growth factors and with the addition of 5% FBS for 3 weeks.

For hypoxia and anoxia experiments, cells after treatment were grown in a hypoxic chamber (Invivo$_2$ 200, Baker Ruskinn, Hypoxic, 1% O_2) or in anoxic conditions using an anaerobic jar (2.5 L, Mitsubishi Gas Chemical America) and an anaerobic atmosphere generator bag (Genbox, cat. 96124).

8.2 HIGH CONTENT SCREENING AND SCREENING ANALYSIS

A custom-made library was created using compounds available from the Selleck Translation Inhibitors and MS Discovery libraries, and additional compounds acquired from other companies (**Table 3.2,** at pages 34-36). All compounds were solubilized in dimethyl sulfoxide (DMSO, Sigma Aldrich) and stored frozen prior to use. COMI and VIPI cells were plated in 96-well microtiter plates in 150 µL of media at plating densities of 6,000 and 4,500 cells/well, respectively, and incubated for 24h prior to drug treatment. The drugs were added to a final concentration of 100 µM and the plates were incubated for 24h at 37°C. Each treatment was performed in a technical triplicate. The positive control wells were treated with FCCP, rotenone and oligomycin A at 100 µM for 24h or with FCCP (Cayman Chemical, cat.15218) at 100 µM for 30min at 37°C. Next, cells were stained with 200 nM MitoTracker Orange (Thermo Fisher Scientific, cat. M7510) and incubated for 30min at 37°C. Subsequently, cells were fixed by direct addition of paraformaldehyde solution to a final concentration of 4% v/v and incubation for 15min at room temperature, followed by a wash with 200 µL of PBS using. The cells were then stained with 5 µM DRAQ5 (Cell Signaling, cat. 4084) for 20min at room temperature protected from light. Drug dilution and addition was performed using Tecan Evo 200 liquid handler, whereas fixing, PBS washing and dyes dispensation were performed using BioTek EL406 washer dispenser. The plates were read using the Operetta-High Content Imaging System (Perkin Elmer). Compound precipitation was visually assessed and interfering compounds were excluded from the analysis.

In order to perform phenotypic profiling of the compound-induced toxicity effects, the image data were visualized and analyzed using the Harmony Software. Six informative features describing cellular compactness and intracellular fluorescence distribution were extracted to describe cellular or mitochondrial toxicity phenotypes (**Table 3.3**, at page 39).
The data were plate-wise normalized by computing the compound percentage of the vehicle control treatment (DMSO) for each feature. The informative content of a feature was assessed by testing whether the feature values for the positive controls were significantly different from the vehicle treatment (t-test, FDR < 0.05). For each library compound we assessed the size of the effect induced on each feature. A compound was defined as a hit for a given feature when the feature deviated from the median value of all compounds by a distance larger than 1.5 times the median absolute deviation. Individual compounds were scored by the number of affected features. When a feature was affected by a compound, it accounted for one over the number of informative features (in this case ⅙, since the number of considered features is 6). Therefore, when all the features were affected, the

maximal attainable score for a given compound was one (or 100%). We next assigned a percentage score to each class of compounds by calculating the average of the scores attained by all the compounds included in each class.

8.3 VIABILITY ASSAYS

For the evaluation of the effect of OXPHOS and glycolysis inhibitors on GSCs viability, cells were plated in a 96 laminin-coated well plate (2,500 cells/well of COMI and VIPI) and treated the following day with rotenone (1 μM, Sigma Aldrich, cat. R8875), Oligomycin (1 μM, Sigma Aldrich, cat. O4876), Antimycin A (1 μM, Sigma Aldrich, cat. A8674), 2-deoxyglucose (2-DG, 250 μM, Sigma Aldrich, D8375) and dichloroacetic acid (DCA, 5 mM, Sigma Aldrich, cat. 347795) for 72h. Each treatment was performed in technical triplicate.

For the evaluation of the effect of streptogramins, including quinupristin/dalfopristin (Q/D), tetracyclines and pleuromutilins on GSCs viability, cells were seeded into 96-well laminin-coated microtiter plates in 150 μL of media at plating densities ranging from 3,500-6,000 cells/well. The plates were incubated for 24h prior to drug treatment. Serial drug dilutions were prepared in PBS to provide a total of seven drug concentrations plus control. 10 μL of these dilutions were added to each well, and the plates were incubated for additional 48h. Each treatment was performed in technical quadruplicate. The following compounds were tested: Dalfopristin (D) (Santa Cruz, cat. sc-362728), Quinupristin (Q) (Bioaustralis, cat. BIA-Q1354), Quinupristin-dalfopristin mesylate complex (Q/D) (Santa Cruz, cat. sc-391726), Virginiamycin M1 (Sigma Aldrich, cat. V2753), Virginiamycin B (Santa Cruz, cat. sc-362038), Virginiamycin S1 (Apollo Scientific, cat. BIV1004), Griseoviridin (Apollo Scientific, cat. BIBR1137), Viridogrisein (Apollo Scientific, cat. BIBR1132), Tetracycline (Sigma Aldrich, cat. 87128-25G), Methacycline HCl (Sigma Aldrich, cat.37906-100MG-R), Oxytetracycline (Sigma Aldrich, cat PHR1537-1G), Doxycycline HCl (Sigma Aldrich, cat. D3447-500MG), Demeclocycline HCl hydrate (Sigma Aldrich, cat. 46161-100MG), Meclocycline Sulfosalicylate (Sigma Aldrich, cat. M1388-500 MG), Minocycline HCl (Santa Cruz, cat. sc-203339), Pipacycline (Santa Cruz, cat. sc-391690), Tigecycline (Santa Cruz, cat. sc-394197), Valnemulin (MicroSource Discovery library) and Tiamulin (Sigma Aldrich, cat., 34044).

After the drug treatments, the cells were stained with Hoechst 33342 (1μg/mL; Thermo Fisher Scientific, cat. H1399) and propidium iodide (PI, 1μg/mL; Sigma Aldrich, cat. P4170) and incubated for 20min shaking in the dark. The plates were then read using Operetta-High Content Imaging System (Perkin Elmer) and analysed using the Harmony Software. The number of viable cells was calculated by subtracting PI positive cells from the total

number of cells estimated by Hoechst 33342 staining and normalized on the non-treated control.

For cytotoxicity analysis on GSCs grown as neurospheres, the cells were mechanically dissociated and plated at a density of $2x10^4$ cells/mL in a 96-well plate, in triplicate. Q/D was added 24 hours after cell plating. ATP levels were measured using the CellTiter-Glo® Luminescent Cell Viability Assay (Promega, cat. G7570) as per the manufacturer's instructions after 48h and 72h of treatment. Percentage viability was calculated upon normalization on the non treated control. This experiment was performed at the Istituto Superiore di Sanità by Lucia Ricci-Vitiani's group.

Dose-response curves were plotted and growth inhibition 50 (GI_{50}) values calculated using the GraphPad Prism software.

For cytotoxicity analysis on COMI cells grown as neurospheres, the cells were mechanically dissociated and ten cells/well were plated in Ultra-Low attachment round bottom 96 well plates (Costar) and treated with desired Q/D concentrations. The cells were centrifuged at 300g for 30sec, followed by the first acquisition using Operetta-High Content Imaging System (Perkin Elmer). The images were subsequently acquired over the course of 9-10 days. The area of the spheres formed was assessed using the Harmony Software.

8.4 NEUROSPHERE FORMATION ASSAY

COMI cells grown in suspension were plated at a density of 50,000 cells/mL and treated with Q/D for 72h. The spheres were then dissociated and the cells were counted and plated at a density of 10 or 100 cells/well in a 96 well plate without the drug. After 10 days, the spheres formed were stained with 1 µM Calcein AM (Thermo Fisher Scientific, cat. C3100MP; for 20 min at 37°C), imaged using Operetta-High Content Imaging System (Perkin Elmer) and analyzed using Harmony Software. Only spheres greater than 100µm were quantified. The experiment was performed in a biological triplicate, with 20 technical replicates each.

8.5 MITOCHONDRIAL AND CYTOSOLIC PROTEIN SYNTHESIS ASSAY

Cells were plated 24 h prior to treatment (180,000 cells/well of COMI cells in a 6 well plate) and incubated with Q/D, D or Q for further 24h prior to [^{35}S]-methionine labeling. To assay for mitochondrial protein synthesis, growth medium was removed and cells were washed

twice with methionine/cysteine-free DMEM medium, followed by an incubation in methionine/cysteine-free DMEM medium containing 96 µg/mL Cysteine, 1% B27 supplement, 1% GlutaMax; 1% Sodium Pyruvate, 10 ng/mL bFGF, 20 ng/mL EGF, 2 µg/mL heparin and 80 µg/mL emetine (Sigma Aldrich, cat. E2375) for 15 min at 37°C. Subsequently, [^{35}S]-methionine (Perkin Elmer, cat. NEG709A005MC) was added to a final concentration of 166.6 µCi/mL and the labeling was performed for 20 min at 37°C. The cells were then detached and pelleted at 4,000 rpm for 5min. The pellet was washed three times with 1 mL of PBS. Cell pellets were resuspended in protein lysis buffer containing protease inhibitors and 1.25 U/µL benzonase. Protein concentrations were measured with PierceTM BCA Protein Assay Kit (Thermo Fisher Scientific, cat. 23227) and equal amount of protein samples were separated on SDS-PAGE gels (NuPAGETM 12% Bis-Tris Protein Gels, Thermo Fisher Scientific, cat. NP0343BOX). The labelled proteins were visualized and quantified using a PhosphorImager system and ImageQuant software (Molecular Dynamics, GE Healthcare). To assay for cytosolic translation, the above procedure was used without the addition of emetine.

8.6 IMMUNOBLOTTING

Total cell lysates were prepared from cells. Briefly, cells were washed with PBS and resuspended in lysis buffer (50 mM Tris-HCl pH 7.4, 150 mM NaCl, 1 mM EDTA, 0.25% NP-40, 0.1% Triton X-100, 0.1% SDS) supplemented with protease inhibitors. Protein concentrations were quantified with Pierce^{TM} BCA Protein Assay Kit (Thermo Fisher Scientific, cat. 23227). Equal amounts of protein were separated on SDS-PAGE and transferred to nitrocellulose or PVDF (for anti-LC3 antibody only) membrane. Membranes were probed with anti-MTCO1 (COX1, Abcam, cat. ab14705), anti-COX4 (Cell Signaling, cat. 4850), anti-β-tubulin (Santa Cruz, cat. sc-53140), anti-LC3 (Cell Signaling, cat. 3868S), and secondary HRP-conjugated antibodies (Santa Cruz Biotechnology). Detection was performed using Amersham ECL Prime or Select Western Blotting Detection Reagent (GE Healthcare Life Sciences) and ChemiDoc Imaging System (Bio-Rad). Data were analyzed using ImageLab software.

8.7 IMMUNOFLUORESCENCE

The cells were fixed either with paraformaldehyde solution (4% v/v final, 15 min incubation at room temperature) or with 100% ice-cold methanol (5 min incubation at room temperature, only for LC3B IF), followed by two washes with PBS. The cells were then

permeabilized with 0.3% Triton X-100 - 3% BSA in PBS for 45 min at room temperature. The primary and secondary antibodies were diluted in 3% BSA-PBS solution. The incubation with the primary antibody was carried out at 4°C overnight, whereas the incubation with the secondary antibody was performed for 1h at room temperature. Cell morphology was determined by staining with HCS CellMask™ Deep Red Stain (Thermo fisher Scientific, cat. H32721, 1:2000, 20 min, room temperature). The plates were then read either using Operetta-High Content Imaging System (Perkin Elmer) and analyzed by the Harmony Software or using the Leica TCS SP5 confocal microscope and processed by imaging softwares ImageJ (version v1.51w) and Photoshop. For the latter, images were acquired on a Leica TCS SP5 confocal microscope with a 63x oil immersion objective, 2x zoom, 1024x1024 resolution, 200Hz speed, lasers Argon 488 nm and Diode laser 633 nm, step 0.89µm. Z-stack images were acquired and LC3 puncta quantification was performed on image stacks of region of interests containing single cells, using the "3D Maxima finder" plugins of ImageJ. Both size and intensity threshold constraints were applied to the quantification.

8.8 RNA EXTRACTION, REVERSE TRANSCRIPTION AND QUANTITATIVE REAL-TIME POLYMERASE CHAIN REACTION

Total RNA was extracted using QIAzol reagent (QIAGEN) according to the manufacturer's instructions. Reverse transcription was performed on 500 ng of RNA using iScript Reverse Transcription Supermix (BioRad, cat.no.170-8891, unique blend of oligo(dT) and random hexamer primers) on C1000 Thermal Cycler (BioRad). The total cDNA obtained was diluted 1:100, and quantitative real-time PCR was performed on 2 µL of sample using 2x qPCR SyGreen Mix Separate ROX (PCR Biosystems, cat.no. PB20.14-05) following the manufacturer's instructions on CFX384 Real-Time System (BioRad). All assays were performed in triplicate in 4-5 independent experiments. Data was analysed using CFX Manager software (BioRad). Relative expression values of each target gene were normalized to GAPDH and 18S RNA level. The following primers were used at 500 nM concentration:

COX1: 5'- CTATACCTATTATTCGGCGCATGA-3' and 5'-CAGCTCGGCTCGAATAAGGA -3',
COX4: 5'-GCCATGTTCTTCATCGGTTTC-3' and 5'-GGCCGTACACATAGTGCTTCTG-3',
18S: 5'-GGACATCTAAGGGCATCACA-3' and 5'-AGGAATTGACGGAAGGGCAC-3',
GAPDH: 5'-CAACGAATTTGGCTACAGCA-3' and 5'-AGGGGTCTACATGGCAACTG-3'.

8.9 BN-PAGE AND IN GEL COMPLEX ACTIVITY ASSAY

Cells were plated in two T75 flasks (700 000 cells/flask) and treated with Q/D after 24h for additional 48h, 72h and 96h. Mitochondria were isolated in the following manner: cells were detached, pelleted and resuspended in 750 µL of MIB+BSA buffer (0.32 M sucrose, 1 mM EGTA pH 8, 20 mM Tris-HCl, pH 7.2, 0.1% fatty acid-free BSA). The cells were homogenized using Potter-Elvehjem homogeniser (60 strokes) and centrifuged at 1,000 g for 5min at 4°C. The supernatant was collected and the pellet resuspended in MIB+BSA, rehomogenised (20 strokes) and centrifuged again. The supernatant was collected and pooled with the first one, then centrifuged at 12,000g for 10 min at 4°C to pellet the mitochondria. The pellet of mitochondria was subsequently washed once with MIB+BSA, once with MIB, resuspended in 100 µL of ACNA buffer (1.5 M aminocaproic acid (Sigma Aldrich, cat. A2504), 50 mM BisTris, pH 7) and quantified using Qubit™ Protein Assay Kit (Thermo Fisher Scientific, cat. Q33212). Digitonin (Sigma Aldrich, cat. D5628-1G) was added to a final concentration of 1% w/v, the samples were vortexed and incubated on ice for 20 min, followed by a centrifugation at 14,000g for 30min at 4°C. The supernatant was mixed with the loading buffer, and 50 µg of protein was separated on Blue Native PAGE gels (NativePAGE^{TM} 3-12% BisTris Protein Gels, Thermo Fisher Scientific, cat. BN1001BOX). The conditions of incubation for the complexes have been adapted from (Nijtmans et al., 2002). Briefly, the gels were incubated overnight at room temperature with the respective complex substrates: Complex I: 2 mM Tris HCl, pH 7.4; 0.1 mg/mL NADH (Sigma Aldrich, cat. N8129-50MG); 2.5 mg/mL iodonitrotetrazolium chloride (Sigma Aldrich, cat. I8377-1G); Complex II: 4.5 mM EDTA, 0.2 mM phenazine methosulfate (Sigma Aldrich, cat. P9625-500MG), 84 mM succinic acid (Sigma Aldrich, cat. S2378-100G) and 0.5 mg/mL iodonitrotetrazolium chloride (Sigma Aldrich, cat. I8377-1G); Complex IV: 0.5 mg/mL 3.3'-diamidobenzidine tetrahydrochloride (DAB) (Sigma Aldrich, cat. D5637-1G), 50mM phosphate buffer pH 7.4, 1 mg/mL cytochrome *c* (Sigma Aldrich, cat. C2506-1G), 0.2 M sucrose, 20 µg/mL (1 nM) catalase (Sigma Aldrich, cat. C9322-1G), Complex V: 3.76 mg/mL glycine, 5 mM $MgCl_2$; Triton X-100, 0.5 mg/mL lead nitrate (Sigma Aldrich, cat. 203580), 8 mM ATP (Sigma Aldrich, cat. A7699-5G), pH 8.4.

8.10 IMMUNOBLOTTING AFTER BN-PAGE

Proteins separated on Blue Native PAGE gels (NativePAGE^{TM} 3-12% BisTris Protein Gels, Thermo Fisher Scientific, cat. BN1001BOX) were transferred to PVDF membrane (25 V, 4°C, O/N, wet-transfer, transfer buffer with 20% MeOH and 2 mL of 10% SDS in 1L).

Membranes were stripped to remove the blue-staining (Restore™ PLUS Western Blot Stripping Buffer, Thermo Fisher Scientific, cat. 46430, 3 min) and probed with anti-OXPHOS complex I (39kDa subunit; clone 20C11, Thermo Fisher Scientific, cat. A21344), anti-SDHA complex II (2E3GC12FB2AE2, Abcam, cat. ab14715), anti-OxPhos complex III (core 1 subunit; clone 16D10, Thermo Fisher Scientific, cat. A21362), anti-OxPhos complex IV (subunit 1; clone 1D6E1A8, Invitrogen cat. 459600), anti-ATP5A complex V (15H4C4, Abcam, cat. ab14748) and Amersham ECL secondary HRP-conjugated antibodies (GE Healthcare). Proteins detection was performed using Clarity™ Western ECL Substrate Detection Reagent (Biorad, cat. 1705061).

8.11 HIGH-RESOLUTION RESPIROMETRY ASSAY

High-resolution respirometry was performed using a 2 mL chamber OROBOROS Oxygraph-2k (Oroboros Instruments) at 37°C. Respiration rates were calculated as the negative time derivative of oxygen concentration measured in the closed respirometer and expressed per number of viable cells and corrected by residual oxygen consumption (ROX, after antimycin A addition). The amplified signal was recorded on a computer with online display of the calibrated oxygen concentration and oxygen flux (DatLab software for data acquisition and analysis; Oroboros Instruments). Cells were plated 24h prior to treatment and incubated with Q/D for further 48h. The cells were then detached and 1,000,000 cells were injected into each chamber. Oxygen consumption was evaluated for cellular ROUTINE respiration, and then cells were permeabilized with digitonin 4.1 uM (Fluka, cat. 37008) in MiR05 medium (10 mM KH_2PO_4, 60 mM lactobionic acid (Sigma Aldrich, cat. 153516), 20 mM HEPES, 3 mM $MgCl_2$, 0.5 mM EGTA, 20 mM taurine (Sigma Aldrich, cat. T0625), 110 mM D-sucrose and 1 mg/mL BSA fatty acid free). Complex I activity was measured after malate (2 mM, Sigma Aldrich, cat. M1000), glutamate (10 mM, Sigma Aldrich, cat. G1626) and ADP (5 mM, Calbiochem, cat. 117105) injection, and complex I and II activity after additional succinate (10 mM, Sigma Aldrich, cat. S2378) injection. The ETS capacity (maximum uncoupled respiration) was induced by stepwise titration of carbonyl cyanide p-(trifluoromethoxy) phenylhydrazone (FCCP, Sigma Aldrich, cat. C2920) (typically 3–4 steps, 1 ul each of 1 mM FCCP). Complex II activity was measured after the addition of rotenone (0.5 uM, Sigma Aldrich, cat. R8875). Residual respiration (ROX) was measured after inhibition with antimycin A (2.5 µM, Sigma Aldrich, cat. A8674).

8.12 LACTATE ASSAY

Cells were plated in a 96 well plate (4,000 cells/well of COMI and 3,500 cells/well of VIPI) and treated the following day with Q/D for 48h. Media was collected and the lactate production was measured using Glycolysis Cell-Based Assay Kit (Cayman Chemical, cat. 600450) according to the manufacturer's instructions. The cells were then fixed with 4% v/v paraformaldehyde for 15 min at room temperature and stained with Hoechst 33342 (1 µg/mL). The nuclei were quantified using Operetta-High Content Imaging System (Perkin Elmer) and analysed by the Harmony Software. The lactate production was normalized on the number of cells.

8.13 CRYO-ELECTRON MICROSCOPY DATA COLLECTION, IMAGE PROCESSING, MODEL BUILDING AND REFINEMENT

Cryo-EM experiments were performed by Alexey Amunts's group at SciLifeLab, Stockholm. Human mitoribosomes and grids were prepared as described previously (Amunts et al., 2015) with some modifications. Briefly, 2 liters of HEK293S TetR GnTi- cells lacking N-acetyl-glucosaminyltransferase I were grown to a final concentration of 4.2 x 10^6 cell/mL. Prior to cell collection and mitoribosome isolation, the cells were treated with 5 µM Q/D for 24h. Three µL of purified mitochondrial ribosomes at a concentration of 3.6 Abs at 280 nm was incubated for 30sec on glow-discharged holey carbon grids (Cu Quantifoil R2/2), onto which a home-made continuous carbon film had previously been deposited, prior to vitrification in a Vitrobot MKIV (3 second blot, 4 C, 100 % humidity). Images were collected on a 300 kV FEI Titan Krios electron microscope, a slit width of 20 eV on a GIF-Quantum energy filter. A Gatan K2-Summit detector was used in counting mode at a magnification of 130,000 (yielding a pixel size of 1.05 Å), and a dose rate of ~5.2 electrons per pixel per second. Exposures of 8ses (yielding a total dose of 38 eÅ-2) were dose-fractionated into 20 movie frames that were stacked into a single MRC stack using newstack. 4225 images were collected using EPU automatic data collection with defocus values ranging from 0.4 to 4.5 µm.

Collected micrographs were corrected for local-frame movement as well as dose filtered using UcsfDfCorr (Zheng et al., 2017). The contrast transfer function parameters were estimated using GCTF-0.5 (Zhang, 2015), for all other image processing steps RELION-2.1.b1 (Kimanius et al., 2016). 578,573 particles were picked using reference based picking, where bad particles were removed by particle sorting (546,701 particles retained) and

subjected to reference-free 2D class averaging, resulting in 387,428 particles for 3D classification. 4 classes containing 138,030 particles were pooled and subjected to 3D auto-refinement, yielding a map of the human mitochondrial ribosome. However, since there was some heterogeneity visible in the reconstruction, the particles were subjected to further fine angular classification and 100,000 particles were selected for another 3D auto-refinement step. Since Q/D is known to interact with the bacterial large subunit and in order to improve the quality of the map, masked focused-refinement was used to focus on the LSU. The resolution of the final reconstruction was 3.9 Å.

Reported resolutions are based on gold-standard refinement applying the 0.143-criterion on the FSC between reconstructed half-maps. The FSC was corrected for the effects of a soft mask on the using high-resolution noise substitution. All 3D refinements used a 70 Å low-pass filtered initial model, the first of which was a previous low resolution reconstruction of the human mitochondrial ribosome (EMDB-2876 (Amunts et al., 2015)). Before visualization, all density maps were corrected for the modulation transfer function of the detector, and then sharpened by applying a negative B-factor that was estimated using automated procedures (Rosenthal and Henderson, 2003).

The quality of the map allowed unambiguous model building with Coot (Emsley and Cowtan, 2004). Stereochemical refinement was performed using phenix.real_space_refine as implemented in the PHENIX suite (Adams et al., 2010). The final model was validated using MolProbity (Chen et al., 2010).

8.14 MITOCHONDRIAL MASS

Mitochondrial mass was assayed by staining the mitochondria with MitoTracker Orange (Thermo Fisher Scientific) or anti-COX4 antibody (Abcam) as described in the immunofluorescence section at pages 94-95. Concomitant staining with Hoechst 33342 (1µg/mL; Thermo Fisher Scientific, cat. H1399) and HCS CellMask™ Deep Red Stain (Thermo fisher Scientific, cat. H32721) was performed to visualize cell nuclei and define cytoplasmic region respectively. 10-15 images per well (3 wells each condition) were acquired using Operetta High Content Imaging System (Perkin Elmer) in widefield mode with a 20X objective. The focus plane was optimized for each fluorescence channel to obtain the best resolution and signal to noise ratio. Image analysis was performed using the Harmony Software (Perkin Elmer). Dedicated alghorithms were chosen to define cell regions and spots and the resulting analysis sequence was applied automatically on all images. A total of 2000-3000 cells per well were analysed and the number of mitochondria was estimated by counting the number of MitoTracker Orange or COX4 positive spots

present in the cytoplasmic region defined using HCS CellMask™ Deep Red Stain and expressed as square pixel (px^2) (number of spots/Area of cytoplasm).

8.15 CELL CYCLE ASSAY

Cells were plated 24h prior to treatment (120,000 cells/well of COMI cells in a 6 well plate) and incubated with Q/D for additional 48h. Cell cycle analysis was conducted using FACS (BD FACSCanto II) after staining with Click-IT EdU Flow Cytometry Assay kit (Thermo Fisher Scientific, cat.C10634) according to the manufacturer's instructions. The experiment was performed in a biological triplicate. Data were processed by BD FacsDIVA V8.0.1™ software.

8.16 APOPTOSIS ASSAYS

Apoptosis was assessed using FITC Annexin V Apoptosis Detection Kit I (BD Pharmingen, BD Biosciences, cat. 556547). Cells were plated 24h prior to treatment (270,000 cells/$6cm^2$ plate of COMI cells) and incubated with Q/D for further 48h. 200,000 cells were stained according to the manufacturer's instructions and analyzed using FACS (BD FACSCanto II). Data were processed by BD FacsDIVA V8.0.1™ software.

8.17 AUTOPHAGY ASSAYS

To assess for autophagic flux, cells were plated 24h prior to treatment and incubated with 6.5 μM Q/D for further 48h. In addition, for immunoblotting the cells were treated with 60 μM chloroquine for 24h (Sigma Aldrich, cat. C6628), 6.5 nM bafilomycin for 3h (Sigma Aldrich, cat. B1793) or 5 mM NH_4Cl for 3h (Sigma Aldrich, cat. A9434). Immunoblotting was performed as described in the Immunoblotting section, at page 94. LC3B-II was quantified by densitometric analysis (Image Lab 2.0.1 software, Biorad) and normalized on β-tubulin as a loading control. For immunofluorescence analysis, cells were plated 24h prior to treatment and incubated with 6.5 μM Q/D for further 48h. In addition, the cells were treated with 60 μM chloroquine, 6.5 nM bafilomycin or 10 mM NH_4Cl for 24h. Immunofluorescence for LC3 staining was carried out according to the procedure described in the Immunofluorescence section, at pages 94-95. Cell morphology was determined with staining with HCS CellMask™ Deep Red Stain (Thermo fisher Scientific, cat. H32721).

In order to evaluate the role of autophagy in the cytotoxic activity of Q/D, COMI cells were seeded into 96-well microtiter plates in 150 µL of media at plating densities of 4,000 cells/well. The plates were incubated for 24h prior to drug treatment. Cells were pretreated with chloroquine (5,10 and 20 µM) for 3h and then treated with 6.5 µM of Q/D for further 48h. The cells were stained with Hoechst 33342 (1µg/mL; Thermo Fisher Scientific, cat. H1399) and propidium iodide (PI, 1µg/mL; Sigma Aldrich, cat. P4170) and incubated for 20 min shaking in the dark. The plates were then read using Operetta-High Content Imaging System (Perkin Elmer) and analysed using the Harmony Software. The number of viable cells was calculated by subtracting PI positive cells from the total number of cells estimated by Hoechst 33342 staining and normalized on the control. Each treatment was performed in technical quadruplicate and in biological triplicate.

8.18 INTRACRANIAL IMPLANTATION OF GSCs IN IMMUNOCOMPROMISED MICE AND ANALYSIS OF BRAIN XENOGRAFTS

In vivo experiments were performed by Roberto Pallini's group at the Università Cattolica del Sacro Cuore, in Rome. Experiments involving animals were approved by the Ethical Committee of the Istituto Superiore di Sanità, Rome, Italy. NOD-SCID mice (4–6 weeks old; Charles River, Italy) were implanted intracranially with 2 x 10^5 green fluorescence protein (GFP)-expressing GSC#1 cells resuspended in 5 µL of serum-free DMEM. For grafting, the mice were anesthetized with intraperitoneal injection of diazepam (2 mg/100 g) followed by intramuscular injection of ketamine (4 mg/100 g). Animal skulls were immobilized in a stereotactic head frame and a burr hole was made 2 mm right of the midline and 1 mm anterior to the coronal suture, and cells were slowly injected using the tip of a 10-µL Hamilton microsyringe placed at a depth of 3.5 mm from the dura. After grafting, the animals were kept under pathogen-free conditions in positive-pressure cabinets (Tecniplast Gazzada, Varese, Italy) and observed daily for neurological signs. Beginning 8 weeks after implantation, the mice (n=4) were treated with Q/D (200 mg/kg ip in PBS) three times weekly for 3 weeks. Control animals (n=4) were treated with PBS. Body weight was monitored weekly. One week after discontinuation of therapy, the mice were deeply anesthetized and transcardially perfused with 0.1 X PBS (pH 7.4), then treated with 4% paraformaldehyde in 0.1 X PBS. The brain was removed, stored in 30% sucrose buffer overnight at 4°C, and serially cryotomed at 40 µm on the coronal plane. Sections were collected in distilled water, mounted on slides, and cover-slipped with Eukitt. Images were obtained with a Laser Scanning Confocal Microscope (IX81, Olympus Inc, Melville, NY). In

control and Q/D-treated xenografts the density of tumor cells was assessed by counting the number of GFP-expressing GSCs in 10 non-superimposing 200x fields across the thalamus, fimbria, and optic tract of the right brain hemisphere.

In order to perform immunofluorescence to assess BBB integrity, brain sections were incubated in ice-cold 100% methanol for 10 minutes at room temperature. After a wash in PBS for 5 minutes, sections were incubated in PBS containing 5% normal donkey serum for 45 minutes and then incubated in 1:200 rabbit anti-Glucose Transporter-1 (Glut-1) (Merck Millipore, Burlington, MA) antibody, overnight at 4°C. After washes in PBS, sections were incubated for 1 hour at room temperature with an anti-rabbit secondary antibody (Vector Laboratories). Confocal images were generated using a Zeiss 510 Meta confocal microscope. Differences in density of GSCs between the Q/D-treated and control group were evaluated using Student's t-test.

8.19 QUANTIFICATION AND STATISTICAL ANALYSIS

Results were reported as mean ± SD (standard deviation) or mean ± SE (standard error of the mean), as indicated in the figure legend. Details of each analysis are in figure legends. All *in vitro* experiments were repeated at least two times and animal experiments were performed once. All the experiments with representative images (including western blot and immunofluorescence) have been repeated at least twice and representative images are shown.

8.20 SEMISYNTHESIS OF A FIRST DALFOPRISTIN DIELS ALDER ADDUCT

Reagents and solvents were purchased from Sigma Aldrich or Merck VWR and used without further purification.

Thin layer chromatography (TLC) was carried out to monitor reactions using *Merck Kieselgel 60* PF_{254} TLC plates. Different spots were visualized using short wave ultraviolet light (254nm) and/or $Ce(SO_4)_2$ staining. Solvent conditions are reported and the retention factors (*Rf*) for the respective compounds are stated. Preparative thin layer chromatography (PLC) was used for compounds purification and was performed on 20 x 20 cm *Merck Kieselgel 60* F_{254} 0.5 mm plates.

Microwave-assisted reactions were carried out using a mono-mode CEM Discover reactor in a sealed vessel, monitoring the temperature of reaction mixtures by an external infrared control system.

All evaporations were performed at reduced pressure.

The structure of all reported compounds was elucidated through the use of proton (^{1}H) nuclear magnetic resonance (NMR) technique. NMR spectra were recorded on a Bruker-Avance 400 spectrometer by using a 5 mm BBI probe with 90° proton pulse length of 8 μsec at a transmission power of 0 db; ^{1}H at 400 MHz were registered in $CDCl_3$, which was previously treated on basic alumina to avoid acidic traces. Chemical shift (δ) values are given in part per million (ppm).

Electrospray ionization (ESI)-MS mass spectra was performed on a Bruker Esquire-LC spectrometer with an electrospray ion source used in positive or negative ion mode by direct infusion of a methanolic solution of the sample, under the following conditions: source temperature 300C, drying gas N_2, 4 L/min, positive ion mode, ISV 4 kV, OV 38.3 V, scan range 100–1,000 *m/z*.

REFERENCES

Abbott, N.J. (2013). Blood–brain barrier structure and function and the challenges for CNS drug delivery. J. Inherit. Metab. Dis. *36*, 437–449.

Abbott, N.J., Patabendige, A.A.K., Dolman, D.E.M., Yusof, S.R., and Begley, D.J. (2010). Structure and function of the blood–brain barrier. Neurobiol. Dis. *37*, 13–25.

Adams, P.D., Afonine, P. V., Bunkóczi, G., Chen, V.B., Davis, I.W., Echols, N., Headd, J.J., Hung, L.-W., Kapral, G.J., Grosse-Kunstleve, R.W., et al. (2010). *PHENIX* : a comprehensive Python-based system for macromolecular structure solution. Acta Crystallogr. Sect. D Biol. Crystallogr. *66*, 213–221.

Alessandrini, F., Cristofaro, I., Di Bari, M., Zasso, J., Conti, L., and Tata, A.M. (2015). The activation of M2 muscarinic receptor inhibits cell growth and survival in human glioblastoma cancer stem cells. Int. Immunopharmacol. *29*, 105–109.

Amunts, A., Brown, A., Toots, J., Scheres, S.H.W., and Ramakrishnan, V. (2015). The structure of the human mitochondrial ribosome. Science (80). *348*, 95–98.

Anderson, S., Bankier, A.T., Barrell, B.G., de Bruijn, M.H.L., Coulson, A.R., Drouin, J., Eperon, I.C., Nierlich, D.P., Roe, B.A., Sanger, F., et al. (1981). Sequence and organization of the human mitochondrial genome. Nature *290*, 457–465.

Angeletti, F., Fossati, G., Pattarozzi, A., Würth, R., Solari, A., Daga, A., Masiello, I., Barbieri, F., Florio, T., and Comincini, S. (2016). Inhibition of the autophagy pathway synergistically potentiates the cytotoxic activity of givinostat (ITF2357) on human glioblastoma cancer stem cells. Front. Mol. Neurosci. *9*, 107.

Appleyard, M.V.C.L., Murray, K.E., Coates, P.J., Wullschleger, S., Bray, S.E., Kernohan, N.M., Fleming, S., Alessi, D.R., and Thompson, A.M. (2012). Phenformin as prophylaxis and therapy in breast cancer xenografts. Br. J. Cancer *106*, 1117–1122.

Ashton, T.M., McKenna, W.G., Kunz-Schughart, L.A., and Higgins, G.S. (2018). Oxidative phosphorylation as an emerging target in cancer therapy. Clin. Cancer Res. clincanres.3070.2017.

Aubry, M., de Tayrac, M., Etcheverry, A., Clavreul, A., Saikali, S., Menei, P., and Mosser, J. (2015). From the core to beyond the margin: a genomic picture of glioblastoma intratumor heterogeneity. Oncotarget *6*, 12094–12109.

Auffinger, B., Tobias, A.L., Han, Y., Lee, G., Guo, D., Dey, M., Lesniak, M.S., and Ahmed, A.U. (2014). Conversion of differentiated cancer cells into cancer stem-like cells in a glioblastoma model after primary chemotherapy. Cell Death Differ. *21*, 1119–1131.

Bacque, E., Barriere, J.-C., and Berthaud, N. (2005). Recent progress in the field of antibacterial pristinamycins. Curr. Med. Chem. -Anti-Infective Agents *4*, 185–217.

Ban, N., Nissen, P., Hansen, J., Moore, P.B., and Steitz, T.A. (2000). The complete atomic structure of the large ribosomal subunit at 2.4 A resolution. Science *289*, 905–920.

Bao, S., Wu, Q., McLendon, R.E., Hao, Y., Shi, Q., Hjelmeland, A.B., Dewhirst, M.W., Bigner, D.D., and Rich, J.N. (2006). Glioma stem cells promote radioresistance by preferential activation of the DNA damage response. Nature *444*, 756–760.

Barriere, J.C., Bouanchaud, D.H., Paris, J.M., Rolin, O., Harris, N. V., and Smith, C. (1992). Antimicrobial activity against Staphylococcus aureus of semisynthetic injectable streptogramins: RP 59500 and related compounds. J. Antimicrob. Chemother. *30*, 1–8.

Barrière, J.C., Berthaud, N., Beyer, D., Dutka-Malen, S., Paris, J.M., and Desnottes, J.F. (1998). Recent developments in streptogramin research. Curr. Pharm. Des. *4*, 155–180.

Bearden, D.T. (2004). Clinical pharmacokinetics of quinupristin/dalfopristin. Clin. Pharmacokinet. *43*, 239–252.

Bergeron, M., and Montay, G. (1997). The pharmacokinetics of quinupristin/dalfopristin in laboratory animals and in humans. J. Antimicrob. Chemother. *39*, 129–138.

Berridge, M. V., Herst, P.M., and Tan, A.S. (2010). Metabolic flexibility and cell hierarchy in metastatic cancer. Mitochondrion *10*, 584–588.

Berry, E.A., Guergova-Kuras, M., Huang, L., and Crofts, A.R. (2000). Structure and function of cytochrome *bc* complexes. Annu. Rev. Biochem. *69*, 1005–1075.

Bhargava, K., Templeton, P., and Spremulli, L.L. (2004). Expression and characterization of isoform 1 of human mitochondrial elongation factor G. Protein Expr. Purif. *37*, 368–376.

Birsoy, K., Possemato, R., Lorbeer, F.K., Bayraktar, E.C., Thiru, P., Yucel, B., Wang, T., Chen, W.W., Clish, C.B., and Sabatini, D.M. (2014). Metabolic determinants of cancer cell sensitivity to glucose limitation and biguanides. Nature *508*, 108–112.

Bonfiglio, G., and Furneri, P.M. (2001). Novel streptogramin antibiotics. Expert Opin. Investig. Drugs *10*, 185–198.

Brem, H., Piantadosi, S., Burger, P.C., Walker, M., Selker, R., Vick, N.A., Black, K., Sisti, M., Brem, S., and Mohr, G. (1995). Placebo-controlled trial of safety and efficacy of intraoperative controlled delivery by biodegradable polymers of chemotherapy for recurrent gliomas. The Polymer-brain Tumor Treatment Group. Lancet (London, England) *345*, 1008–1012.

Brennan, C.W., Verhaak, R.G.W., McKenna, A., Campos, B., Noushmehr, H., Salama, S.R., Zheng, S., Chakravarty, D., Sanborn, J.Z., Berman, S.H., et al. (2013). The somatic genomic landscape of glioblastoma. Cell *155*, 462–477.

Brescia, P., Richichi, C., and Pelicci, G. (2012). Current strategies for identification of glioma stem cells: adequate or unsatisfactory? J. Oncol. *2012*, 1–10.

Brodbelt, A., Greenberg, D., Winters, T., Williams, M., Vernon, S., Collins, V.P., and (UK) National Cancer Information Network Brain Tumour Group (2015). Glioblastoma in England: 2007–2011. Eur. J. Cancer *51*, 533–542.

Brown, A., Amunts, A., Bai, X.-C., Sugimoto, Y., Edwards, P.C., Murshudov, G., Scheres, S.H.W., and Ramakrishnan, V. (2014). Structure of the large ribosomal subunit from human mitochondria. Science *346*, 718–722.

Cabrera, M.C., Hollingsworth, R.E., and Hurt, E.M. (2015). Cancer stem cell plasticity and tumor hierarchy. World J. Stem Cells *7*, 27–36.

Cai, Y.-C., Bullard, J.M., Thompson, N.L., and Spremulli, L.L. (2000). Interaction of mitochondrial elongation factor Tu with Aminoacyl-tRNA and elongation factor Ts. J. Biol. Chem. *275*, 20308–20314.

Calabrese, C., Poppleton, H., Kocak, M., Hogg, T.L., Fuller, C., Hamner, B., Oh, E.Y., Gaber, M.W., Finklestein, D., Allen, M., et al. (2007). A perivascular niche for brain tumor stem cells. Cancer Cell *11*, 69–82.

Cavalli, L.R., Varella-Garcia, M., and Liang, B.C. (1997). Diminished tumorigenic phenotype after depletion of mitochondrial DNA. Cell Growth Differ. *8*, 1189–1198.

Cecchini, G. (2003). Function and structure of complex II of the respiratory chain. Annu. Rev. Biochem. *72*, 77–109.

Chen, J., Li, Y., Yu, T.-S., McKay, R.M., Burns, D.K., Kernie, S.G., and Parada, L.F. (2012). A restricted cell population propagates glioblastoma growth after chemotherapy. Nature *488*, 522–526.

Chen, V.B., Arendall, W.B., Headd, J.J., Keedy, D.A., Immormino, R.M., Kapral, G.J., Murray, L.W., Richardson, J.S., and Richardson, D.C. (2010). *MolProbity* : all-atom structure validation for macromolecular crystallography. Acta Crystallogr. Sect. D Biol. Crystallogr. *66*, 12–21.

Cheng, G., Zielonka, J., Dranka, B.P., McAllister, D., Mackinnon, A.C., Joseph, J., and Kalyanaraman, B. (2012). Mitochondria-targeted drugs synergize with 2-deoxyglucose to trigger breast cancer cell death. Cancer Res. *72*, 2634–2644.

Cheng, G., Zielonka, J., Ouari, O., Lopez, M., McAllister, D., Boyle, K., Barrios, C.S., Weber, J.J., Johnson, B.D., Hardy, M., et al. (2016). Mitochondria-targeted analogues of metformin exhibit enhanced antiproliferative and radiosensitizing effects in pancreatic Cancer Cells. Cancer Res. *76*, 3904–3915.

Christian, B.E., and Spremulli, L.L. (2012). Mechanism of protein biosynthesis in mammalian mitochondria. Biochim. Biophys. Acta - Gene Regul. Mech. *1819*, 1035–1054.

Cojoc, M., Mäbert, K., Muders, M.H., and Dubrovska, A. (2015). A role for cancer stem cells in therapy resistance: cellular and molecular mechanisms. Semin. Cancer Biol. *31*, 16–27.

Cominelli, M., Grisanti, S., Mazzoleni, S., Branca, C., Buttolo, L., Furlan, D., Liserre, B., Bonetti, M.F., Medicina, D., Pellegrini, V., et al. (2015). EGFR amplified and overexpressing glioblastomas and association with better response to adjuvant metronomic temozolomide. JNCI J. Natl. Cancer Inst. *107*.

Conti, L., Crisafulli, L., Caldera, V., Tortoreto, M., Brilli, E., Conforti, P., Zunino, F., Magrassi, L., Schiffer, D., and Cattaneo, E. (2012). REST controls self-renewal and tumorigenic competence of human glioblastoma cells. PLoS One *7*, e38486.

Contreras, A., and Vázquez, D. (1977). Synergistic interaction of the streptogramins with the ribosome. Eur. J. Biochem. *74*, 549–551.

Couvillion, M.T., Soto, I.C., Shipkovenska, G., and Churchman, L.S. (2016). Synchronized mitochondrial and cytosolic translation programs. Nature *533*, 499–503.

Crinière, E., Kaloshi, G., Laigle-Donadey, F., Lejeune, J., Auger, N., Benouaich-Amiel, A., Everhard, S., Mokhtari, K., Polivka, M., Delattre, J.-Y., et al. (2007). MGMT prognostic impact on glioblastoma is dependent on therapeutic modalities. J. Neurooncol. *83*, 173–179.

Dalva-Aydemir, S., Bajpai, R., Martinez, M., Adekola, K.U.A., Kandela, I., Wei, C., Singhal, S., Koblinski, J.E., Raje, N.S., Rosen, S.T., et al. (2015). Targeting the metabolic plasticity of multiple myeloma with FDA-approved ritonavir and metformin. Clin. Cancer Res. *21*, 1161–1171.

Daneman, R., and Prat, A. (2015). The blood–brain barrier. Cold Spring Harb. Perspect. Biol. *7*, a020412.

DeBerardinis, R.J., and Chandel, N.S. (2016). Fundamentals of cancer metabolism. Sci. Adv. *2*, e1600200–e1600200.

Delgado, G., Neuhauser, M.M., Bearden, D.T., and Danziger, L.H. (2000). Quinupristin-dalfopristin: an overview. Pharmacotherapy *20*, 1469–1485.

Emsley, P., and Cowtan, K. (2004). *Coot* : model-building tools for molecular graphics. Acta Crystallogr. Sect. D Biol. Crystallogr. *60*, 2126–2132.

Englmeier, R., Pfeffer, S., and Förster, F. (2017). Structure of the human mitochondrial ribosome studied in situ by cryoelectron tomography. Structure *25*, 1574–1581.e2.

Eramo, A., Ricci-Vitiani, L., Zeuner, A., Pallini, R., Lotti, F., Sette, G., Pilozzi, E., Larocca, L.M., Peschle, C., and De Maria, R. (2006). Chemotherapy resistance of glioblastoma stem cells. Cell Death Differ. *13*, 1238–1241.

Etienne, S.D., Montay, G., Le Liboux, A., Frydman, A., and Garaud, J.J. (1992). A phase I, double-blind, placebo-controlled study of the tolerance and pharmacokinetic behaviour of RP 59500. J. Antimicrob. Chemother. *30 Suppl A*, 123–131.

Evans, J.M.M., Donnelly, L.A., Emslie-Smith, A.M., Alessi, D.R., and Morris, A.D. (2005). Metformin and reduced risk of cancer in diabetic patients. BMJ *330*, 1304–1305.

Fiorillo, M., Lamb, R., Tanowitz, H.B., Mutti, L., Krstic-Demonacos, M., Cappello, A.R., Martinez-Outschoorn, U.E., Sotgia, F., and Lisanti, M.P. (2016). Repurposing atovaquone: targeting mitochondrial complex III and OXPHOS to eradicate cancer stem cells. Oncotarget *7*, 34084–34099.

Frattini, V., Pagnotta, S.M., Tala, Fan, J.J., Russo, M. V., Lee, S.B., Garofano, L., Zhang, J., Shi, P., Lewis, G., et al. (2018). A metabolic function of FGFR3-TACC3 gene fusions in cancer. Nature *553*, 222–227.

Galli, R., Binda, E., Orfanelli, U., Cipelletti, B., Gritti, A., De Vitis, S., Fiocco, R., Foroni, C., Dimeco, F., and Vescovi, A. (2004). Isolation and characterization of tumorigenic, stem-like neural precursors from human glioblastoma. Cancer Res. *64*, 7011–7021.

Gaur, R., Grasso, D., Datta, P.P., Krishna, P.D.V., Das, G., Spencer, A., Agrawal, R.K., Spremulli, L., and Varshney, U. (2008). A single mammalian mitochondrial translation initiation factor functionally replaces two bacterial factors. Mol. Cell *29*, 180–190.

Di Giambattista, M., Chinali, G., and Cocito, C. (1989). The molecular basis of the inhibitory activities of type A and type B synergimycins and related antibiotics on ribosomes. J. Antimicrob. Chemother. *24*, 485–507.

Gou, S., Cui, P., Li, X., Shi, P., Liu, T., and Wang, C. (2013). Low concentrations of metformin selectively inhibit CD133+ cell proliferation in pancreatic cancer and have anticancer action. PLoS One *8*, e63969.

Gray, M.W. (2012). Mitochondrial evolution. Cold Spring Harb. Perspect. Biol. *4*, a011403.

Gray, M.W., Burger, G., and Lang, B.F. (1999). Mitochondrial evolution. Science *283*, 1476–1481.

Greber, B.J., and Ban, N. (2016). Structure and function of the mitochondrial ribosome. Annu. Rev. Biochem. *85*, 103–132.

Greber, B.J., Boehringer, D., Leitner, A., Bieri, P., Voigts-Hoffmann, F., Erzberger, J.P., Leibundgut, M., Aebersold, R., and Ban, N. (2014b). Architecture of the large subunit of the mammalian mitochondrial ribosome. Nature *505*, 515–519.

Greber, B.J., Boehringer, D., Leibundgut, M., Bieri, P., Leitner, A., Schmitz, N., Aebersold, R., and Ban, N. (2014a). The complete structure of the large subunit of the mammalian mitochondrial ribosome. Nature *515*, 283–286.

Greber, B.J., Bieri, P., Leibundgut, M., Leitner, A., Aebersold, R., Boehringer, D., and Ban, N. (2015). Ribosome. The complete structure of the 55S mammalian mitochondrial ribosome. Science *348*, 303–308.

Griguer, C.E., Cantor, A.B., Fathallah-Shaykh, H.M., Gillespie, G.Y., Gordon, A.S., Markert, J.M., Radovanovic, I., Clement-Schatlo, V., Shannon, C.N., and Oliva, C.R. (2013). Prognostic relevance of cytochrome c oxidase in primary glioblastoma multiforme. PLoS One *8*, e61035.

Guan, M.-X. (2011). Mitochondrial 12S rRNA mutations associated with aminoglycoside ototoxicity. Mitochondrion *11*, 237–245.

Gurk-Turner, C. (2000). Quinupristin/dalfopristin: the first available macrolide-lincosamide-streptogramin antibiotic. Proc. (Bayl. Univ. Med. Cent). *13*, 83–86.

Gürsel, D.B., Shin, B.J., Burkhardt, J.-K., Kesavabhotla, K., Schlaff, C.D., and Boockvar, J.A. (2011). Glioblastoma stem-like cells—Biology and therapeutic implications. Cancers (Basel). *3*, 2655–2666.

Hadjipanayis, C.G., Widhalm, G., and Stummer, W. (2015). What is the surgical benefit of utilizing 5-aminolevulinic acid for fluorescence-guided surgery of malignant gliomas? Neurosurgery *77*, 663–673.

Hällberg, B.M., and Larsson, N.-G. (2014). Making proteins in the powerhouse. Cell Metab. *20*, 226–240.

Hamaï, A., Codogno, P., and Mehrpour, M. (2014). Cancer stem cells and autophagy: facts and perspectives. J. Cancer Stem Cell Res. *2*, 1.

Hambardzumyan, D., and Bergers, G. (2015). Glioblastoma: defining tumor niches. Trends in Cancer *1*, 252–265.

Hanahan, D., and Weinberg, R.A. (2011). Hallmarks of cancer: the next generation. Cell *144*, 646–674.

Harms, J.M., Schlünzen, F., Fucini, P., Bartels, H., and Yonath, A. (2004). Alterations at the peptidyl transferase centre of the ribosome induced by the synergistic action of the streptogramins dalfopristin and quinupristin. BMC Biol. *2*, 4.

Hayashi, J., Takemitsu, M., and Nonaka, I. (1992). Recovery of the missing tumorigenicity in mitochondrial DNA-less HeLa cells by introduction of mitochondrial DNA from normal human cells. Somat. Cell Mol. Genet. *18*, 123–129.

Hegi, M.E., Diserens, A.-C., Gorlia, T., Hamou, M.-F., de Tribolet, N., Weller, M., Kros, J.M., Hainfellner, J.A., Mason, W., Mariani, L., et al. (2005). *MGMT* gene silencing and benefit from temozolomide in glioblastoma. N. Engl. J. Med. *352*, 997–1003.

Hirst, J. (2013). Mitochondrial complex I. Annu. Rev. Biochem. *82*, 551–575.

Ignatova, T.N., Kukekov, V.G., Laywell, E.D., Suslov, O.N., Vrionis, F.D., and Steindler, D.A. (2002). Human cortical glial tumors contain neural stem-like cells expressing astroglial and neuronal markers in vitro. Glia *39*, 193–206.

Jahangiri, A., Chin, A.T., Flanigan, P.M., Chen, R., Bankiewicz, K., and Aghi, M.K. (2017). Convection-enhanced delivery in glioblastoma: a review of preclinical and clinical studies. J. Neurosurg. *126*, 191–200.

Janiszewska, M., Suvà, M.L., Riggi, N., Houtkooper, R.H., Auwerx, J., Clément-Schatlo, V., Radovanovic, I., Rheinbay, E., Provero, P., and Stamenkovic, I. (2012). Imp2 controls oxidative phosphorylation and is crucial for preserving glioblastoma cancer stem cells. Genes Dev. *26*, 1926–1944.

Jawhari, S., Ratinaud, M.-H., and Verdier, M. (2016). Glioblastoma, hypoxia and autophagy: a survival-prone 'ménage-à-trois.' Cell Death Dis. *7*, e2434–e2434.

Jenner, L., Starosta, A.L., Terry, D.S., Mikolajka, A., Filonava, L., Yusupov, M., Blanchard, S.C., Wilson, D.N., and Yusupova, G. (2013). Structural basis for potent inhibitory activity of the antibiotic tigecycline during protein synthesis. Proc. Natl. Acad. Sci. *110*, 3812–3816.

Jose, C., Bellance, N., and Rossignol, R. (2011). Choosing between glycolysis and oxidative phosphorylation: a tumor's dilemma? Biochim. Biophys. Acta - Bioenerg. *1807*, 552–561.

Ke, X.-Y., Lin Ng, V.W., Gao, S.-J., Tong, Y.W., Hedrick, J.L., and Yang, Y.Y. (2014). Co-delivery of thioridazine and doxorubicin using polymeric micelles for targeting both cancer cells and cancer stem cells. Biomaterials *35*, 1096–1108.

Keilin, D. (1925). On cytochrome, a respiratory pigment, common to animals, yeast, and higher plants. Proc. R. Soc. London Ser. B *100*, 129-151.

Keilin D. (1966). The history of cell respiration and cytochrome. (Cambridge University Press, Cambridge, UK).

Khosla, D. (2016). Concurrent therapy to enhance radiotherapeutic outcomes in glioblastoma. Ann. Transl. Med. *4*, 54.

Kim, S.-S., Pirollo, K.F., and Chang, E.H. (2015). Isolation and culturing of glioma cancer stem cells. In Current Protocols in Cell Biology, (Hoboken, NJ, USA: John Wiley & Sons, Inc.), p. 23.10.1-23.10.10.

Kimanius, D., Forsberg, B.O., Scheres, S.H., and Lindahl, E. (2016). Accelerated cryo-EM structure determination with parallelisation using GPUs in RELION-2. Elife *5*, e18722.

Koc, E.C., and Spremulli, L.L. (2002). Identification of mammalian mitochondrial translational initiation factor 3 and examination of its role in initiation complex formation with natural mRNAs. J. Biol. Chem. *277*, 35541–35549.

Kuntz, E.M., Baquero, P., Michie, A.M., Dunn, K., Tardito, S., Holyoake, T.L., Helgason, G.V., and Gottlieb, E. (2017). Targeting mitochondrial oxidative phosphorylation eradicates therapy-resistant chronic myeloid leukemia stem cells. Nat. Med. *23*, 1234–1240.

Lam, Y.K.T., Dai, P., Zink, D.L., Smith, A.J., Lee, N.W., Freedman, S., and Salvatore, M.J. (1993). New virginiamycin M1 derivatives: synthesis, cholecystokinin binding inhibitory and antimicrobial properties. J. Antibiot. (Tokyo). *46*, 623–630.

Lambert, T. (2012). Antibiotics that affect the ribosome. Rev. Sci. Tech. *31*, 57–64.

Lan, X., Jörg, D.J., Cavalli, F.M.G., Richards, L.M., Nguyen, L. V., Vanner, R.J., Guilhamon, P., Lee, L., Kushida, M.M., Pellacani, D., et al. (2017). Fate mapping of human glioblastoma reveals an invariant stem cell hierarchy. Nature *549*, 227–232.

Lange, C., and Hunte, C. (2002). Crystal structure of the yeast cytochrome bc1 complex with its bound substrate cytochrome c. Proc. Natl. Acad. Sci. *99*, 2800–2805.

Larjavaara, S., Mantyla, R., Salminen, T., Haapasalo, H., Raitanen, J., Jaaskelainen, J., and Auvinen, A. (2007). Incidence of gliomas by anatomic location. Neuro. Oncol. *9*, 319–325.

Lathia, J.D., Mack, S.C., Mulkearns-Hubert, E.E., Valentim, C.L.L., and Rich, J.N. (2015). Cancer stem cells in glioblastoma. Genes Dev. *29*, 1203–1217.

Lauschke, K., Frederiksen, L., and Hall, V.J. (2017). Paving the way toward complex blood-brain barrier models using pluripotent stem cells. Stem Cells Dev. *26*, 857–874.

Ledur, P.F., Onzi, G.R., Zong, H., and Lenz, G. (2017). Culture conditions defining glioblastoma cells behavior: what is the impact for novel discoveries? Oncotarget *8*, 69185–69197.

Lee, S.Y. (2016). Temozolomide resistance in glioblastoma multiforme. Genes Dis. *3*, 198–210.

Li, Q., and Seiple, I.B. (2017). Modular, scalable synthesis of group A streptogramin antibiotics. J. Am. Chem. Soc. *139*, 13304–13307.

Li, D., Shi, A., Zhang, W.-X., Liu, G., and Xi, Z. (2008). Selective synthesis of multiply substituted 7-norbornenone derivatives or Diels–Alder cycloadducts from 1,2,3,4-tetrasubstituted 1,3-butadienes and maleic anhydride with or without Lewis acids. Tetrahedron *64*, 9895–9900.

Li, Z., Bao, S., Wu, Q., Wang, H., Eyler, C., Sathornsumetee, S., Shi, Q., Cao, Y., Lathia, J., McLendon, R.E., et al. (2009). Hypoxia-inducible factors regulate tumorigenic capacity of glioma stem cells. Cancer Cell *15*, 501–513.

Liu, M., and Spremulli, L. (2000). Interaction of mammalian mitochondrial ribosomes with the inner membrane. J. Biol. Chem. *275*, 29400–29406.

Liu, G., Yuan, X., Zeng, Z., Tunici, P., Ng, H., Abdulkadir, I.R., Lu, L., Irvin, D., Black, K.L., and Yu, J.S. (2006). Analysis of gene expression and chemoresistance of CD133+ cancer stem cells in glioblastoma. Mol. Cancer *5*, 67.

Louis, D.N., Perry, A., Reifenberger, G., von Deimling, A., Figarella-Branger, D., Cavenee, W.K., Ohgaki, H., Wiestler, O.D., Kleihues, P., and Ellison, D.W. (2016). The 2016 World Health Organization classification of tumors of the central nervous system: a summary. Acta Neuropathol. *131*, 803–820.

Mai, N., Chrzanowska-Lightowlers, Z.M.A., and Lightowlers, R.N. (2017). The process of mammalian mitochondrial protein synthesis. Cell Tissue Res. *367*, 5–20.

Marchetti, P., Guerreschi, P., Mortier, L., and Kluza, J. (2015). Integration of mitochondrial targeting for molecular cancer therapeutics. Int. J. Cell Biol. *2015*, 1–17.

Martinez-Outschoorn, U.E., Peiris-Pagés, M., Pestell, R.G., Sotgia, F., and Lisanti, M.P. (2017). Cancer metabolism: a therapeutic perspective. Nat. Rev. Clin. Oncol. *14*, 11–31.

McBride, H.M., Neuspiel, M., and Wasiak, S. (2006). Mitochondria: more than just a powerhouse. Curr. Biol. *16*, R551–R560.

McLendon, R., Friedman, A., Bigner, D., Van Meir, E.G., Brat, D.J., M. Mastrogianakis, G., Olson, J.J., Mikkelsen, T., Lehman, N., Aldape, K., et al. (2008). Comprehensive genomic characterization defines human glioblastoma genes and core pathways. Nature *455*, 1061–1068.

Mitchell, P. (1961). Coupling of phosphorylation to electron and hydrogen transfer by a chemi-osmotic type of mechanism. Nature *191*, 144–148.

Mizushima, N., Yoshimori, T., and Levine, B. (2010). Methods in mammalian autophagy research. Cell *140*, 313–326.

Mohammadi, A.M., Sullivan, T.B., Barnett, G.H., Recinos, V., Angelov, L., Kamian, K., and Vogelbaum, M.A. (2014). Use of high-field intraoperative magnetic resonance imaging to enhance the extent of resection of enhancing and nonenhancing gliomas. Neurosurgery *74*, 339–350.

Molina, J.R., Sun, Y., Protopopova, M., Gera, S., Bandi, M., Bristow, C., McAfoos, T., Morlacchi, P., Ackroyd, J., Agip, A.-N.A., et al. (2018). An inhibitor of oxidative phosphorylation exploits cancer vulnerability. Nat. Med. *24*, 1036–1046.

Montoya, J., Ojala, D., and Attardi, G. (1981). Distinctive features of the 5′-terminal sequences of the human mitochondrial mRNAs. Nature *290*, 465–470.

Moreno-Sánchez, R., Marín-Hernández, A., Saavedra, E., Pardo, J.P., Ralph, S.J., and Rodríguez-Enríquez, S. (2014). Who controls the ATP supply in cancer cells? Biochemistry lessons to understand cancer energy metabolism. Int. J. Biochem. Cell Biol. *50*, 10–23.

Neupert, W. (2015). A perspective on transport of proteins into mitochondria: a myriad of open questions. J. Mol. Biol. *427*, 1135–1158.

Newton, H.B., and Otero, J.J. (2015). Overview of epidemiology, pathology, and treatment of primary brain tumors. In Epilepsy and Brain Tumors, (Elsevier), pp. 11–28.

Nijtmans, L., Henderson, N.S., and Holt, I.J. (2002). Blue Native electrophoresis to study mitochondrial and other protein complexes. Methods *26*, 327–334.

Nijtmans, L.G.J., Klement, P., Houštěk, J., and van den Bogert, C. (1995). Assembly of mitochondrial ATP synthase in cultured human cells: implications for mitochondrial diseases. Biochim. Biophys. Acta - Mol. Basis Dis. *1272*, 190–198.

Nissen, P., Hansen, J., Ban, N., Moore, P.B., and Steitz, T.A. (2000). The structural basis of ribosome activity in peptide bond synthesis. Science *289*, 920–930.

Nixon, G.L., Moss, D.M., Shone, A.E., Lalloo, D.G., Fisher, N., O'Neill, P.M., Ward, S.A., and Biagini, G.A. (2013). Antimalarial pharmacology and therapeutics of atovaquone. J. Antimicrob. Chemother. *68*, 977–985.

Noeske, J., Huang, J., Olivier, N.B., Giacobbe, R.A., Zambrowski, M., and Cate, J.H.D. (2014). Synergy of streptogramin antibiotics occurs independently of their effects on translation. Antimicrob. Agents Chemother. *58*, 5269–5279.

Nowell, P.C. (1976). The clonal evolution of tumor cell populations. Science *194*, 23–28.

O'Brien, T.W. (1971). The general occurrence of 55 S ribosomes in mammalian liver mitochondria. J. Biol. Chem. *246*, 3409–3417.

Ohgaki, H., and Kleihues, P. (2013). The definition of primary and secondary glioblastoma. Clin. Cancer Res. *19*, 764–772.

Oliva, C.R., Nozell, S.E., Diers, A., McClugage, S.G., Sarkaria, J.N., Markert, J.M., Darley-Usmar, V.M., Bailey, S.M., Gillespie, G.Y., Landar, A., et al. (2010). Acquisition of temozolomide chemoresistance in gliomas leads to remodeling of mitochondrial electron transport chain. J. Biol. Chem. *285*, 39759–39767.

Oliva, C.R., Moellering, D.R., Gillespie, G.Y., and Griguer, C.E. (2011). Acquisition of chemoresistance in gliomas is associated with increased mitochondrial coupling and decreased ROS production. PLoS One *6*, e24665.

Oliva, C.R., Markert, T., Ross, L.J., White, E.L., Rasmussen, L., Zhang, W., Everts, M., Moellering, D.R., Bailey, S.M., Suto, M.J., et al. (2016). Identification of small molecule inhibitors of human cytochrome *c* oxidase that target chemoresistant glioma cells. J. Biol. Chem. *291*, 24188–24199.

Oliva, C.R., Zhang, W., Langford, C., Suto, M.J., and Griguer, C.E. (2017). Repositioning chlorpromazine for treating chemoresistant glioma through the inhibition of cytochrome c oxidase bearing the COX4-1 regulatory subunit. Oncotarget *8*, 37568–37583.

Ostrom, Q.T., Gittleman, H., Liao, P., Vecchione-Koval, T., Wolinsky, Y., Kruchko, C., and Barnholtz-Sloan, J.S. (2017). CBTRUS Statistical Report: primary brain and other central nervous system tumors diagnosed in the United States in 2010–2014. Neuro. Oncol. *19*, v1–v88.

Ott, M., Amunts, A., and Brown, A. (2016). Organization and regulation of mitochondrial protein synthesis. Annu. Rev. Biochem. *85*, 77–101.

Paolillo, M., Boselli, C., and Schinelli, S. (2018). Glioblastoma under siege: an overview of current therapeutic strategies. Brain Sci. *8*, 15.

Papa, S., Martino, P.L., Capitanio, G., Gaballo, A., De Rasmo, D., Signorile, A., and Petruzzella, V. (2012). The oxidative phosphorylation system in mammalian mitochondria. In Advances in Experimental Medicine and Biology, pp. 3–37.

Parfait, R., de Béthune, M.P., and Cocito, C. (1978). A spectrofluorimetric study of the interaction between virginiamycin S and bacterial ribosomes. Mol. Gen. Genet. *166*, 45–51.

Pastò, A., Bellio, C., Pilotto, G., Ciminale, V., Silic-Benussi, M., Guzzo, G., Rasola, A., Frasson, C., Nardo, G., Zulato, E., et al. (2014). Cancer stem cells from epithelial ovarian cancer patients privilege oxidative phosphorylation, and resist glucose deprivation. Oncotarget *5*, 4305–4319.

Patel, M.M., and Patel, B.M. (2017). Crossing the blood–brain barrier: recent advances in drug delivery to the brain. CNS Drugs *31*, 109–133.

Pavlova, N.N., and Thompson, C.B. (2016). The emerging hallmarks of cancer metabolism. Cell Metab. *23*, 27–47.

Phillips, H.S., Kharbanda, S., Chen, R., Forrest, W.F., Soriano, R.H., Wu, T.D., Misra, A., Nigro, J.M., Colman, H., Soroceanu, L., et al. (2006). Molecular subclasses of high-grade glioma predict prognosis, delineate a pattern of disease progression, and resemble stages in neurogenesis. Cancer Cell *9*, 157–173.

Pollard, S.M., Yoshikawa, K., Clarke, I.D., Danovi, D., Stricker, S., Russell, R., Bayani, J., Head, R., Lee, M., Bernstein, M., et al. (2009). Glioma stem cell lines expanded in adherent culture have tumor-specific phenotypes and are suitable for chemical and genetic screens. Cell Stem Cell *4*, 568–580.

Prados, M.D., Byron, S.A., Tran, N.L., Phillips, J.J., Molinaro, A.M., Ligon, K.L., Wen, P.Y., Kuhn, J.G., Mellinghoff, I.K., de Groot, J.F., et al. (2015). Toward precision medicine in glioblastoma: the promise and the challenges. Neuro. Oncol. *17*, 1051–1063.

Rahman, M., Reyner, K., Deleyrolle, L., Millette, S., Azari, H., Day, B.W., Stringer, B.W., Boyd, A.W., Johns, T.G., Blot, V., et al. (2015). Neurosphere and adherent culture conditions are equivalent for malignant glioma stem cell lines. Anat. Cell Biol. *48*, 25.

Ravà, M., D'Andrea, A., Nicoli, P., Gritti, I., Donati, G., Doni, M., Giorgio, M., Olivero, D., and Amati, B. (2018). Therapeutic synergy between tigecycline and venetoclax in a preclinical model of MYC/BCL2 double-hit B cell lymphoma. Sci. Transl. Med. *10*, eaan8723.

Reardon, D.A., and Wen, P.Y. (2015). Unravelling tumour heterogeneity—implications for therapy. Nat. Rev. Clin. Oncol. *12*, 69–70.

Reed, G.A., Schiller, G.J., Kambhampati, S., Tallman, M.S., Douer, D., Minden, M.D., Yee, K.W., Gupta, V., Brandwein, J., Jitkova, Y., et al. (2016). A Phase 1 study of intravenous infusions of tigecycline in patients with acute myeloid leukemia. Cancer Med. *5*, 3031–3040.

Ricci-Vitiani, L., Pallini, R., Biffoni, M., Todaro, M., Invernici, G., Cenci, T., Maira, G., Parati, E.A., Stassi, G., Larocca, L.M., et al. (2010). Tumour vascularization via endothelial differentiation of glioblastoma stem-like cells. Nature *468*, 824–828.

Rich, J.N. (2016). Cancer stem cells: understanding tumor heirarchy and heterogeneity. Medicine (Baltimore). *95*, S2–S7.

Rich, P.R. (2003). The molecular machinery of Keilin's respiratory chain. Biochem. Soc. Trans. *31*, 1095–1105.

Richter-Dennerlein, R., Oeljeklaus, S., Lorenzi, I., Ronsör, C., Bareth, B., Schendzielorz, A.B., Wang, C., Warscheid, B., Rehling, P., and Dennerlein, S. (2016). Mitochondrial protein synthesis adapts to influx of nuclear-encoded protein. Cell *167*, 471–483.e10.

Richter, O.-M.H., and Ludwig, B. (2003). Cytochrome *c* oxidase — structure, function, and physiology of a redox-driven molecular machine. In Reviews of Physiology, Biochemistry and Pharmacology, (Berlin, Heidelberg: Springer Berlin Heidelberg), pp. 47–74.

Ropolo, M., Daga, A., Griffero, F., Foresta, M., Casartelli, G., Zunino, A., Poggi, A., Cappelli, E., Zona, G., Spaziante, R., et al. (2009). Comparative analysis of DNA repair in stem and nonstem glioma cell cultures. Mol. Cancer Res. *7*, 383–392.

Rorbach, J., Richter, R., Wessels, H.J., Wydro, M., Pekalski, M., Farhoud, M., Kühl, I., Gaisne, M., Bonnefoy, N., Smeitink, J.A., et al. (2008). The human mitochondrial ribosome recycling factor is essential for cell viability. Nucleic Acids Res. *36*, 5787–5799.

Rosenthal, P.B., and Henderson, R. (2003). Optimal determination of particle orientation, absolute hand, and contrast loss in single-particle electron cryomicroscopy. J. Mol. Biol. *333*, 721–745.

Sagan, L. (1967). On the origin of mitosing cells. J. Theor. Biol. *14*, 225-IN6.

Ben Sahra, I., Laurent, K., Giuliano, S., Larbret, F., Ponzio, G., Gounon, P., Le Marchand-Brustel, Y., Giorgetti-Peraldi, S., Cormont, M., Bertolotto, C., et al. (2010). Targeting cancer cell metabolism: the combination of metformin and 2-deoxyglucose induces p53-dependent apoptosis in prostate cancer cells. Cancer Res. *70*, 2465–2475.

Sancho, P., Burgos-Ramos, E., Tavera, A., Bou Kheir, T., Jagust, P., Schoenhals, M., Barneda, D., Sellers, K., Campos-Olivas, R., Graña, O., et al. (2015). MYC/PGC-1α balance determines the metabolic phenotype and plasticity of pancreatic cancer stem cells. Cell Metab. *22*, 590–605.

Sancho, P., Barneda, D., and Heeschen, C. (2016). Hallmarks of cancer stem cell metabolism. Br. J. Cancer *114*, 1305–1312.

Sarkaria, J.N., Hu, L.S., Parney, I.F., Pafundi, D.H., Brinkmann, D.H., Laack, N.N., Giannini, C., Burns, T.C., Kizilbash, S.H., Laramy, J.K., et al. (2018). Is the blood–brain barrier really disrupted in all glioblastomas? A critical assessment of existing clinical data. Neuro. Oncol. *20*, 184–191.

Senft, C., Bink, A., Franz, K., Vatter, H., Gasser, T., and Seifert, V. (2011). Intraoperative MRI guidance and extent of resection in glioma surgery: a randomised, controlled trial. Lancet Oncol. *12*, 997–1003.

Shchors, K., Massaras, A., and Hanahan, D. (2015). Dual targeting of the autophagic regulatory circuitry in gliomas with repurposed drugs elicits cell-lethal autophagy and therapeutic benefit. Cancer Cell *28*, 456–471.

Singh, D., Chan, J.M., Zoppoli, P., Niola, F., Sullivan, R., Castano, A., Liu, E.M., Reichel, J., Porrati, P., Pellegatta, S., et al. (2012). Transforming fusions of FGFR and TACC genes in human glioblastoma. Science (80-.). *337*, 1231–1235.

Singh, S.K., Hawkins, C., Clarke, I.D., Squire, J.A., Bayani, J., Hide, T., Henkelman, R.M., Cusimano, M.D., and Dirks, P.B. (2004). Identification of human brain tumour initiating cells. Nature *432*, 396–401.

Škrtić, M., Sriskanthadevan, S., Jhas, B., Gebbia, M., Wang, X., Wang, Z., Hurren, R., Jitkova, Y., Gronda, M., Maclean, N., et al. (2011). Inhibition of mitochondrial translation as a therapeutic strategy for human acute myeloid leukemia. Cancer Cell *20*, 674–688.

Soleimanpour-Lichaei, H.R., Kühl, I., Gaisne, M., Passos, J.F., Wydro, M., Rorbach, J., Temperley, R., Bonnefoy, N., Tate, W., Lightowlers, R., et al. (2007). mtRF1a is a human mitochondrial translation release factor decoding the major termination codons UAA and UAG. Mol. Cell *27*, 745–757.

Song, C.W., Lee, H., Dings, R.P.M., Williams, B., Powers, J., Santos, T. Dos, Choi, B.-H., and Park, H.J. (2012). Metformin kills and radiosensitizes cancer cells and preferentially kills cancer stem cells. Sci. Rep. *2*, 362.

Soriano, A., Miró, O., and Mensa, J. (2005). Mitochondrial toxicity associated with linezolid. N. Engl. J. Med. *353*, 2305–2306.

Spencer, A.C., and Spremulli, L.L. (2005). The interaction of mitochondrial translational initiation factor 2 with the small ribosomal subunit. Biochim. Biophys. Acta - Proteins Proteomics *1750*, 69–81.

Spremulli, L.L., Coursey, A., Navratil, T., and Hunter, S.E. (2004). Initiation and elongation factors in mammalian mitochondrial protein biosynthesis. In Progress in Nucleic Acid Research and Molecular Biology, pp. 211–261.

Stieber, D., Golebiewska, A., Evers, L., Lenkiewicz, E., Brons, N.H.C., Nicot, N., Oudin, A., Bougnaud, S., Hertel, F., Bjerkvig, R., et al. (2014). Glioblastomas are composed of genetically divergent clones with distinct tumourigenic potential and variable stem cell-associated phenotypes. Acta Neuropathol. *127*, 203–219.

Strik, H.M., Marosi, C., Kaina, B., and Neyns, B. (2012). Temozolomide dosing regimens for glioma patients. Curr. Neurol. Neurosci. Rep. *12*, 286–293.

Stummer, W., Reulen, H.-J., Meinel, T., Pichlmeier, U., Schumacher, W., Tonn, J.-C., Rohde, V., Oppel, F., Turowski, B., Woiciechowsky, C., et al. (2008). Extent of resection and survival in glioblastoma multiforme. Neurosurgery *62*, 564–576.

Stupp, R., Mason, W.P., van den Bent, M.J., Weller, M., Fisher, B., Taphoorn, M.J.B., Belanger, K., Brandes, A.A., Marosi, C., Bogdahn, U., et al. (2005). Radiotherapy plus concomitant and adjuvant temozolomide for glioblastoma. N. Engl. J. Med. *352*, 987–996.

Stupp, R., Hegi, M.E., Mason, W.P., van den Bent, M.J., Taphoorn, M.J., Janzer, R.C., Ludwin, S.K., Allgeier, A., Fisher, B., Belanger, K., et al. (2009). Effects of radiotherapy with concomitant and adjuvant temozolomide versus radiotherapy alone on survival in glioblastoma in a randomised phase III study: 5-year analysis of the EORTC-NCIC trial. Lancet Oncol. *10*, 459–466.

Stupp, R., Taillibert, S., Kanner, A.A., Kesari, S., Steinberg, D.M., Toms, S.A., Taylor, L.P., Lieberman, F., Silvani, A., Fink, K.L., et al. (2015). Maintenance therapy with tumor-treating fields plus temozolomide vs temozolomide alone for glioblastoma. JAMA *314*, 2535.

Stupp, R., Taillibert, S., Kanner, A., Read, W., Steinberg, D.M., Lhermitte, B., Toms, S., Idbaih, A., Ahluwalia, M.S., Fink, K., et al. (2017). Effect of tumor-treating fields plus maintenance temozolomide vs maintenance temozolomide alone on survival in patients with glioblastoma. JAMA *318*, 2306.

Sturm, D., Witt, H., Hovestadt, V., Khuong-Quang, D.-A., Jones, D.T.W., Konermann, C., Pfaff, E., Tönjes, M., Sill, M., Bender, S., et al. (2012). Hotspot mutations in H3F3A and IDH1 define distinct epigenetic and biological subgroups of glioblastoma. Cancer Cell *22*, 425–437.

Sundar, S.J., Hsieh, J.K., Manjila, S., Lathia, J.D., and Sloan, A. (2014). The role of cancer stem cells in glioblastoma. Neurosurg. Focus *37*, E6.

Tajes, M., Ramos-Fernández, E., Weng-Jiang, X., Bosch-Morató, M., Guivernau, B., Eraso-Pichot, A., Salvador, B., Fernàndez-Busquets, X., Roquer, J., and Muñoz, F.J. (2014). The blood-brain barrier: structure, function and therapeutic approaches to cross it. Mol. Membr. Biol. *31*, 152–167.

Tan, A.S., Baty, J.W., Dong, L.-F., Bezawork-Geleta, A., Endaya, B., Goodwin, J., Bajzikova, M., Kovarova, J., Peterka, M., Yan, B., et al. (2015). Mitochondrial genome acquisition restores respiratory function and tumorigenic potential of cancer cells without mitochondrial DNA. Cell Metab. *21*, 81–94.

Tan, B.-X., Yao, W.-X., Ge, J., Peng, X.-C., Du, X.-B., Zhang, R., Yao, B., Xie, K., Li, L.-H., Dong, H., et al. (2011). Prognostic influence of metformin as first-line chemotherapy for advanced nonsmall cell lung cancer in patients with type 2 diabetes. Cancer *117*, 5103–5111.

van Tellingen, O., Yetkin-Arik, B., de Gooijer, M.C., Wesseling, P., Wurdinger, T., and de Vries, H.E. (2015). Overcoming the blood–brain tumor barrier for effective glioblastoma treatment. Drug Resist. Updat. *19*, 1–12.

Temperley, R.J., Wydro, M., Lightowlers, R.N., and Chrzanowska-Lightowlers, Z.M. (2010). Human mitochondrial mRNAs—like members of all families, similar but different. Biochim. Biophys. Acta - Bioenerg. *1797*, 1081–1085.

Tenson, T., and Mankin, A. (2006). Antibiotics and the ribosome. Mol. Microbiol. *59*, 1664–1677.

Tsuboi, M., Morita, H., Nozaki, Y., Akama, K., Ueda, T., Ito, K., Nierhaus, K.H., and Takeuchi, N. (2009). EF-G2mt is an exclusive recycling factor in mammalian mitochondrial protein synthesis. Mol. Cell *35*, 502–510.

Urbanska, K., Sokolowska, J., Szmidt, M., and Sysa, P. (2014). Glioblastoma multiforme - an overview. Wspolczesna Onkol. *18*, 307–312.

Vecchio, D., Daga, A., Carra, E., Marubbi, D., Baio, G., Neumaier, C.E., Vagge, S., Corvò, R., Pia Brisigotti, M., Louis Ravetti, J., et al. (2014). Predictability, efficacy and safety of radiosensitization of glioblastoma-initiating cells by the ATM inhibitor KU-60019. Int. J. Cancer *135*, 479–491.

Vecchio, D., Daga, A., Carra, E., Marubbi, D., Raso, A., Mascelli, S., Nozza, P., Garrè, M.L., Pitto, F., Ravetti, J.L., et al. (2015). Pharmacokinetics, pharmacodynamics and efficacy on pediatric tumors of the glioma radiosensitizer KU60019. Int. J. Cancer *136*, 1445–1457.

Verhaak, R.G.W., Hoadley, K.A., Purdom, E., Wang, V., Qi, Y., Wilkerson, M.D., Miller, C.R., Ding, L., Golub, T., Mesirov, J.P., et al. (2010). Integrated genomic analysis identifies clinically relevant subtypes of glioblastoma characterized by abnormalities in PDGFRA, IDH1, EGFR, and NF1. Cancer Cell *17*, 98–110.

Viale, A., Pettazzoni, P., Lyssiotis, C.A., Ying, H., Sánchez, N., Marchesini, M., Carugo, A., Green, T., Seth, S., Giuliani, V., et al. (2014). Oncogene ablation-resistant pancreatic cancer cells depend on mitochondrial function. Nature *514*, 628–632.

Viale, A., Corti, D., and Draetta, G.F. (2015). Tumors and mitochondrial respiration: a neglected connection. Cancer Res. *75*, 3687–3691.

Vlashi, E., Lagadec, C., Vergnes, L., Matsutani, T., Masui, K., Poulou, M., Popescu, R., Della Donna, L., Evers, P., Dekmezian, C., et al. (2011). Metabolic state of glioma stem cells and nontumorigenic cells. Proc. Natl. Acad. Sci. U. S. A. *108*, 16062–16067.

Vlashi, E., Lagadec, C., Vergnes, L., Reue, K., Frohnen, P., Chan, M., Alhiyari, Y., Dratver, M.B., and Pajonk, F. (2014). Metabolic differences in breast cancer stem cells and differentiated progeny. Breast Cancer Res. Treat. *146*, 525–534.

De Vriese, A.S., Van Coster, R., Smet, J., Seneca, S., Lovering, A., Van Haute, L.L., Vanopdenbosch, L.J., Martin, J.-J., Ceuterick-de Groote, C., Vandecasteele, S., et al. (2006). Linezolid-induced inhibition of mitochondrial protein synthesis. Clin. Infect. Dis. *42*, 1111–1117.

Walker, J.E. (2013). The ATP synthase: the understood, the uncertain and the unknown. Biochem. Soc. Trans. *41*, 1–16.

Warburg, O. (1956). On the origin of cancer cells. Science *123*, 309–314.

Weinberg, S.E., and Chandel, N.S. (2015). Targeting mitochondria metabolism for cancer therapy. Nat. Chem. Biol. *11*, 9–15.

Wheaton, W.W., Weinberg, S.E., Hamanaka, R.B., Soberanes, S., Sullivan, L.B., Anso, E., Glasauer, A., Dufour, E., Mutlu, G.M., Budigner, G.S., et al. (2014). Metformin inhibits mitochondrial complex I of cancer cells to reduce tumorigenesis. Elife *3*, e02242.

William, D., Walther, M., Schneider, B., Linnebacher, M., and Classen, C.F. (2018). Temozolomide-induced increase of tumorigenicity can be diminished by targeting of mitochondria in in vitro models of patient individual glioblastoma. PLoS One *13*, e0191511.

Würth, R., Pattarozzi, A., Gatti, M., Bajetto, A., Corsaro, A., Parodi, A., Sirito, R., Massollo, M., Marini, C., Zona, G., et al. (2013). Metformin selectively affects human glioblastoma tumor-initiating cell viability. Cell Cycle *12*, 145–156.

Yap, T.A., Gerlinger, M., Futreal, P.A., Pusztai, L., and Swanton, C. (2012). Intratumor heterogeneity: seeing the wood for the trees. Sci. Transl. Med. *4*, 127ps10.

Yuan, X., Curtin, J., Xiong, Y., Liu, G., Waschsmann-Hogiu, S., Farkas, D.L., Black, K.L., and Yu, J.S. (2004). Isolation of cancer stem cells from adult glioblastoma multiforme. Oncogene *23*, 9392–9400.

Zhang, L., Ging, N.C., Komoda, T., Hanada, T., Suzuki, T., and Watanabe, K. (2005). Antibiotic susceptibility of mammalian mitochondrial translation. FEBS Lett. *579*, 6423–6427.

Zhang, Y., Guan, M., Zheng, Z., Zhang, Q., Gao, F., and Xue, Y. (2013). Effects of metformin on CD133+ colorectal cancer cells in diabetic patients. PLoS One *8*.

Zu, X.L., and Guppy, M. (2004). Cancer metabolism: facts, fantasy, and fiction. Biochem. Biophys. Res. Commun. *313*, 459–465.

ACKNOWLEDGEMENTS

This Ph.D. thesis represents the work of the last four years, during which I had the opportunity to work on “drug discovery” from both a biological and a chemical perspectives. During this period, I met and collaborated with several great researchers. From them, I tried to learn as much as possible, and I would like to emphasize in this last chapter how important they have been for me.

In primis, my sincere thanks go to my tutor Prof. Ines Mancini for letting me work on this project, for inspiring me with her love for science, for encouraging my research, and of course for her essential advice.

I would like to specially thank Prof. Alessandro Quattrone for giving me the opportunity to work on this project, adopting me as an official member of his lab. Thanks for the chance to work in such dynamic environment and for the stimulating discussions which have allowed me to grow as a researcher.

I would like to thank my advisor Dr. Angelika Modelska, who with her guidance helped me in all the time of this research.

I have to say a big thank to all our external collaborators: Dr. Lucia Ricci-Vitiani for testing D/Q on her panel of GSCs, confirming our results; Dr. Joanna Rorbach for hosting me in her lab at Karolinska Institute in Sweden and for giving me the opportunity to learn [^{35}S] methione labeling and in gel-activity techniques; Dr. Alexey Amunts for solving Q/D-mitoribosome structure; Prof. Roberto Pallini for performing the *in vivo* experiments and Prof. Stefano Moro for helping in defining dalfopristin derivatives.

I would like to thank the members of my thesis committee (Prof. Pietro Luigi Poliani and Prof. Zofia Chrzanowska-Lightowlers) for their comments and suggestion which let me to improve this manuscript.

I would like to express my special thanks to all the LTG group for the support and for all the fun, food and drinks we have had in the last four years. A special thank to Michela Notarangelo for the help in the lab and to Alessia Soldano for proof-reading this manuscript.

I cannot forget to acknowledge the CIBIO people and the members of the facilities.

Last but not the least, I thank my family: my parents, my sister, my best friend Sara and my boyfriend Michele for supporting me to follow my passions and achieve my goals.